מכון ויצמן למדע
WEIZMANN INSTITUTE OF SCIENCE

עבודת גמר (תזה) לתואר
דוקטור לפילוסופיה

מוגשת למועצה המדעית של
מכון ויצמן למדע
רחובות, ישראל

Thesis for the degree
Doctor of Philosophy

Submitted to the Scientific Council of the
Weizmann Institute of Science
Rehovot, Israel

מאת
זיו מאיר

By
Ziv Meir

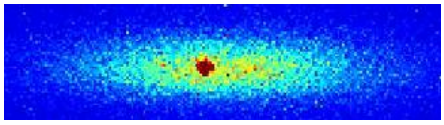

הדינאמיקה של יון בודד, מקורר לאנרגיית היסוד ולכוד בעקבות התנגשויות עם אטומים מאוד קרים.

Dynamics of a single, ground-state cooled and trapped ion colliding with ultracold atoms: A micromotion tale.

מנחה: פרופ' רועי עוזרי

Advisor: Prof. Roee Ozeri

תמוז ה'תשע"ו

July, 2016

This thesis is dedicated to the memory of my father.

תקציר

במסגרת תזה זו אתאר בניית מערכת חדשנית שמטרתה להביא יונים ואטומים לכדי אינטראקציה בטמפרטורות קרות מאוד. הבנת הדינאמיקה של ההתנגשויות בין יונים לאטומים קרים היא הבסיס של תחום מחקר חדש זה ומטרתה להוביל לקו חדש של ניסויים שבהם יונים ואטומים משמשים לחקר כימיה קוונטית ולביצוע סימולציות קוונטיות של מערכות מורכבות. בניסוי שלנו הפגנו בין יוני $^{88}Sr^{+}$ שקוררו למצב היסוד הקוונטי עם אטומי ^{87}Rb קרים מאוד כך ששני המינים בטמפרטורה של כמה עשרות מיליוניות המעלה מעל האפס המוחלט. במהלך הניסוי מדדנו את התפלגות האנרגיה של היון גם אחרי מספר התנגשויות בודדות וגם לאחר התנגשויות רבות עם האטומים [1]. למרות העובדה ששני המינים נמצאים בטמפרטורה של כמה עשרות מיליוניות המעלה, לאחר האינטראקציה הטמפרטורה של היון מגיעה לכמה עשרות אלפיות המעלה. התפלגות האנרגיה של היון לפני ההתנגשויות מתוארת ע"י התפלגות Maxwell-Boltzmann שמאופיינת בזנב מעריכי שלא מאפשר ליון להגיע לטמפרטורות גבוהות. במהלך ההתנגשויות התפלגות האנרגיה של היון משתנה להתפלגות Tsallis שמאופיינת בזנב חזקתי שמאפשר ליון להגיע לטמפרטורות גבוהות מאוד עד כדי שהאנרגיה הממוצעת של היון כמעט מתבדרת. השינוי הדרסטי בהתפלגות האנרגיה נובע ממספר התנגשויות אקראיות רצופות שבהם האנרגיה של היון גדלה כתוצאה מהשדות החשמליים המתנדנדים של מלכודת היונים. הניסוי שלנו ייחודי בכך שאנחנו מקררים את היון למצב היסוד ומקטינים את האנרגיה שלו לפני ההתנגשויות עם האטומים כך שההתנגשות הראשונה היא אכן קרה מאוד. שלא כמו בניסויים אחרים אנחנו לא צריכים לסמוך על האטומים שיקררו את היון, מה גם שהניסוי שלנו מראה שקירור זה לא מתאפשר. בניסוי שלנו האנרגיה של האינטראקציה נקבעת ע"י המשיכה ההדדית של היון והאטום בזמן ההתנגשות. אפקט זה מגביל את היכולת לקרר יונים באמצעות התנגשויות עם אטומים קרים.

המסע שלי לדוקטורט החל בנובמבר 2010 כאשר הצטרפתי לקבוצה של רועי עוזרי כמסטרנט במטרה לבנות מלכודת יונים לניסויים עם אטומים ויונים קרים. לאחר שנה וחצי, ביוני 2012, כדוקטורנט, לכדתי בפעם הראשונה יונים במלכודת שבניתי. במהלך שנת 2013 שיתפתי פעולה עם אוסיפ שוורץ כדי למדוד שינויים ברמות האנרגיה של שרשרת דיפולים מתנדנדים באמצעות היונים במלכודת שלי [2]. לשינויים בקרינה של הדיפול כתוצאה משינוי הסביבה (שבניסוי שלנו מתבצעת ע"י הדיפולים הנוספים בשרשרת) יש יישומים מחקריים רבים כגון צימוד טוב של אטום לאור שחיוני לבניית רשתות מידע קוונטי.

עד לנקודה זו ניסוי היונים היה מופרד פיסית מניסוי האטומים שנבנה ע"י יוני דלאל שהיה גם כן דוקטורנט בקבוצה. בינואר 2014 התחלתי לעבוד על חיבור התאים לכדי מערכת היברידית אחת של יונים ואטומים. לאחר שמונה חודשים באוגוסט 2014 הפגנו לראשונה אטומים ויונים קרים במערכת שלנו. כאן החל מסע חדש לפענוח המסתורין של הפיזיקה של אטומים ויונים בטמפרטורות קרות מאוד.

Abstract

In this thesis I will describe the building of a novel apparatus for overlapping and interacting atoms and ions at ultracold temperatures. Understanding atom-ion collision dynamics is at the heart of the growing field of ultracold atom-ion physics. It can lead to a new line of experiments in which ions and atoms are used to explore quantum chemistry and to perform many-body quantum simulations. In our system, we overlapped a ground-state cooled $^{88}Sr^{+}$ ion with ultracold ^{87}Rb atoms such that both species are at μK temperatures and measured the elastic collisions dynamics by looking on the ion's energy distribution after few and many collisions [1]. Despite the fact that both species start at μK temperatures, we observed the heating of the ion to mK temperatures at steady-state. The ion's energy distribution starts as Maxwell-Boltzmann characterized by an exponential tail which excludes high energies. During collisions, it deviates to a Tsallis distribution with a long power-law tail and almost diverging mean energy. The drastic change in the energy distribution is attributed to multiple consecutive random collisions in which the ion's energy is increased due to the Paul traps oscillating electric fields. Our experiment is unique to its field, since we can ground-state cool the ion and decrease its kinetic energy to the μK regime before collisions starts. This way the first collision is indeed ultracold and we don't need to rely on sympathetic cooling. Moreover, the energy scale of the atom-ion interaction is determined by the pulling of the ion from the center of the trap during a collision, effect which is inherent to Paul traps and sets the fundamental limit for sympathetic cooling in these traps.

My journey began on Nov. 2010 when I joined the group of Roee Ozeri for a master's project aiming to build an ion trap for hybrid atom-ion experiments. One and a half years later on Jun 2012, already as a PhD student, I first trapped ions in my trap. Shortly after, during the entire year of 2013, I collaborated with Osip Schwartz and measured the cooperative line shift in the emission of an ordered crystal of oscillating and interacting dipoles, also known as the cooperative Lamb shift, using the ions in my trap [2]. The change in the optical response of an individual emitter due to its environment, here the other emitters, has vast research application such as enhanced atom-light coupling which is crucial for building quantum information networks.

Up to this point, the ion trap experiment ran as a stand-alone apparatus while another PhD student, Yoni Dallal, built and performed experiments on the atoms part of the hybrid system which was located on a different optical table. On Jan. 2014 I set to connect both experiments to a single hybrid apparatus. Eight months later, on Aug. 2014 we first overlapped atoms and ions in our system and a new journey began to unravel the mysteries of ultracold atom-ion physics.

Acknowledgments

My physics journey started in high school at the eleventh grade. A year before, I started my physics course with very little success or understanding. The way we taught the subject, which was mostly hand waiving and thought experiments conducted inside moving elevators, was completely incoherent to my taste. Then a new young teacher, Isam Abu-Salaman, came to teach our class, directly from his Technion studies. In his first class, he stated that we have no clue about physics and he will start to teach us everything from the beginning. Then he began writing the equations of kinematics on the blackboard. The questions in his tests were taken from his Technion studies; I clearly remember getting similar question from one of his tests in my undergraduate physics studies at Tel-Aviv University. Suddenly, I learned to appreciate the beauty and simplicity in the way physics describes nature.

Fifteen years later, after a long unrelated detour, I came to the Weizmann Institute of Science and to the group of Roee Ozeri. The first person at this point whom I'm very grateful to is Anna Keselman, the legendary MSc student known for mathematically proving proposals wrong, chose not to continue to PhD studies in our group which allowed me to take her intended PhD project of building an ion trap already at the beginning of my MSc. I'm also grateful to Roee who trusted me with this project. Roee who is a great advisor, person and friend has the tendency of being over optimistic. I'm also grateful to the two legendary PhD students at that time - Nitzan Akerman and Shlomi Kotler which both in a completely orthogonal approaches to experimental physics, introduced me to the realm of ion trapping. I want to thank Yoni Dallal for welcoming me and Elad Kronstein to his single person mini-group and to Yinnon Glickman for not electrifying me in the lab. I'm also grateful for meeting Nir Navon which I admire his real enthusiasm for science and his restless way of living. Osip Schwartz taught me how to perform real experiments and how to take data. The year I worked with him was truly insightful. I'm also grateful with the opportunity to work with the new, talented, group members: Tomas, Ruti, Ravid, Tom, Yotam and Meir. I hope they feel the same way with me.

Special thanks is reserved to the technical and administration stuff in the complex system department. Perla, Rachel, Malka and Alona which made it possible for us to concentrate solely in science. The AMO technical stuff: David who designed the mechanical assembly of the trap, 80+ years old Benjamin who built the trap's rf resonators and also measured their properties with the enthusiasm of an undergrad, Guy and Gershon which designed and built numerous parts in our system. Guy also performed an amazing surgery for our gate-valve, he drilled

out a broken bolt from the gate-valve while maintaining differential pressure of 10^{-14} (see Fig. 4.3). Yossi Shopen for his designs, Rusti for solving hard technical problems, Yossi Drier for technical support and Yuri for electronic solutions.

Last but not least, I want to thanks my family, my wife Tal who allowed me to not growing up for six years and my two lovely kids - Aviv and Maayan which are really my best achievement during this period of time.

Contents

List of Figures

Chapter 1
Introduction

Hybrid systems, in our case ultracold trapped ions and atoms, can benefit from the strengths of each of its composing systems. Trapped ions are recognized as the best single qubits in terms of the ability to perform quantum information protocols with high fidelity [3, 4]. They are also excellent local probes with outstanding sensitivity for quantum metrology purposes using "quantum tricks" such as decoherence-free-subspaces and echo-pulses [5, 6]. Trapped atoms, cooled to quantum degeneracy [7, 8], are routinely used to simulate condensed matter physics [9, 10] involving many particles with well controlled and tailored Hamiltonians [11].

Interest in the physics of ultracold atom-ion mixtures [12, 13, 14] has recently increased as several research groups around the world reached experimental maturity [15, 16, 17, 18, 19, 20, 21, 22, 23, 24]. Hybrid atom-ion systems have diverse research applications ranging from quantum chemistry to quantum computing. For example, these systems are suited for emulating solid state physics where the periodic lattice of the trapped ions creates a band-structure in the atomic spectrum [25]. Another interesting proposal is to implement a double-well bosonic Josephson junction [26]. Here, the ion polarizes the atoms leading to long range attraction between the wells with the tunneling rate controlled via the ion polarization [27]. Spin-state-dependent atom-ion interaction is also the basis of an atom-ion quantum gate [28] necessary for quantum information applications.

The polarization interaction between atoms and ions which scales as $1/r^4$ extends to 100's of nm. This long interaction-scale can form macroscopic objects [29] while maintaining quantum features such as Feshbach [30] and shape-resonances [31]. At close range the molecular energy surfaces [32] of the atom-ion system exhibits vast complexity allowing for quantum control on chemical reactions [33]. Even though the field is promising, the experimental research is still in its nursery phase. The complexity of the hybrid system both in technological and physical aspects compels current experimental research with fundamental aspects of the atom-ion interaction.

All the above proposals relies on the atom and ion systems to be in the ultracold regime. Here enters the central complication of hybrid atom-ion experiments which stems from the ion's Paul trap oscillating electric fields [34]. Long time ago, Major and Demhelt realized that a system with heavy atoms and light ions in a Paul trap is thermally unstable [35]. It took more than 50 years until DeVoe

pointed out that the mechanism behind this behavior originates from non Maxwell-Boltzmann statistics which results in power-law energy distributions [36]. In more broader context, Tsallis introduced in 1988 an extension to the Boltzmann-Gibbs statistical mechanics [37] which produces these power-laws and can potentially give the theoretical framework for the collision dynamics.

Numerical simulations of atom-ion systems [36, 38, 39], showed that the non-equilibrium dynamics emanates from the spatial gradient of the oscillating electric fields. Collisions far from the trap center can potentially heat the ion significantly while collisions near the trap center cool the ion down. This results in erratic trajectories in which the ion's amplitude can increase tremendously due to multiple random collisions far from the center of the trap accompanied with sudden decrease of the amplitude due to collision near the trap center. This dynamics is reminiscent to sub-recoil laser cooling of atoms [40] and Lévy walks [41] which can also serve as a theoretical framework for the observed dynamics.

While the above dynamics controls the power-law of the ion's energy distribution, we still didn't address the question of what determines the collisions energy scale? The main experimental effort these days, is to reduce the energy scale of the atom-ion interaction to reach ultracold collisions. The energy scale imposed by the atoms temperature was set to the possible minimum when an ion was overlapped with a Bose-Einstein condensate (BEC) in the groups of Köhl [15] and Denschlag [16]. It was soon realized that in this case, the collision energy is determined by the residual excess-micromotion (EMM) in the system. EMM is a technical issue in ion Paul traps [42] and it can be minimized well below the quantum mechanical energy of the ion's ground-state.

At this point it is interesting to ask what will determine the energy scale of interaction when both atoms temperature and EMM are minimal? Somewhat surprisingly, yet another energy scale was proposed to appear in atom-ion systems [43]. This energy scale is related to the attraction between the ion and the atom during a collision which pulls the ion from the center of the trap into regions of finite oscillating electric fields. Since it is determined by the physical parameters of the system it is regarded as a fundamental limit to the collision energy and it was not observed experimentally prior to the findings reported in this thesis.

Our experiment was set to answer the following urging questions:

- When reducing all energy scales to minimum, will the system be limited by the fundamental limit for atom-ion interaction?

- Can we observe the deviation form Maxwell-Boltzmann to power-law energy distribution?

- Can we perform experiments in the ultracold regime?

This thesis is arranged as follows: In Ch. 2 I will describe the relevant theory necessary for understanding collision dynamics in Paul traps. In Ch. 3 I will describe the building of the ion's experimental system and the necessary tools developed to observe the atom-ion dynamics. In Ch. 4 I will describe experimental aspects of the hybrid system. In Ch. 5 I will present our experimental results. In Ch. 6 I will discuss other approaches for hybrid atom-ion experiments. I will also briefly mention new experimental results which are outside the scope of this thesis. Finally, I will present an outlook on near and future research plans.

Chapter 2

Atom-ion physics

In this chapter I will describe the relevant theory involved in the collision of a single ion with a single atom in a Paul trap. In Sec. 2.1 I will describe the atom-ion polarization potential at large inter-molecular distances which scales as $1/\mathrm{r}^4$. This type of potential leads to both glancing and spiralling (Langevin) collisions. Glancing collisions are purely elastic and involve only very small momentum transfer. In contrast, Langevin collisions involve large momentum transfer and can also lead to inelastic processes such as spin exchange or relaxation [44], charge exchange [33], molecule formation [45] and three-body recombination [46]. In Sec. 2.2 I will describe some of these in-elastic processes. In Sec. 2.3 I will describe how ions are trapped in linear Paul traps using oscillating electric fields and the effect of these oscillating fields on the ion's motion, namely, micromotion. In Sec. 2.4 I will describe another technical, however important, aspect of micromotion - excess micromotion. The minimization of excess micromotion is crucial for reaching ultracold collisions. Micromotion plays an essential rule in the dynamics of atom-ion elastic collisions which I will discuss in Sec. 2.5 both theoretically and by showing molecular dynamics simulation results of collisions between atoms and an ion.

2.1 The -1/r^4 potential

Atoms in their electronic ground-state do not possess a permanent electric dipole moment. Therefore, they interact with the ion through their induced electric dipole moment. The ion generates an electric field on the atom position $\boldsymbol{\varepsilon}(\mathbf{r}) = \frac{e}{4\pi\epsilon_0|\mathbf{r}|^2}\hat{\mathbf{r}}$ which induces an electric dipole moment on the atom $\mathbf{p} = \alpha\boldsymbol{\varepsilon}$. Here, $\mathbf{r}$ is the position vector connecting between the ion and the atom, e is the ion charge, ϵ_0 is the vacuum permittivity and α is the atomic polarizability[1]. The atoms induced electric dipole moment interacts again with the electric field giving rise to a force, $\mathbf{f} = \mathbf{p}\cdot\nabla\boldsymbol{\varepsilon} = \alpha\boldsymbol{\varepsilon}\cdot\nabla\boldsymbol{\varepsilon} = \frac{1}{2}\alpha\nabla(\boldsymbol{\varepsilon}^2)$, and therefore for an attractive potential which scales as $1/r^4$:

$$\mathrm{V}(r) = -\int_{-\infty}^{r}\mathbf{f}\cdot d\mathbf{r} = -\frac{1}{2}\alpha\boldsymbol{\varepsilon}^2 \equiv -\frac{1}{2}\mathrm{C}_4/r^4. \tag{2.1}$$

[1] $\alpha_{Rb} = h\cdot 0.0794(16)$ Hz/(V/cm)^2[47] $\approx 5.2\cdot 10^{-39}$ C·m^2/V.

Here, $C_4 = \frac{\alpha e^2}{(4\pi\epsilon_0)^2}$[2] determines the interaction strength at large atom-ion separation.

The Schrödinger equation for two bodies interacting through a spherically symmetrical potential such as in Eq. 2.1 is given by:

$$\left(-\frac{\hbar^2}{2m_1}\nabla_1^2 - \frac{\hbar^2}{2m_2}\nabla_2^2 + V\left(|\mathbf{r}_1 - \mathbf{r}_2|\right)\right)\Psi(\mathbf{r}_1, \mathbf{r}_2) = E\Psi(\mathbf{r}_1, \mathbf{r}_2). \tag{2.2}$$

By performing a transformation to center-of-mass coordinates [48], one can separate the wave function, $\Psi(\mathbf{r}_1, \mathbf{r}_2) = e^{i\mathbf{k}\mathbf{r}_{cm}}\Psi(r)$, to a trivial free particle center of mass motion and a one-body wave function which depends only on the two-body separation, r, and has an effective reduced mass[3], μ:

$$\left(-\frac{\hbar^2}{2\mu}\nabla^2 + V\left(r\right)\right)\Psi(r) = E\Psi(r). \tag{2.3}$$

A further simplification can be made since the potential is spherically symmetric. We expand the wave function using a basis set of the angular momentum eigenfunctions, $\Psi(r) = \sum_{l=0}^{\infty}\sum_{m=-l}^{m=l} Y_l^m(\theta,\phi)\frac{u_{l,m}(r)}{r}$. Plugging this into Eq. 2.3 yields a one-dimensional Schrödinger equation:

$$\left(-\frac{\hbar^2}{2\mu}\frac{\partial^2}{\partial r^2} + \frac{\hbar^2}{2\mu}\frac{l(l+1)}{r^2} + V\left(r\right)\right)u_{l,m}(r) = Eu_{l,m}(r). \tag{2.4}$$

Here, l is the angular momentum of the atom-ion wave function. The effective potential is composed of the original interaction potential and another term which acts as a centrifugal barrier for high angular momentum wave functions (see Fig. 2.1). The centrifugal barrier position is given by $r_{\text{barrier}} = \sqrt{\frac{2}{l(l+1)}}r^*$ with $r^* = \sqrt{\frac{C_4\mu}{\hbar^2}}$. The centrifugal barrier height is given by $E_{\text{barrier}} = \frac{1}{4}l^2(l+1)^2E^*$ with $E^* = \frac{\hbar^2}{2\mu r^{*2}}$. For our system r^*=265 nm and E^*=80 nK which are typical values in atom-ion experiments. The small energy barrier at low angular momentum suggests that the s-wave regime in atom-ion scattering is still far from experimental reach. The long-ranged interaction scale is much larger than the typical ion extent in the ground-state which is only few nm.

In classical capture model we consider a collision in the center-of-mass frame with energy $E = \frac{1}{2}\mu v^2$ and angular momentum $L = \mu v b$ where b is the impact parameter[4] and v is the relative velocity. Collisions with $b > b_c$, where b_c is

[2] C_4=1.1·10^{-56} J·m^4 for Rb atom.

[3] $\mu = \frac{m_1 m_2}{m_1+m_2}$.

[4] The impact parameter is loosely defined as the closet distance between the particles trajectories when there is no potential.

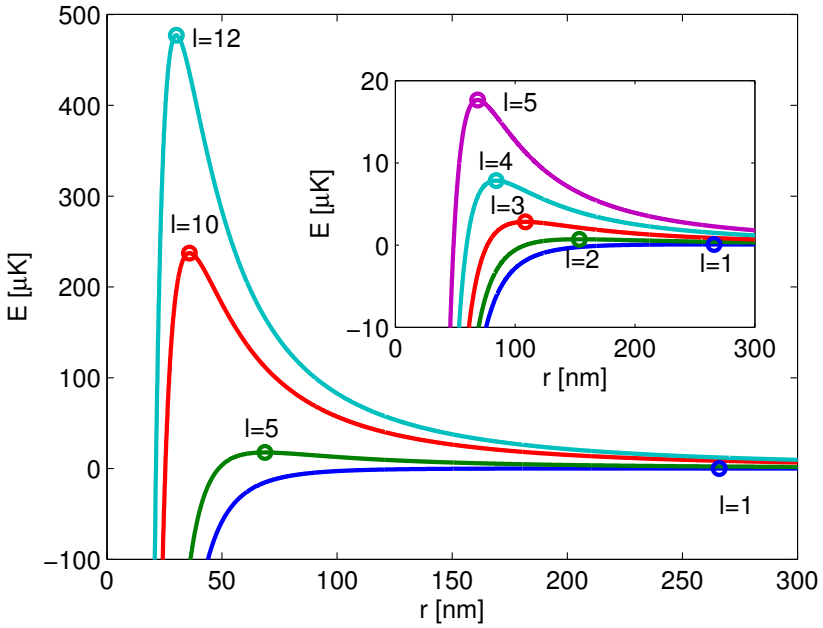

Figure 2.1: **Centrifugal barrier.** The effective potential of Eq. 2.3 is plotted for different angular momentum (l) values. The position and height of the centrifugal barrier is indicated by the open circles. For the typical collision energies in our system (200-500 μK) wave functions with angular momentum less than $\sim 10\hbar$ penetrates the momentum barrier. For quantum micromotion limited ion energy ($\sim$50 μK in our system parameters - Sec. 2.3.1) we would expect this to reduce to $\sim 5\hbar$.

the critical impact parameter, will deflect from the centrifugal barrier. These are glancing (forward-scattering) collisions in which the two bodies deflect each other by a small angle and never get into close proximity. Alternatively, collisions with $b < b_c$ will penetrate the centrifugal barrier. These are Langevin (spiralling) collisions in which the two bodies come into close contact and deflect due to short-range repulsion forces. To calculate the critical impact parameter we recall that the classic centrifugal energy is given by: $\frac{L^2}{2\mu r^2}$. Comparing to Eq. 2.4 we can use the result of the quantum centrifugal barrier, $E_{barrier}$, to calculate the height of the classic centrifugal barrier: $E_c = \frac{L^4}{8\mu^2 C_4}$ from which we can extract the critical impact parameter $b_c = \left(\frac{2C_4}{E}\right)^{\frac{1}{4}}$. The Langevin cross section is given by $\sigma_L = \pi b_c^2 = \pi\sqrt{\frac{2C_4}{E}}$ [49] which results in an energy independent Langevin collision rate[5]:

$$\Gamma_L = n\sigma_L v = 2\pi\sqrt{\frac{C_4}{\mu}}n. \tag{2.5}$$

Here, n is the atoms density. The rate of in-elastic processes (Sec. 2.2) which results solely from Langevin collisions, is energy independent. In Sec. 2.5 we will show that also the heating dynamics of atom-ion collisions in a Paul trap is mainly determined by the Langevin collisions.

2.2 The $(RbSr)^+$ molecule

Numerical *ab inito* calculations are needed to resolve more than the asymptotic behavior of atom-ion energy surfaces. Such calculations were made for various atom-ion systems. The results for our $(RbSr)^+$ system can be found in [32] and are shown in Fig. 2.2. From these potential curves we can understand the different inelastic mechanism in our atom-ion system.

Spin-exchange: $Rb_\uparrow + Sr^+_\downarrow \rightarrow Rb_\downarrow + Sr^+_\uparrow$

The entrance channel of our system which corresponds to neutral Rb and ionized Sr^+ both in the electronic $S_{1/2}$ ground-state[6] splits into two channels at close inter-molecular separation of ∼1 nm. These channels correspond to the electrons arrangement in a singlet configuration for the $(2)^1\Sigma^+$ channel and a triplet configuration for the $(1)^3\Sigma^+$ channel. If the atom and ion are prepared in one of these configurations (e.g., the atoms are prepared in the stretch state $|F = 2, m_F = 2\rangle$ and the ion is prepared in the spin up state $|J = 1/2, m_J = 1/2\rangle$) no spin-exchange

[5] $K_L = \Gamma_L/n = 2.4 \cdot 10^{-9}$ [cm^3/sec] for Rb atoms.

[6] The molecular curve calculations don't include the hyper-fine interaction of the Rb atoms.

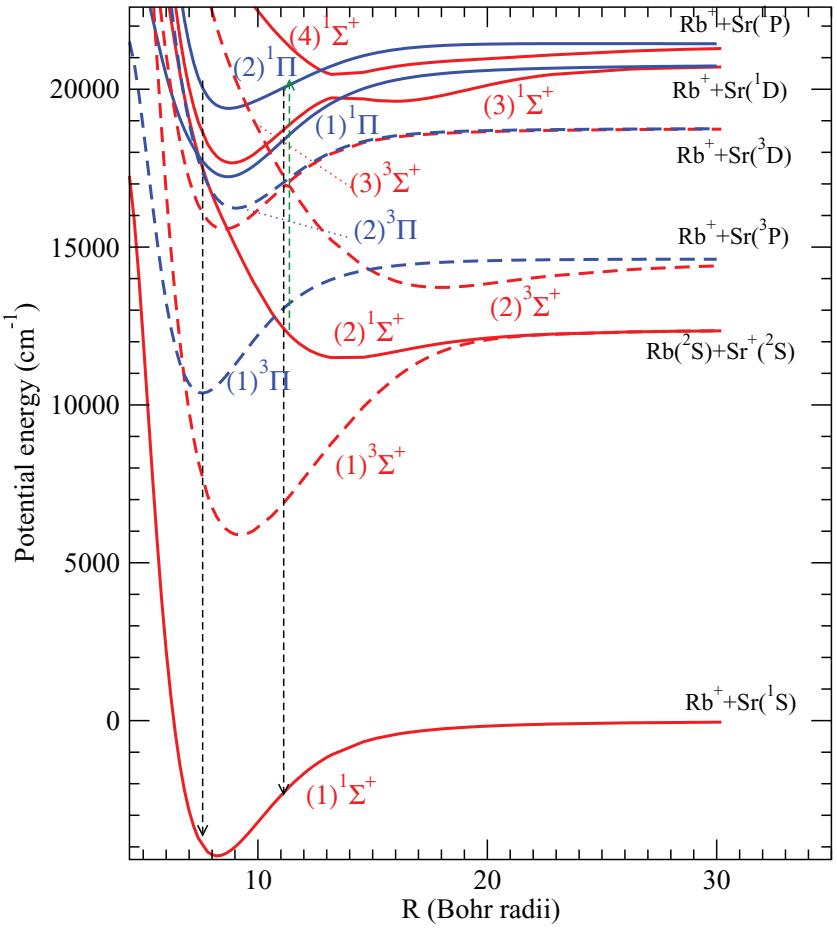

Figure 2.2: **Potential energy curves of the (RbSr)$^+$ system.** System ground state $(1)^1\Sigma^+$ (also referred to as $X^1\Sigma^+$) consist of closed shell ionized Rb^+ and neutral Sr in the $^1S_0$ singlet state. The energy level above the ground state corresponds to ionized Sr^+ and neutral Rb (our system initial state) in the dissociation limit. The energy curve splits into first triplet $(1)^3\Sigma^+$ (also $a^3\Sigma^+$) and second singlet $(2)^1\Sigma^+$ (also $A^1\Sigma^+$) states with zero total angular momentum (Σ) (the singlet/triplet configuration corresponds to the spin state of the two free electrons). The triplet state is attractive due to charge induced dipole long range attraction (r^{-4}) while the singlet is less attractive due to the strong repulsion from the $(1)^1\Sigma^+$ ground state. The energy levels above consists of Rb^+ and Sr in the triplet ^3P state. The $(2)^3\Sigma^+$ curve corresponds to the Sr in the $^3P_0$ state while the $(1)^3\Pi$ curve corresponds to the $^3P_1$ state (J=1). The $(1)^3\Delta$ curve (J=2) was omitted for clarity. Vertical arrows suggest possible photoassociation and spontaneous decay paths to the molecular ground state. Figure was taken from [32].

should occur. However, if the atom and ion are prepared in a superposition of these states, spin-exchange will occur due to the different phase accumulated by the different states during a Langevin collision.

Spin-relaxation: $Rb_{\uparrow}+Sr^{+}_{\uparrow} \rightarrow Rb_{\uparrow}+Sr^{+}_{\downarrow}$

Even if the atom and ion are prepared in a protected spin state, spin relaxation can still occur due to spin-orbit coupling. In atomic systems this inelastic mechanism is often suppressed which is crucial for evaporation to condensates in magnetic traps[7]. However, in the atom-ion system of Yb^{+} and Rb it was found to dominate over the spin-exchange [44].

Charge-exchange: $Rb+Sr^{+} \rightarrow Rb^{+}+Sr$

The lowest energy molecular curve $(1)^1\Sigma^+$ consist of closed shell ionized Rb^+ and neutral Sr in the $^1S_0$ singlet state in the dissociation limit. This energy configuration is favorable over our initial state of Rb atom and Sr^+ ion, each with a single valence electron in the electronic ground-state, by ∼18,000 K. Due to the large energetic gap, bi-partite non-radiative relaxation is unlikely to occur due to momentum conservation. However, spontaneous or stimulated radiative charge-exchange [45] or charge-exchange through a three-body collision [51] are allowed. Since the molecular ground-state is a singlet state, the state of our system in the entrance channel should also have an overlap with the singlet $(2)^1\Sigma^+$ channel. If the system is prepared in a purely triplet state then charge-exchange should be highly suppressed.

Molecule formation: $Rb+Sr^{+} \rightarrow (RbSr^{+})$

Radiative molecule formation is unlikely to occur in our system entrance channel due to small overlap between the second $(2)^1\Sigma^+$ and the deeply bound states in the first $(1)^1\Sigma^+$ singlet channel. However, by exciting our initial state into the $(2)^1\Pi^+$ channel, radiative molecule formation can occur as suggested by the arrows in Fig. 2.2. The photon wavelength for such excitation is around ∼1 μm which suggest that this process can occur spontaneously due to the atoms dipole trap laser. One can also consider stimulated molecule formation [52] by using a second laser with a wavelength ∼400nm, to stimulate the excited molecule into the ground-state.

[7] see Ref. [50] for the case of Cesium atoms where spin relaxation is dominant.

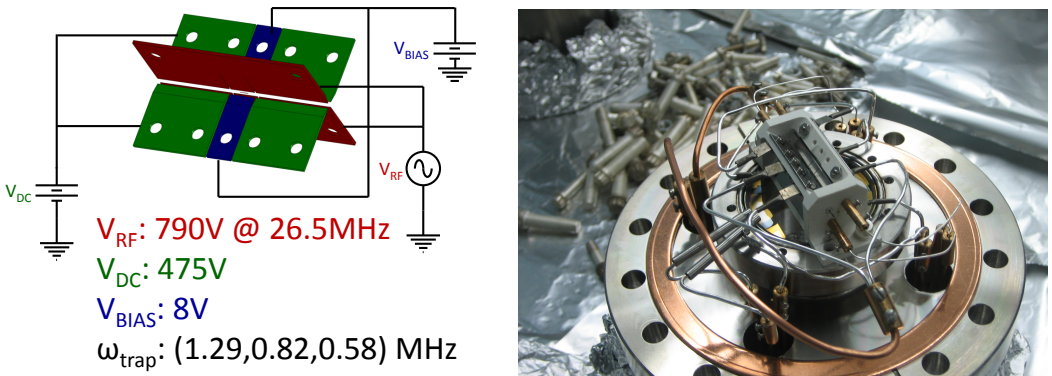

(a) (b)

Figure 2.3: **Linear segmented ion Paul trap.** a) Trap's electrode design. The RF electrodes (red - "RF") are driven with 26.5 MHz oscillating voltage of roughly 790 V. The end-caps (green -"DC") are integrated into the rf-grounded quadrupole electrodes (blue - "GND"/"BIAS" and green) creating a quasi-infinite linear Paul trap which posses negligible rf gradient along the axial axis. The radial compensation electrodes are not shown in this sketch (see Fig. 3.1a). b) Picture of the assembled trap. The trap is mounted with all its electronic connections and ovens on a single CF 6" flange. This makes the connection of the assembled trap to the vacuum chamber effortless.

2.3 Ion Paul trapping

In our experiment we trap ions using a Paul trap [53]. Ion's can be trapped also in Penning traps [54], in multipole traps [55] and also in optical dipole traps [56]. At the present state of atom-ion experimental research, the robustness of Paul traps overcomes speculative advantages other trapping techniques might offer. I will discuss the pros and cons of each trapping technique in Ch. 6.

In ion Paul traps, the oscillating quadrupole radio-frequency (rf) fields create a pseudo-harmonic electric potential which confines the ion. In addition to the harmonic motion, the ion's motion also consists of micromotion, which is an oscillatory motion at the trap rf frequency.

Consider the symmetric linear Paul trap configuration shown in Fig. 2.3. We apply an rf voltage (V_{RF}) at frequency Ω on the RF (red) electrode while the GND (blue) and DC (green) electrodes are kept in rf ground. For an ideal trap[8], in a region close to the trap center, the electric potential is quadratic and has

[8]Here we neglect mechanical and electrical miss-alignments which will be discussed in Sec. 2.4.

components only in the radial direction:

$$\mathrm{V}\left(x,y,t\right)=\frac{\mathrm{V_{RF}}}{2}\left(1+\frac{x^2-y^2}{{R_0^{'}}^2}\right)\cos(\Omega t). \tag{2.6}$$

Here, $R_0^{'}=\epsilon_{R_0^{'}}R_0$ where R_0 is the center-of-trap to electrode distance and $\epsilon_{R_0^{'}}$ is a geometrical factor (for hyperbolic electrodes $\epsilon_{R_0^{'}}=1$). The radial potential of Eq. 2.6 has a cylindrical symmetry which results in degeneracy of the ion's radial modes. To remove this degeneracy[9] we apply a dc voltage ($\mathrm{V_{BIAS}}$) on the GND (blue) electrode:

$$\mathrm{U}_1\left(x,y,t\right)=\frac{\mathrm{V_{BIAS}}}{2}\left(1+\frac{x^2-y^2}{{R_0^{'}}^2}\right), \tag{2.7}$$

In linear Paul traps radial trapping of the ion is due to the rf electric fields while the axial (z-direction) trapping is carried out by a constant (dc) voltage ($\mathrm{V_{DC}}$) applied on the DC (green) electrodes. The static potential near the trap center created by this voltage is given by:

$$\mathrm{U}_0\left(x,y,z,t\right)=\frac{\mathrm{V_{DC}}}{{Z_0^{'}}^2}\left[z^2-\frac{1}{2}\left(x^2+y^2\right)\right]. \tag{2.8}$$

Here, $Z_0^{'}=\epsilon_{Z_0^{'}}Z_0$ where Z_0 is the effective center-of-trap-electrode distance.

The classical equations of motion for ion with mass m and charge e resulting from the above rf and dc electric potentials are in the form of a Mathieu equation [57]:

$$\ddot{u}_i+u_i\left[a_i+2q_i\cos(\Omega t)\right]\frac{\Omega^2}{4}=0, \tag{2.9}$$

where u_i is the displacement of the ion from trap center along axis $i=x,y,z$. The trap parameters, a_i and q_i, are given by:

$$a_{x/y}=-\frac{4e}{m\Omega^2}\left(\frac{\mathrm{V_{DC}}}{{Z_0^{'}}^2}\mp\frac{\mathrm{V_{BIAS}}}{{R_0^{'}}^2}\right),\quad a_z=\frac{8e}{m\Omega^2}\frac{\mathrm{V_{DC}}}{{Z_0^{'}}^2} \tag{2.10}$$

$$q_x=-q_y=\frac{2eV_0}{m{R_0^{'}}^2\Omega^2},\quad q_z=0. \tag{2.11}$$

For typical trap parameters where $a_i,q_i^2<<1$, the solution for Eq. (2.9) can be approximated by [58]:

$$u_i\approx A_i\left(\cos\left(\omega_i t+\phi_i\right)\left[1+\frac{q_i}{2}\cos\left(\Omega t\right)+\frac{q_i^2}{32}\cos\left(2\Omega t\right)\right]+\frac{\omega_i}{\Omega}q_i\sin\left(\omega_i t+\phi_i\right)\sin\left(\Omega t\right)\right). \tag{2.12}$$

[9] To allow for efficient, single beam, laser cooling.

Here we took the second order approximation which is important for analytic simulation of the ion trajectory (Sec. 2.5.5). In most text-books and for understanding the underlying ion dynamics it is sufficient to consider only the first order approximation:

$$u_i \approx A_i \cos\left(\omega_i t + \phi_i\right)\left[1 + \frac{q_i}{2}\cos\left(\Omega t\right)\right]. \tag{2.13}$$

The ion motion is described by a secular (harmonic) part with amplitude A_i, phase ϕ_i and frequency [59]:

$$\omega_i \approx \frac{1}{2}\Omega\sqrt{\frac{a_i + q_i^2\left(\frac{1}{2} + \frac{a_i}{8}\right) + \frac{q_i^4}{128}}{1 - q_i^2\left(\frac{3}{8} + \frac{5a_i}{16}\right)}} \approx \frac{1}{2}\Omega\sqrt{a_i + \frac{1}{2}q_i^2}, \tag{2.14}$$

and a micromotion part with amplitude $A_i q_i/2$ and frequency $\Omega \pm \omega_i$[10].

In symmetric linear Paul traps, the confinement in the axial ($i = z$) axis is purely harmonic. The energy is distributed equally between kinetic and potential energy during one cycle of harmonic oscillation such that the total energy, $E_z = \frac{1}{2}m\left(A_z\omega_i\right)^2$, remains constant. In the same spirit, in the radial axes ($i = x, y$) the energy is distributed equally between secular and micromotion (both kinetic) energy such that the total energy (purely kinetic), $E_i = \frac{1}{2}m\left(A_i\omega_i\right)^2$, is equal to that of an harmonic oscillator with the same amplitude A_i.

The micromotion part of the ion motion has a crucial part in the dynamics of atom-ion collisions. Since the micromotion is essentially a driven motion, in each collision energy can flow from the rf field in or out of the system depending on the exact rf phase during the collision. Moreover, since the amplitude of the micromotion is proportional to the secular amplitude, it serves as an amplifier for collision energy which results in non-thermal energy distributions. I will discuss the dynamics of atom-ion collisions in detail in Sec. 2.5.

2.3.1 Quantum micromotion

The above classical description of micromotion has no associated energy scale since, in theory, the amplitude of secular (and thus also micromotion) motion can completely vanish. However, quantum description of the ion motion [60] reveals that the ion's wavefunction in the ground state resembles that of an harmonic oscillator

[10] The micromotion frequency has higher orders with smaller amplitudes contributions, $n\Omega \pm \omega_i$, as seen in Eq. 2.12.

(Gaussian) plus an oscillatory part which is attributed to the micromotion[11]:

$$\Psi_0(x,t) = \left(\frac{m\omega}{\pi\hbar}\right)^{1/4} e^{-\frac{i\omega t}{2}} \sqrt{\frac{1-\frac{q}{2}}{1-\frac{q}{2}\cos(\Omega t)}} e^{-\frac{m\omega}{2\hbar}\left[\frac{1+q\cos(\Omega t)}{1+q} - i\frac{\Omega}{\omega}\frac{q}{2}\sin(\Omega t)\left(1+\frac{q}{2}\cos(\Omega t)\right)\right]x^2}. \tag{2.15}$$

Here we omitted the index $i = (x, y)$ for clarity. The probability density is given by:

$$|\Psi_0(x,t)|^2 = \left(\frac{m\omega}{\pi\hbar}\right)^{1/2} \frac{1-\frac{q}{2}}{1-\frac{q}{2}\cos(\Omega t)} e^{-\frac{m\omega}{\hbar}\left[\frac{1+q\cos(\Omega t)}{1+q}\right]x^2}. \tag{2.16}$$

While the total probability $\int |\Psi(x,t)|^2 dx \simeq 1 + O(q^2)$ is constant (as it should), the probability density is fluctuating at the rf frequency. This can be seen clearly when calculating the wave-function extent:

$$\Delta x_{g.s} = \sqrt{\langle x^2 \rangle} = \Delta x_{h.o}\left(1 + \frac{q}{2}(1 - \cos(\Omega t))\right). \tag{2.17}$$

Here, $\Delta x_{h.o} = \sqrt{\frac{\hbar}{2m\omega}}$ is the harmonic oscillator ground state wave-function width. We refer to the oscillations of the ion's wave-function as the "breathing" of the wave-function. The amplitude of this motion is given by:

$$x^{\mathrm{q}}_{\mathrm{m.m.}} = (\Delta x_{\max} - \Delta x_{\min})/2 \approx \Delta x_{h.o} q/2. \tag{2.18}$$

We calculate the kinetic energy of the ground state wave-function from the expectation value of the kinetic energy operator, $\hat{T} = \hat{p}/2m$:

$$\langle \Psi_0 | \hat{T} | \Psi_0 \rangle = -\frac{\hbar^2}{2m} \int \Psi_o^* \frac{\partial^2}{\partial x^2} \Psi_0 dx \approx \frac{\hbar\omega}{4}(1 - q(1 - \cos(\Omega t))). \tag{2.19}$$

Averaging over the fast rf oscillation we are left with $\left\langle \hat{T} \right\rangle \approx \frac{\hbar\omega}{4}(1-q)$ which gives a small correction to the kinetic energy of an ordinary quantum harmonic oscillator in its ground state[12]. It is nice to note that if we treat the breathing amplitude derived in Eq. 2.18 as classical amplitude we get the same kinetic energy:

$$E^{\mathrm{q}}_{\mathrm{k}} = \frac{1}{4} m \left(x^{\mathrm{q}}_{\mathrm{m.m.}} \Omega\right)^2 = \frac{\hbar\omega}{4}. \tag{2.20}$$

[11] Note that there is a mistake in the final expression for the ground-state wave-function given in Ref. [60], Eq. 38.

[12] This is yet another example of the equipartition theorem since $\langle H \rangle = \langle T \rangle + \langle V \rangle = 2\langle T \rangle = \hbar\omega/2$ is the ground state energy of a quantum harmonic oscillator.

2.4 Excess micromotion

The micromotion discussed in the previous section is inherent[13] to Paul traps and can be reduced to the quantum limit (Eq. 2.18), but not eliminated, using ground-state cooling[14]. There is another type of micromotion, excess-micromotion (EMM), which is attributed to imperfections in the mechanical and electrical trap assembly. EMM is the persistence of non-vanishing rf fields in the position of the harmonic potential minimum. We distinguish between two mechanisms for micromotion which results in in-phase (Sec. 2.4.1) and quadrature (Sec. 2.4.2) oscillations with respect to the rf phase. The compensation methods for both type of EMM are also different. While we can compensate in-phase EMM by applying dc fields, thus using the trap itself as an rf source for compensating the in-phase part of EMM, we can only compensate quadrature EMM by applying external rf fields with quadrature phase with respect to the rf frequency (Sec. 3.6.3).

In atom-ion collisions, EMM sets one of the energy scales which determines the ion's temperature (This will be discussed in further details in Sec. 2.5). For this reason, to reach ultracold regime of atom-ion collisions, EMM should be minimized.

2.4.1 In-phase excess micromotion

The rf and dc electric potentials given in Eq. 2.6-2.8 assume perfect trap symmetry. Both rf and dc fields vanish at the origin. When the trap assembly is not symmetric due to mechanical misalignments and manufacturing imperfections, the rf fields will vanish (rf null) at a different position from the dc fields (dc null). The electric field due to a shift (x_0, y_0, z_0) between the nulls takes the form:

$$\begin{aligned}\mathbf{E}(x,y,z,t) &\approx -V_{\mathrm{RF}}\left(x\hat{x}-y\hat{y}\right)\cos(\Omega t)/R_0^{'2} \\ &\quad - V_{\mathrm{DC}}\left(2(z-z_0)\hat{z}-(x-x_0)\hat{x}-(y-y_0)\hat{y}\right)/Z_0^{'2} \\ &= -V_{\mathrm{RF}}\left(x\hat{x}-y\hat{y}\right)\cos(\Omega t)/R_0^{'2} \\ &\quad - V_{\mathrm{DC}}\left(2z\hat{z}-x\hat{x}-y\hat{y}\right)/Z_0^{'2} \\ &\quad + V_{\mathrm{DC}}\left(2z_0\hat{z}-x_0\hat{x}-y_0\hat{y}\right)/Z_0^{'2}.\end{aligned} \tag{2.21}$$

In this expression we assumed $\mathrm{V_{BIAS}}$=0 for simplicity. The shift in the dc null translates to a symmetric trap in the presence of additional uniform dc field:

$$\mathbf{E}_{\mathrm{dc}} \equiv V_{\mathrm{DC}}\left(2z_0\hat{z}-x_0\hat{x}-y_0\hat{y}\right)/Z_0^{'2}. \tag{2.22}$$

[13]For this reason, and for the distinction from excess-micromotion, we use the term "inherent micromotion".

[14]Just as in harmonic oscillator where the energy is equally distributed between the potential and kinetic energies, in Paul traps the energy is equally distributed between the micromotion and secular motion. The micromotion quantum limit is the part of the ground-state energy which is stored in micromotion.

Apart from mechanical misalignments, charging of dielectric materials near the trap will also induce dc electric fields in the rf null. The spatial dependence of these fields depends on the geometry of the charged insulators, though, near the trap center it can be assumed to be linear. As before, the effect of these fields is a shift in the harmonic potential minimum and constant dc field at the rf null.

The equation of motion (Eq. 2.9), due to the additional dc field, changes to:

$$\ddot{u}_i + [a_i + 2q_i \cos(\Omega t)] \frac{\Omega^2}{4} u_i = -\frac{e}{m} \mathbf{E}_{\mathrm{dc}} \cdot \hat{u}_i, \tag{2.23}$$

To lowest order in a_i and q_i, the solution is given by [42]:

$$u_i \approx \left[u_i^{\mathrm{dc}} + A_i \cos(\omega_i t + \phi_i)\right] \left[1 + \frac{q_i}{2} \cos(\Omega t)\right], \tag{2.24}$$

where $u_i^{\mathrm{dc}} \approx \frac{e\mathbf{E}_{\mathrm{dc}} \cdot \hat{u}_i}{m\omega_i^2}$ corresponds to a shift in the pseudo-harmonic potential minimum due to the dc field. Note that even when the secular motion is reduced to zero ($\mathbf{A} \to 0$), the ion is oscillating in the rf frequency with an amplitude:

$$x_{\mathrm{m.m.}}^{\mathrm{dc}} \approx \frac{u_i^{\mathrm{dc}} q_i}{2} = \frac{e\mathbf{E}_{\mathrm{dc}} \cdot \hat{u}_i}{m\omega_i^2} \frac{q_i}{2}. \tag{2.25}$$

The kinetic energy of this motion, averaged over an rf cycle, is given by:

$$E_{\mathrm{k}}^{\mathrm{dc}} = \frac{1}{4} m \left(x_{\mathrm{m.m.}}^{\mathrm{dc}} \Omega\right)^2 \equiv \mathrm{k_B T}_{\mathrm{m.m.}}^{\mathrm{dc}} \tag{2.26}$$

By comparing the ion's amplitude due to EMM (Eq. 2.25) to the quantum limit amplitude (Eq. 2.18), we can determine the maximal allowed uncompensated dc field which results with a micromotion amplitude smaller than the inherent quantum limit:

$$\mathbf{E}_{\mathrm{dc}} \cdot \hat{u}_{i\,|max} = \sqrt{\frac{\hbar}{2m\omega_i}} \frac{m\omega_i^2}{e}. \tag{2.27}$$

A summary of the different EMM related values for our trap can be found in Table 2.1.

2.4.2 Quadrature excess micromotion

The analytic expression for the rf fields in the trap (Eq. 2.6) vanishes at the origin due to reflection symmetry ($x \to -x$, $y \to -y$,) which originates from both mechanical trap assembly and electrical rf delivery symmetry. In the case of both electrical and mechanical misalignments, the electric field vanishes at a different position than the origin. Compensation techniques, described in the

		Radial mode	
Parameter	Sec.	x	y
ω [MHz]	2.3	1.29	0.82
$\Delta x_{h.o}$ [nm]	2.3.1	6.7	8.4
$x^{\mathrm{q}}_{\mathrm{m.m.}}$ [nm]	2.3.1	0.4	0.5
$\mathrm{T}^{\mathrm{q}}_{\mathrm{m.m.}}$ [μK]	2.3.1	15	10
$\mathrm{E}_{\mathrm{dc}_{\lvert max}}$ [V/m]	2.4.1	0.4	0.2
$\varphi_{\mathrm{ac}_{\lvert max}}$ [°]	2.4.2	$1.4{\cdot}10^{-3}$	$1.7{\cdot}10^{-3}$
W_0 [mK]	2.5.3	1.8	1.0

Table 2.1: Micromotion related parameters.

pervious section (Sec. 2.4.1), which align the dc null with the rf null solve this problem. However, the compensation technique will fail if the rf null position will vary in time (at the rf frequency). In the following, we'll try to figure out what misalignment will induce an oscillation of the rf null.

Consider the asymmetric electrode configuration shown in Fig. 2.4 with static potential on the electrodes (V_{elec}). The electric potential, $\Phi(\mathbf{r})$, satisfies the Laplace equation, $\nabla^2\Phi(\mathbf{r}) = 0$, with boundary conditions on the electrodes, $\Phi(\mathbf{r}_{\mathrm{elec}}) = V_{\mathrm{elec}}$. The electric field vanishes in some point near the origin[15], $\mathbf{E}(\mathbf{r}_0) = -\nabla\Phi(\mathbf{r})_{|_{\mathbf{r}_0}} = 0$. Now, consider a scale transformation $V \to \alpha V$ on the potential boundary conditions. In this case, the electric potential also scales like the transformation $\Phi \to \alpha\Phi$ and the position of the null is invariant, since $-\nabla\alpha\Phi_{|_{\mathbf{r}_0}} = -\alpha\nabla\Phi_{|_{\mathbf{r}_0}} = 0$. We just showed that if a null exists, its position is invariant under scaling transformation. One such transformation is just the oscillating rf field of the trap, $\alpha = \cos(\Omega t)$. For that, a trap driven with a single tone (single frequency and phase component) can be compensated by eliminating the dc fields at the rf null position. However, if the trap is driven with multiple tones, e.g. quadrature rf (90° phase shifted), with different nulls positions then a non-vanishing oscillating electric field will persist in the minimum of the trap.

Suppose there is a slight phase difference (φ_{ac}) between the rf electrodes due to differences in impedance of the electrodes and their electric connections to the rf source. We define the rf phase relative to one of the electrodes. Then, the voltage

[15] We shall see later, that even though this is the case in the radial direction in the axial direction the electric field can vanish outside the trap.

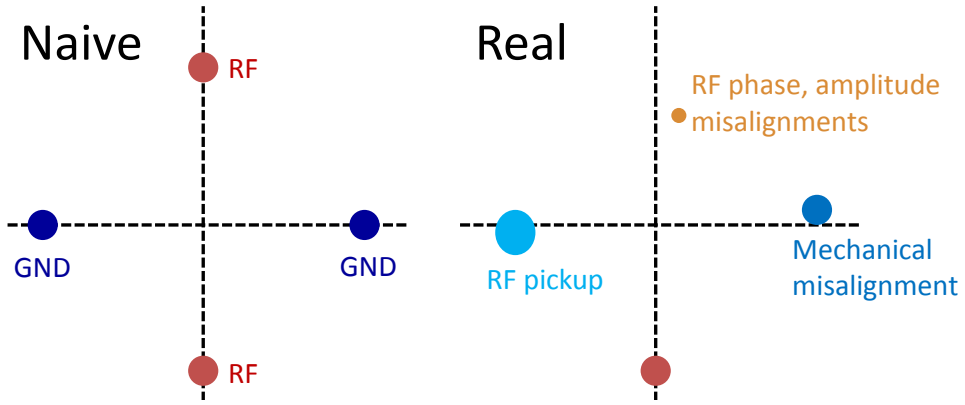

Figure 2.4: **Possible mechanical and electrical misalignments.**

on the other electrode is given by:

$$V_{\mathrm{RF}}\cos(\Omega t+\varphi_{\mathrm{ac}})=V_{\mathrm{RF}}\cos(\Omega t)\cos(\varphi_{\mathrm{ac}})-V_{\mathrm{RF}}\sin(\Omega t)\sin(\varphi_{\mathrm{ac}}). \tag{2.28}$$

The first term in Eq. 2.28 is in-phase with the rf frequency, with a small amplitude difference ($\cos(\varphi_{\mathrm{ac}})\approx 1-\varphi_{\mathrm{ac}}^2/2$) which will result in slight constant shift of the rf null. However, the second term is in quadrature with the rf frequency which will lead to a persisting oscillating field in the position of the rf null:

$$\vec{E}_{\mathrm{ac}}=-V_{\mathrm{RF}}\sin(\Omega t)\sin(\varphi_{\mathrm{ac}})\vec{\beta}^{\mathrm{RF}}. \tag{2.29}$$

Here, $\vec{\beta}^{\mathrm{RF}}$ is the electric field at the rf null due to 1 Volt in one of the RF electrodes, extracted from our trap simulation (Sec. 3.1), $|\beta^{\mathrm{RF}}|\approx 540\left[\frac{1\,V}{m}\right]$. The ion motion due to this field to lowest order in the trap parameters is given by [42]:

$$u_i\approx\left[u_i^{\mathrm{dc}}+A_i\cos(\omega_i t+\phi_i)\right]\left[1+\frac{q_i}{2}\cos(\Omega t)\right]-\frac{eV_{\mathrm{RF}}}{m\Omega^2}\sin(\varphi_{\mathrm{ac}})\sin(\Omega t)\vec{\beta}^{\mathrm{RF}}\cdot\hat{u}_i. \tag{2.30}$$

Note that, as the in-phase EMM, this motion is also independent of the harmonic amplitude ($\mathbf{A}$). It is also independent of the electric dc shift (u_i^{dc}). The resulting EMM amplitude is given by:

$$x_{\mathrm{m.m.}}^{\mathrm{ac}}\approx\frac{eV_{\mathrm{RF}}|\beta^{\mathrm{RF}}|}{m\Omega^2}\sin(\varphi_{\mathrm{ac}}). \tag{2.31}$$

The kinetic energy of this motion, averaged over an rf cycle, is given by:

$$E_{\mathrm{k}}^{\mathrm{ac}}=\frac{1}{4}m\left(x_{\mathrm{m.m.}}^{\mathrm{ac}}\Omega\right)^2\equiv \mathrm{k_B T}_{\mathrm{m.m.}}^{\mathrm{ac}}. \tag{2.32}$$

We can evaluate the maximal allowed phase difference between the electrodes by comparing the micromotion amplitude (Eq. 2.31) to the quantum limit (Eq. 2.18):

$$\sin(\varphi_{\mathrm{ac}_{|max}}) = \sqrt{\frac{\hbar}{2m\omega}}\frac{1}{|\beta^{\mathrm{RF}}|}\frac{1}{R_0'^{\,2}}. \tag{2.33}$$

The resulting maximal phase, $\varphi_{\mathrm{ac}_{|max}} \approx 0.0015°$, is extremely small and corresponds to length difference of 0.05 mm between the RF electrodes leads. We therefore expect to suffer from quadrature micromotion. We can compensate this micromotion better than the quantum limit only by using an external oscillating rf fields.

2.4.3 Axial micromotion

Linear Paul traps are designed for capturing ions in a linear crystal aligned with the trap axial axis. In a symmetric linear Paul trap (Eq. 2.6), the trapping in the axial direction is purely harmonic such that no inherent-micromotion is induced on the ions, even far from the trap center (a typical distance between ions due to Coulomb repulsion is few μm). This will be beneficial in atom-ion experiment with ion chains. Symmetric linear Paul traps posses a line (instead of a point) on which the rf nulls. However, in many real traps (Fig. 2.3) asymmetry in the design slightly breaks the ideal symmetry and rf field gradient penetrates along the axial axis. Our trap is designed to minimize this leakage by using long RF electrodes with notches aligned with the GND-DC electrodes gap (see Fig. 2.3b) to maintain inversion symmetry as much as possible. The deviation from symmetry is quantified by the parameter, q_z (Eq. 2.11), which obtains a non-zero value.

We wish to estimate the micromotion in the case of two-ion crystal aligned with the trap axial axis. The ions equilibrium positions are determined by the balance between the Coulomb repulsion and the harmonic trapping [61]:

$$l_2 = 2\left(\frac{1}{2}\right)^{2/3}\sqrt[3]{\frac{e^2}{4\pi\epsilon_0 m\omega_z^2}}. \tag{2.34}$$

In our trap, $l_2 = 6.2$ μm is the two-ions distance. Even for dc-compensated trap, this displacement from the rf null will lead to in-phase EMM due to the small rf leakage in the axial axis:

$$x_{\mathrm{m.m.}}^{\mathrm{ax}} \approx l_2 q_z. \tag{2.35}$$

Trap simulation (Sec. 3.1) including mechanical asymmetry yield for our trap $x_{\mathrm{m.m.}}^{\mathrm{ax}} \approx 0.25$ nm, which is lower than the quantum limit.

The vanishing axial rf gradient in symmetric Paul traps leads to further complication. Due to trap imperfections, a non-vanishing rf field can persist along the

axial axis of the trap. In the case of regular linear Paul trap, this will lead to a shift in the null position along the axial axis which can be compensated using dc fields as described in Sec. 2.4.1. However, in symmetric traps, where the rf gradient is close to zero, the null position can lie outside the trapping region. In this case, we must compensate axial micromotion by applying an external rf field with opposite phase of the micromotion. This technique which is unique in ion trapping community is described in Sec. 3.6.3.

2.5 Collisions dynamics in a Paul trap

In thermodynamics, two isolated systems in contact with each other will thermalize to the same temperature. This fundamental concept is the basis for sympathetic cooling, in which, the temperature of a small system is controlled by bringing it into contact with a larger system (the bath). Sympathetic cooling of ions (small system) with atoms (the bath) can be used for cooling of dark ions, anions and molecular ions for which the electronic structure needed for laser cooling is lacking. In the case of molecular ions sympathetic cooling can also be used to cool the rovibrational modes. Sympathetic cooling also provides a quicker and more robust way for cooling simultaneously the numerous modes of ion chains used in quantum computation and simulation.

The naive picture of sympathetic cooling in our system presumes that in each atom-ion collision energy is transferred from the hot ion to the colliding atom which is then usually lost from the shallow atom's trap. After several of such collisions this process should lead to thermalization of the ion to the atomic bath temperature. This naive picture complectly fails in our system due to the following reasons:

- Due to the time dependent oscillating fields which creates the Paul trap, our system is open and energy can flow in and out via collisions which interrupt the motion of the ion with respect to the rf phase (Sec. 2.5.1).

- The amplitude of the oscillating fields, which nulls at the trap's center and grows linearly with the distance from the center of the trap, give rise to power-law (Tsallis [37]) instead of exponential (Maxwell-Boltzmann) distribution of the ion's energy (Sec. 2.5.2).

- In addition to the atoms temperature energy scale, two more energy scales are involved, namely EMM [38] (Sec. 2.5.4) and the re-action of the ion to the polarization force during a collision [43] (Sec. 2.5.3). The last sets a fundamental limit for the ion's steady-state temperature.

2.5.1 Single collision: micromotion heating

The interplay between micromotion heating and sympathetic cooling has been known for a long time. In 1968 Major and Demhelt [35] have shown that in Paul traps, sympathetic cooling is most efficient for light atoms and heavy ions ($m_i \gg m_a$), in-contrast to ordinary sympathetic cooling which is most efficient for equal particle masses ($m_i = m_a$)[16]. In-fact, in Paul traps, equal masses (in the Demhelt treatment) was shown to give zero cooling or heating. For light ions colliding with heavy atoms ($m_i \ll m_a$) it was predicted that an exponential heating of the ion arises.

The principle of ion heating and cooling in the presence of an external oscillating field is depicted in Fig. 2.5. Here we consider an over-simplified[17] 1D model of an ion in a constant oscillating external field colliding with atoms at rest. The ion's velocity is described by a center-of-mass part and an oscillating part: $v_{ion}(t) = v_{cm} + v_{EMM}\cos(\Omega t)$. After a hard-sphere elastic collision the ion's velocity is calculated from energy and momentum considerations: $v'(\tau) = -v(\tau)\cdot\chi$ where $\chi = (m_a - m_i)/(m_a + m_i)$ and τ is the time of collision. The new center-of-mass velocity after the collision is given by:

$$v'_{cm} = -v_{cm}\cdot\chi - v_{EMM}\cos(\Omega\tau)\cdot(\chi+1). \tag{2.36}$$

The external field can couple energy in and out of the system depending on the phase of the rf at the instant of the collision and the momentum transfer during the collision. For collision with light atom (green curve in Fig. 2.5, $\chi \approx -1$) the effect of collision is similar to a friction force ($v'_{cm} = (1-\epsilon)v_{cm}$, $\epsilon \ll 1$) which reduce the momentum of the ion and leads to cooling. On the other hand, collision with heavy atom (red to magenta curve, $\chi \approx 1$), which is similar to hitting a wall, maximize the momentum change ($v'_{cm} \approx -v_{cm} - v_{EMM}\cos(\Omega\tau)$) and can lead to unbound heating depending on the rf phase during the collision. In the case of equal mass collision (blue to red curve, $\chi = 0$) the ion's comes to a stop and the center-of-mass velocity ($v'_{cm} = -v_{EMM}\cos(\Omega\tau)$) is determined solely from the rf phase which is equivalent to neither heating nor cooling.

In the above example we showed how an external force (e.g., EMM) which creates a periodic driven motion with zero average velocity, through collision couples to the center-of-mass velocity. This is also true for inherent micromotion which could also lead to heating. The phase-space diagram of one of the radial modes of an ion in a Paul trap is shown in Fig. 2.6. The ion's trajectory lies on an inclined ellipse which oscillates in the rf frequency. After a hard-sphere collision (in 1D) the ion's velocity changes according to $v' = -v\cdot\chi$ while the ion's position remains

[16] Due to the efficient equal-mass momentum transfer during an elastic collision.

[17] Over-simplified since the external oscillating field is spatially constant.

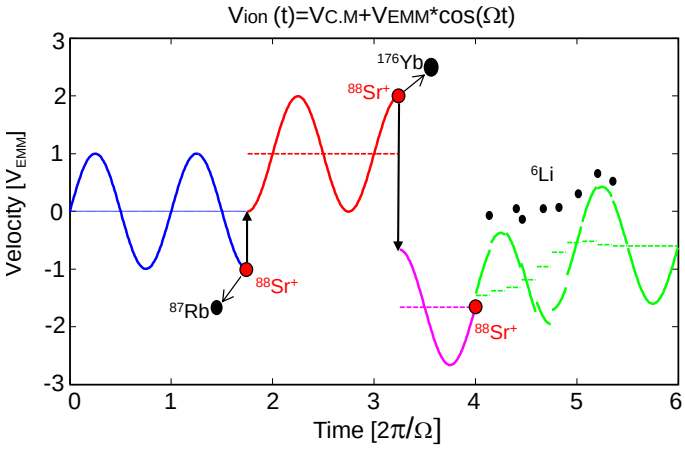

Figure 2.5: **Atom-ion collisions in the presence of external drive.**

unchanged. The new trajectory lies on a new ellipse with the same inclination prior to the collision (see Fig. 2.7). Heating or cooling due a collision in a Paul trap depends on the rf phase, position in the trap and the momentum transfer at the instant of the collision.

2.5.2 Multiple collisions: power-law energy distribution

Numerical molecular dynamics simulations have shown that atom-ion collision dynamics results in a non-thermal energy distribution characterized by a long power-law tail, the magnitude of which depends on the atom-ion mass ratio and trap parameters (see [36, 38, 39, 63] and Sec. 2.5.4). The inherent micromotion, which is proportional to the rf electric field, linearly increases with the ion's distance from the trap center and adds to the energy available in each collision. In the process of consecutive collisions this potentially heats the ion to energies beyond the Maxwell-Boltzmann bounds. This phenomenon is closely related, among other examples, to anomalous diffusion in optical lattices [64, 65] and is well described by non-Maxwellian statistics which was introduced by Tsallis [37].

The ion's energy distribution is described by a Tsallis function:

$$\mathrm{P}\left(\mathrm{E}\right) = \frac{(n-3)(n-2)(n-1)}{2(n\mathrm{T})^3}\frac{\mathrm{E}^2}{\left(1+\frac{\mathrm{E}}{n\mathrm{T}}\right)^n}. \tag{2.37}$$

Here, n and T charectarize the distribution. The first term is used for normalization and the E^2 term in the numerator accounts for the density of states of a 3D

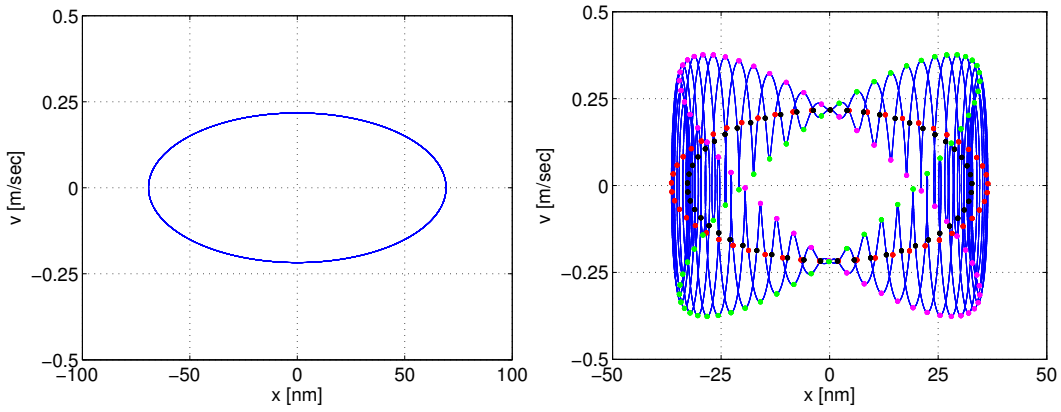

Figure 2.6: **Phase space trajectory.** a) Phase-space trajectory of a Sr^+ ion in Harmonic trap. b) Phase-space trajectory in a Paul trap. Due to micromotion, the ion's trajectory is much more complicated. For a given rf phase the ion's trajectory lies on an ellipse as shown by the coloured dots $(0, \pi/2, \pi, 3\pi/4$ for red,magenta,black and green).

harmonic oscillator. For $n \gg 1$ the distribution converges to the regular Maxwell-Boltzmann distribution, $\mathrm{P}(\mathrm{E}) = \frac{\mathrm{E}^2}{2\mathrm{T}^3} e^{-\mathrm{E}/\mathrm{T}}$, and T is the regular temperature. For smaller n values, the parameter T has an elusive physical meaning. Instead, we can define the distribution by using its mean, $\langle \mathrm{E} \rangle = \int_0^\infty \mathrm{EP}(\mathrm{E})\, d\mathrm{E} = \frac{3n\mathrm{T}}{n-4}$, which diverges for $n \leq 4$ or its mode (most probable energy), $\mathrm{E}_{\mathrm{mode}} = \frac{2n\mathrm{T}}{n-2}$, which is well defined up to $n \leq 3$ where the distribution itself is not normalizable. In our experiment, due to the equal mass ratio of ^{87}Rb and $^{88}Sr^+$, $n \approx 4$ such that the mean energy diverges but the distribution is still well defined. For that, we use the distribution mode to define a Tsallis temperature which converges to the regular temperature for $n \gg 1$:

$$\mathrm{T}_{\mathrm{mode}} = \frac{n\mathrm{T}}{n-2}. \tag{2.38}$$

In the literature Tsallis mathematics is defined using q-functions such as q-Gaussians and q-logarithms [66]. In Tsallis notation the distribution of Eq. 5.1 can be written using the q-exponential function, $\mathrm{P}(\mathrm{E}) = (4-3\mathrm{q})(3-2\mathrm{q})(2-\mathrm{q})\frac{\mathrm{E}^2}{2\mathrm{T}^3} e_{\mathrm{q}}^{-\mathrm{E}/\mathrm{T}}$ which makes the connection to the Maxwell-Boltzmann distribution bluntly apparent. The q-exponential function converges to the regular exponent for q→1. The relation between the q-parameter and our definition of the power-law parameter, n, is given by: $n = \frac{1}{\mathrm{q}-1}$.

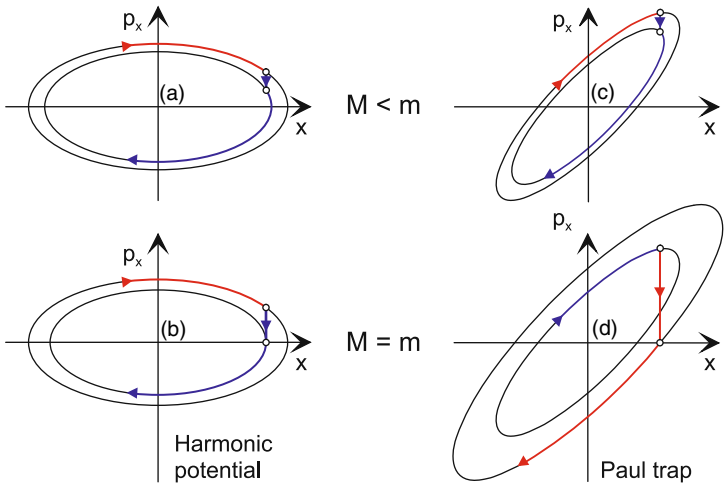

Figure 2.7: **Energy change due to collision with a cold atom.** a,b) Collision in an harmonic trap (or Paul trap at the instant of rf phase equals to $0,\pi$). c,d) Collision in a Paul trap at the instant of rf phase equals to $\pi/2,3\pi/4$. In a,c) the atom mass is much smaller than the ion mass such that the ion's velocity only slightly disturbed by the atom collision while in b,d) the atom and ion mass are equal (similar to our system) such that after collision the ion comes to a stop. We see that for the harmonic case (and also specific phases of the Paul trap) collisions always leads to cooling of the ion while for the Paul trap case collision could lead to heating the magnitude of which depends on the mass ratio, rf phase and the position in trap. Figure was taken from [62].

2.5.3 Fundamental limit in sympathetic cooling

In Sec. 2.5.1 we described the atom-ion interaction as a collision between two hard-spheres without any force acting between them. This simplification is enough to capture the collision dynamics which results from atoms temperature [36, 39, 63] or EMM [38]. In experiments with buffer-gas or with atoms in a magneto-optical trap, atoms temperature might be the largest and relevant energy scale. In ultracold experiments, where the atoms are trapped in optical or magnetic traps with temperature of few or below μK, the relevant energy scale is the residual EMM in the trap center. To our best knowledge, this was the limiting factor in all ultracold hybrid experiments previous to our work [67, 16, 68] .

It is interesting to ask what will determine the steady state temperature and ion dynamics when both EMM and atom's temperature are negligible? To resolve this question one should take into account also the polarization potential acting as a force between the two colliding particles.

Numerical simulations which includes the polarization potential between the atom and ion ([43] and also Sec. 2.5.5) reveals a new energy scale in atom-ion collision dynamics. We consider a fully compensated Paul trap with zero EMM in the rf null and an ion with zero temperature treated classically as a single point colliding with zero temperature atoms. Even in this case a new energy scale arises due to the attraction force between the atom and the ion. During the collision, the ion is pulled away form the trap center into regions with non-zero oscillating rf fields. The work carried out by the oscillating electric fields on the ion during the collision places a new characteristic energy scale [43][18] which sets a lower limit for sympathetic cooling in Paul traps:

$$\mathrm{W}_0 = 2\left(\frac{\mu^5\omega^4\mathrm{C}_4}{m_i^3 q^2}\right)^{\frac{1}{3}}. \tag{2.39}$$

Here, μ and m_i are the reduced and ion mass respectively, ω is the trap radial frequency, q is the trap Mathieu parameter and C_4 is the atom-ion interaction strength (Eq. 2.1). By neglecting the anti-trapping effects of the dc fields, namely $q \approx \frac{2\sqrt{(2)}\omega}{\Omega}$, we can simplify Eq. 2.39 further: $\mathrm{W}_0 = \left(\frac{\mu^5\Omega^2\omega^2\mathrm{C}_4}{m_i^3}\right)^{\frac{1}{3}}$. This suggests that for minimizing the energy scale, we need to choose the heaviest ion ($^{176}\mathrm{Yb}^+$), lightest atom (^{6}Li) and use a shallow, "slow" trap. In our trap $\mathrm{W}_0 \approx 1.5$mK which makes it the highest energy scale in our system. Replacing our atom and ion to Li and Yb will reduce the energy scale by two orders of magnitude, $\mathrm{W}_0 \approx 13\mu$K[19], on par with the kinetic micromotion energy of the quantum ground state (Eq. 2.20).

[18] We slightly change the appearance of Eq. 4 in ref. [43].

[19] $\alpha_{Li} \approx 2.6 \cdot 10^{-39}$ C·m^2/V and the radial frequency is decreased by half due to the double mass of the ion.

2.5.4 Hard-sphere collisions simulation

We perform two type of atom-ion collision simulations[20]. The simpler type treats only hard-sphere collisions. In a more involved simulation (Sec. 2.5.5) we also include the effect of the re-action of the polarization potential on the ion's position.

We start the simulation by sampling the ion's initial total energy ($\mathrm{E_{ion}}$) from a Maxwell-Boltzmann distribution of a 3D harmonic oscillator (Eq. 5.1 in the $n \to \infty$ limit). We calculate the three independent ion's amplitudes by assuming thermal equilibrium between the ion modes and using the equipartition theorem: $A_i = \sqrt{\frac{2\mathrm{E_{ion}}}{3m\omega_i^2}}$. The ion's initial phases, ϕ_i, are sampled from a uniform random distribution. The motion of the ion between collisions is calculated analytically using the solution of the Mathieu equations in the presence of EMM (Eq. 2.24)[21] from which we derive the ion's velocity just before the collision:

$$v_i\left(t_c\right) \approx -A_i\omega_i \sin\left(\omega_i t_c + \phi_i\right) - \left(A_i \cos\left(\omega_i t_c + \phi_i\right) + u_i^{dc}\right) \Omega \frac{q_i}{2} \sin\left(\Omega t_c\right). \quad (2.40)$$

Here, the first term is the secular velocity while the second term includes both the inherent[22] and excess micromotion velocities. The time between consecutive collisions, t_c, is randomly sampled from exponential distribution to render a constant rate of Langevin collisions. We also included the effect of the atomic cloud finite-size by biasing the collision probability with the local atomic density in the position of the collision. The atomic temperature is also sampled from a Maxwell-Boltzmann distribution. The atoms velocity-vector is randomly and uniformly sampled.

Since the collisions are modeled as instantaneous, the position of the ion remains constant during the collision, $\mathbf{u}' = \mathbf{u}$, which implies:

$$A_i \cos(\omega t_c + \phi) = A_i' \cos(\omega t_c + \phi'). \quad (2.41)$$

Where, A_i''s and ϕ_i''s are the new ion's amplitudes and phases. The velocity of the ion just after the collision is determined by energy and momentum conservation:

$$\mathbf{v}' = (1-\beta)\left(\mathbf{v} - \mathbf{v}_a\right) + \beta\Re\left(\mathbf{v} - \mathbf{v}_a\right) + \mathbf{v}_a. \quad (2.42)$$

Here, $\mathbf{v}'$ and $\mathbf{v}$ are the ion's velocity after and before the collision, $\mathbf{v}_a$ is the atom's velocity before the collision, $\beta = \frac{m_a}{m_a+m_i}$ and $\Re$ is a rotation matrix which defines the scattering angles and it is randomly and uniformly sampled with each collision, a consequence of the $1/r^4$ potential for Langevin collisions [38].

[20] All simulation results were obtained using a code written by Dr. Nitzan Akerman.

[21] For simplicity we show here the derivation with only the in-phase part of EMM.

[22] We neglect the term $+\omega\frac{q_i}{2}\sin\left(\omega_i t_c + \phi_i\right)\cos\left(\Omega t_c\right)$ which is of higher order in q. The correct sign for this term is given by taking into account higher order terms in the expression for the ion's position (Eq. 2.12).

From the new ion's velocity we determine its new secular velocity:

$$\begin{aligned} v_{i_{|sec}}^{'}(t_c) &= v_i^{'}(t_c) + \left(A_i^{'}\cos\left(\omega_i t_c + \phi_i^{'}\right) + u_i^{dc}\right)\Omega\frac{q_i}{2}\sin\left(\Omega t_c\right) \\ &= v_i^{'}(t_c) + \left(A_i\cos\left(\omega_i t_c + \phi_i\right) + u_i^{dc}\right)\Omega\frac{q_i}{2}\sin\left(\Omega t_c\right), \end{aligned} \tag{2.43}$$

Here, $v_{i_{|sec}}^{'}$ is the secular parts in Eq. 2.40[23] and we used consequence of instantaneous collision (Eq. 2.41) which is also used to derive the secular position:

$$u_{i_{|sec}}^{'}(t_c) = u_i^{dc} + A_i^{'}\cos\left(\omega_i t_c + \phi_i^{'}\right) = u_i^{dc} + A_i\cos\left(\omega_i t_c + \phi_i\right). \tag{2.44}$$

By inverting the new secular velocities and positions we can extract the ion's new amplitudes and phases:

$$u_{i_{|sec}}^{'}(t_c) - u_i^{dc} = A_i^{'}\cos\left(\omega_i t_c + \phi_i^{'}\right) \tag{2.45}$$

$$v_{i_{|sec}}^{'}(t_c) = -A_i^{'}\omega_i\sin\left(\omega_i t_c + \phi_i^{'}\right). \tag{2.46}$$

Armed with these equations we can analytically calculate the maximal amplitude increase during a collision. For equal masses and no EMM it turns out to be $A^{'}/A \approx \sqrt{3}$. This nice result is left as an exercise for the enthusiastic reader[24].

We record the new ion parameters and continue for the next collision. After reaching the final number of collisions (typically 100-300), we repeat the simulation $\sim$10,000 times and recover the ion's energy distribution. The results of a hard-sphere collision simulation with 3 mK ion's EMM energy are shown in Fig. 2.8. We clearly see the deviation from thermal to Tsallis distribution in the energy spectrum.

Finite size effects

The atomic cloud finite-size introduces a cut-off for the ion's heating mechanism (see Fig. 2.8). When the length scale associated with the EMM energy becomes comparable to the cloud-size, the ion trajectory exceeds the atomic cloud-size after only few or even single collision. When the ion's amplitude becomes larger than the cloud-size, atom-ion collisions are prohibited in the outskirts of the ion's trajectory where the micromotion and hence the heating is maximal. This effect can be used for cooling unstable atom-ion mixtures and it was used to show experimentally [69] an increase in the cooling efficiency for hot atoms and huge ion crystals of the same mass.

[23] in the first line we just re-arranged the terms of this equation.

[24] Hint: Find the rf phase and secular phase for which a collision which brings the ion to a stop maximize the inflation of the ellipse in phase-space.

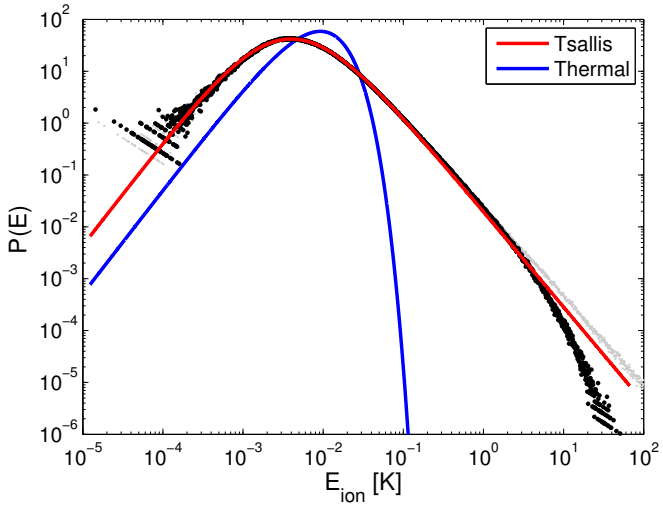

Figure 2.8: **Hard-sphere collision simulation of steady-state energy distribution.** Histogram (6,000,000 data points) of the ion's total energy (dots) in steady-state after hard-sphere collisions with ultracold (6 μK) atoms. In this simulation we set the trap's EMM to 3 mK. In black dots we show a simulation with Gaussian-profile atomic cloud (3.66 μm radial width and 70 μm axial width). In red we show a fit to a Tsallis distribution (Eq. 5.1). The fitted distribution parameters are: $n = 3.8407(16)$ and T=0.9594(13) mK which results in a Tsallis temperature (Eq. 2.38): T_{mode}=2.0018(29) mK. In blue we show a fit to a thermal distribution (Eq. 5.1 with $n \to \infty$, $T_{mode} \approx 10$ mK). In grey dots we show a simulation with infinite cloud size (We record events of up to 10^6 K - not shown). The difference in the distributions of finite and infinite clouds is only in the tail of the power-law which highly affects the mean energy however it has negligible effect on the distribution mode and hence on our definition of temperature (Eq. 2.38).

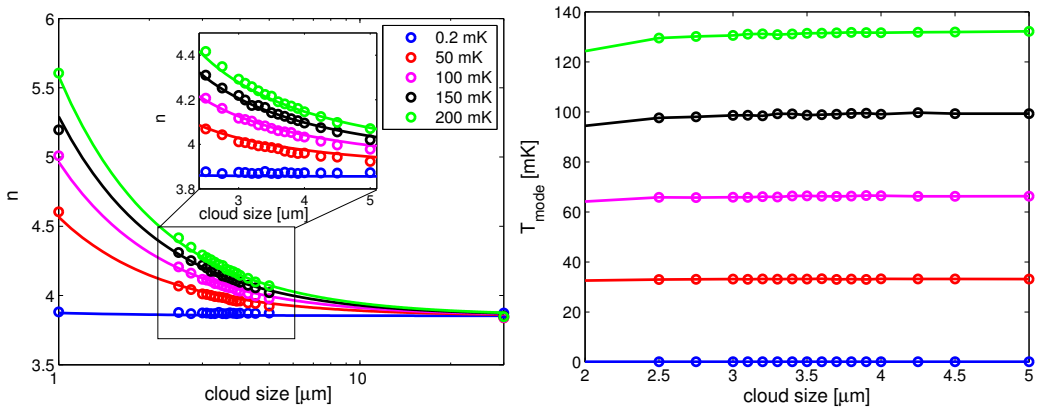

(a) (b)

Figure 2.9: **Effect of atomic cloud size.** a) Power-law fit parameter of the Tsallis distribution (Eq. 5.1) dependance on the atomic radial cloud-size (x-axis) and trap EMM energy (color). b) Tsallis temperature (Eq. 2.38) dependance on the atomic radial cloud-size (x-axis) and trap EMM energy (color). The Tsallis temperature is independent of the atomic cloud-size which makes it good observable for the EMM energy.

We wish to investigate the effect of the atomic cloud-size on the ion's energy distribution. We simulate hard-sphere collisions for different cloud-sizes and EMM energies and fit the steady-state distribution to a Tsallis distribution (Eq. 5.1) with n,T as fit parameters (see Fig. 2.9a). The resulting fit parameters shows an increasing dependance on the atomic cloud-size for growing EMM energies. We fit globally the dependance of the power-law fit parameter, n, to the atomic cloud-size and EMM energy using an empiric function:

$$n = \frac{a}{\left(\frac{\sigma_{\text{atom}}}{x_{\text{EMM}}}\right)^{m}} + n_0. \tag{2.47}$$

Here, σ_{atom} is the atomic radial Gaussian width, $x_{\text{EMM}} = \frac{1}{\omega}\sqrt{\frac{k_B E_{\text{EMM}}}{m}}$ is the secular amplitude associated with the EMM energy, n_0 is the power-law for infinite cloud-size and/or zero EMM energy and a,m are fit parameters which quantify the deviation from n_0. We found out that: $n_0 = 3.8533(38)$, $m = 1.280(13)$ and $a = 1.779(14)$. The bare power-law, $n_0 = 3.85$ agrees well with both experimental data (Ch. 5) and more involved simulation (Sec. 2.5.5). We use this empirical formula to estimate the power-law parameter (cloud size is set to 3.66 μm) for the fitting of the experimental re-cooling data (Ch. 5).

We see that the ion's Tsallis temperature (Eq. 2.38) is insensitive to the atomic

cloud-size (Fig. 2.9b), however the Tsallis distribution parameters, n and T, and other observables such as the ion's mean energy are sensitive. This is because the finite size effects are dominant in the tail of the distribution whereas the distribution mode is less affected by the far-tail of the distribution (highly energetic yet rare events). For that, the Tsallis temperature, which is defined using the distribution mode, is a good observable for the energy scale which seeds the atom-ion dynamics. We extract the temperature dependance on EMM energy from the simulation:

$$\mathrm{T}_{\mathrm{mode}} = 0.6555(25)\mathrm{T}_{\mathrm{EMM}}, \tag{2.48}$$

which we will compare to experimental data in Ch. 5.

Reduced dimensionality

Looking on Eq. 2.47, we see that the atomic cloud-size and the EMM energy scale plays the same role in determining the power-law of the distribution. This power-law is responsible to the ion's energy extent and hence to the spatial extent of the ion's trajectory. If our goal is to study ultracold atom-ion collisions or to study mixtures which are not stable for trapping, we want to increase the power-law of the distribution by decreasing the cloud size. Decreasing the cloud size in all three dimensions simultaneously is not feasible due to the fast decrease in the number of atoms and density available for cooling. However, we can significantly reduce the cloud size in single dimension by using, e.g., optical lattice for atom trapping.

In Fig. 2.10 we show the results of a hard-sphere collision simulation, comparing between a radially symmetric cloud-size of 3.66 μm (blue) and a cloud shrinked to 0.1 μm (red) in one of its radial dimensions. We notice that the spatial distribution of collisions coordinates in the squeezed direction changes from power-law (blue dots in Fig. 2.10a, where the blue line is a gaussian distribution with $\sigma = 3.66$ μm) to almost Gaussian (red dots in Fig. 2.10a, where the red line is a gaussian distribution with $\sigma = 0.1$ μm) which follows the atomic density profile. We observe similar behavior on the other two axes. In Fig. 2.10b we show the total energy distribution of the ion. The power-law parameter of the distribution changes from 3.86 (blue) to 5.33 (red). While the Tsallis temperature is only slightly modified from 2 mK to 1.7 mK the mean energy decreased from ∞ to 13mK.

2.5.5 Simulation including the polarization potential

The hard-sphere simulations of the pervious section capture the dynamics of the energy scales imposed by EMM or atoms temperature (Sec. 2.5.2). However, it doesn't capture the dynamics related to the re-action of the polarization force on the ion's position during collision (Sec. 2.5.3) since the polarization force is not

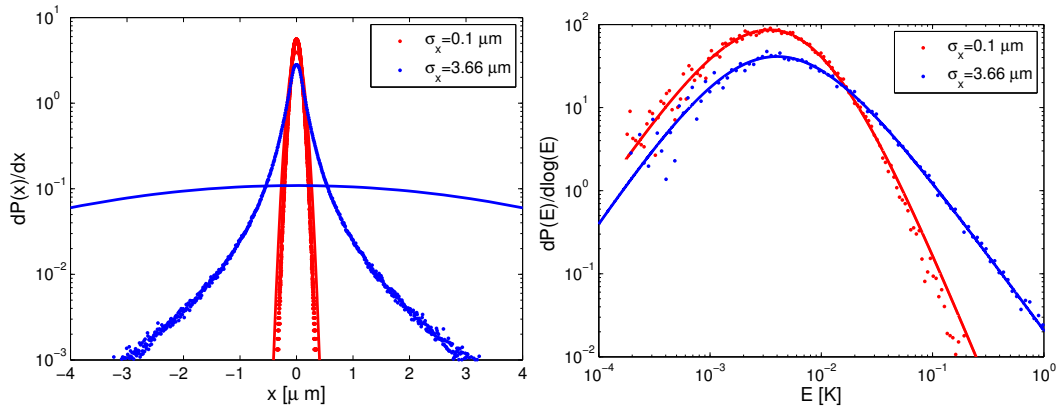

(a) (b)

Figure 2.10: **Reduced dimensionality.** a) Histogram of the projection of the atom-ion collisions position (dots) on the x-axis. Solid lines show the atomic cloud Gaussian distribution (blue σ=3.66 μm, red σ=0.1 μm). The blue data corresponds to radially symmetric cloud (σ=3.66 μm) while in red the cloud is squeezed in only one dimension (σ_x=0.1 μm). b) Total energy distribution. Solid lines show a fit for Tsallis distribution (Eq. 5.1). The power-law of the distribution changes from 3.86 (blue) to 5.33 (red).

included in the simulation. In our system this energy scale dominates over the other two which makes it unique to the atom-ion community.

In a more involved simulation we treat the ion and atoms as billiard-balls with a $1/r^5$ attractive force. Apart from the mutual interaction, the ion also experiences the trap rf and dc fields whereas the atoms are modeled as free particles. In the simulation presented here, we set the EMM amplitude to zero. We simulate time dynamics by letting the ion interact with multiple atoms consecutively, i.e., one atom at a time. At t=0 the ion initial amplitudes are randomly sampled from a Maxwell-Boltzmann distribution with a temperature of 0.5 mK and the ion phases are randomly sampled from a uniform distribution. We define an interaction sphere with a radius of $r_0 = 1.2$ μm centered around the ion trap. A single Rb atom is generated in a random position on the surface of the interaction sphere with random velocity that is sampled from a Maxwell-Boltzmann distribution with temperature of 6 μK. The particles classical trajectories are calculated using the Runge-Kutta fourth-order method until the atom leaves the interaction sphere. In case of contact interaction due to the particles finite size which was set here to 5 nm, a deterministic hard sphere collision is evaluated after which the time integration continues. This procedure approximates the Langevin type spiralling collisions in which the atom and ion are eventually repealed by exchange interaction. An

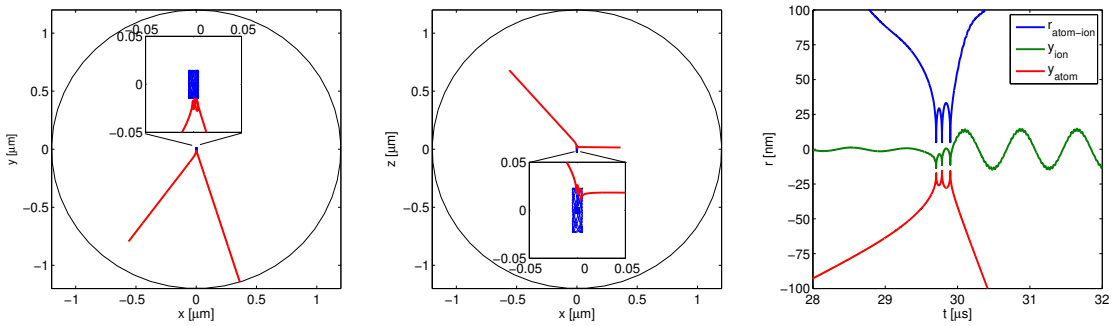

Figure 2.11: **Numerical simulation which includes the effect of the polarization potential.** In the left and middle panels we show the ion (blue) and atom (red) trajectories projected on the x-y and x-z planes respectively. The black circle represents the radius (1.2 μm) from the ion trap center on which the atom is randomly created in the simulation. In the right panel we zoom into the collision. In blue we show the atom-ion distance as function of time. In green (red) we show the ion's (atom's) trajectory projected on the y-axis. As pointed out in Ref. [43], depending on the rf phase during the collision, the total energy of the atom-ion system can decrease during the collision leading to a bound-state of the polarization potential. This bound-state keeps colliding until the system gains enough energy to dissociate as seen in this simulation.

example of such collision in our numerical simulation is shown in Fig. 2.11. This process is repeated with new atoms being randomly generated whereas the ion motion is preserved between the consecutive interaction events (see Fig. 2.12).

In order to reduce computation time, we numerically calculate only events in which the atom-ion minimal separation is below 100 nm. This distance was chosen such that the number of numerical integrated glancing trajectories is minimized without missing any Langevin collision. Contrary to the hard-sphere collision simulation of Sec. 2.5.4, in this simulation we clearly distinguish between the two types of elastic collisions (see Fig. 2.13). In glancing collisions the momentum transfer per collision is small and the total effect of the collisions is cooling while in the Langevin collisions the momentum transfer is much larger and the total effect of the collisions is heating. In-fact, we see (Fig. 2.13b - dashed blue lines) that during a Langevin collision the ion can gain more energy than its initial energy in a single collision[25].

One nice by-product of our simulation is the retrieval of the Langevin collision

[25]In Sec. 2.5.4 we calculated the maximal energy gain during single collision due to inherent micromotion. We retrieve this factor of three in energy in simple hard-sphere collisions simulation. In this simulation, the energy gain exceeds this limit because it is seeded by the re-action of the polarization potential.

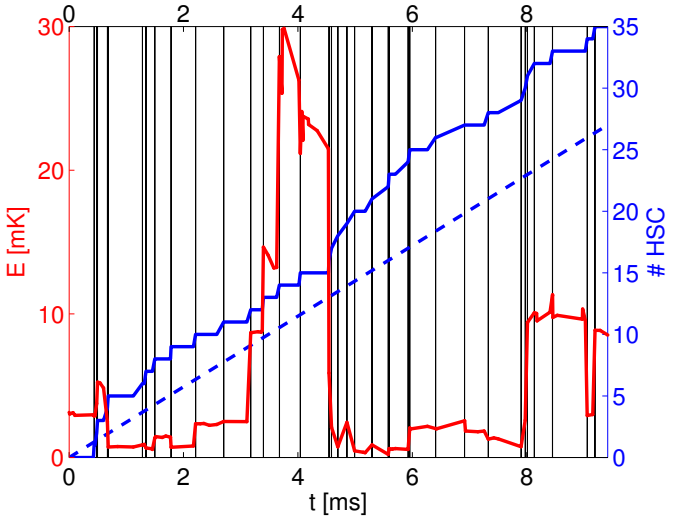

Figure 2.12: **Single simulation trajectory.** We plot the ion's energy (red) as function of time which we calculate from the rate of atoms entering the interaction sphere. We numerically integrate only collisions which cross at distance less than 100 nm. We treat collisions which reach below 5 nm atom-ion separation as hard-sphere (black lines). The solid blue line is the cumulative number of such collisions for this realization whereas the dashed blue line is the theoretical Langevin rate.

rate (Eq. 2.5). To calculate the Langevin rate from the simulation we consider the rate in which thermal atoms enters the interaction sphere of radius r_0,

$$\Gamma = \pi r_0^2 n_{at} \sqrt{\frac{8\mathrm{E}_{at}}{\pi m_{at}}}. \tag{2.49}$$

Here, $\sqrt{\frac{8\mathrm{E}_{at}}{\pi m_{at}}}$ is the average thermal velocity of atoms with mass m_{at} and temperature $\mathrm{E}_{at} = \mathrm{k_B T}_{at}$. We keep track on the number of atoms which we create until a Langevin collision had occurred. This allows us to calculate the distribution of times for Langevin collisions to occur in the simulation. The results and a comparison to the theoretical Langevin rate is shown in Fig. 2.14a.

By running the simulation multiple times we obtain the energy distribution of the ion as a function of time, which we then compare to the experimental results (Ch. 5). Due to the numerical integration, this simulation is much slower than the hard-sphere one such that our statistics is scarce. Moreover, Due to the high energy tail of the energy distribution, as the ion heats, the interaction sphere of 1.2 um introduces finite size effects. Therefore, this simulation is valid only up to ∼6 ms of interaction time (Fig. 2.14b) such that we can't tell whether the ion reached steady-state or not.

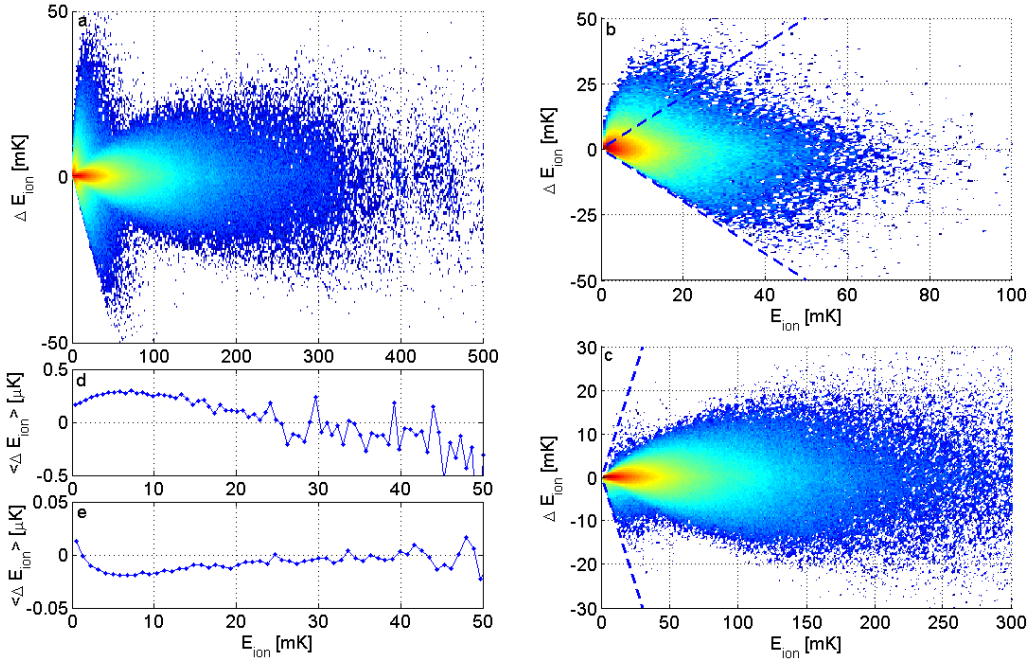

Figure 2.13: **Energy transfer in a single collision event.** a) Histogram of the ion's energy gain (ΔE_{ion}) for given energy before the collision (E_{ion}). The histogram reveals two type of collisions. b) Same histogram as in (a) but conditioned on Langevin collisions (< 5 nm - numerical hard-sphere collision). c) Same as in (a) but conditioned on glancing collisions (> 5 nm). d) Ion's mean energy gain for given collision energy conditioned on Langevin. e) same as in (d) but conditioned on glancing collisions. The net effect of Langevin collision is heating while for glancing is cooling to ∼1.3 mK. Dashed lines in (b,c) indicates $|\Delta E_{ion}|=E_{ion}$.

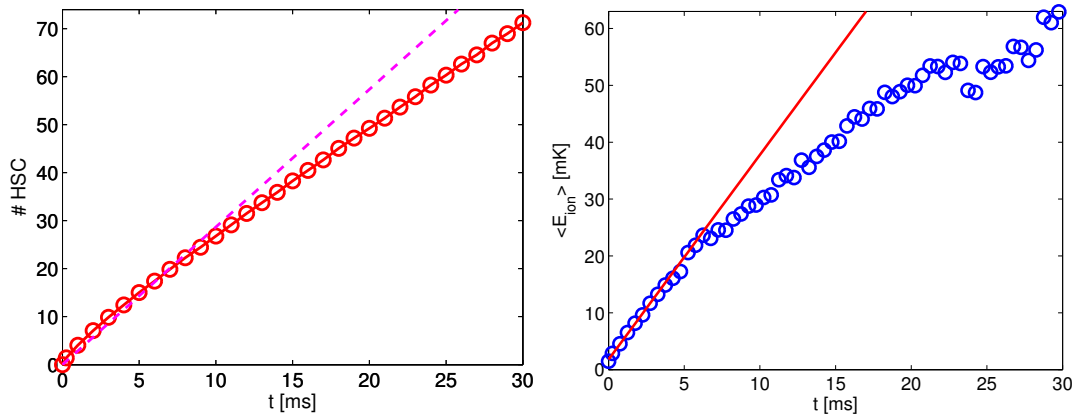

(a) **Langevin rate.** (b) **Mean energy.**

Figure 2.14: a) Mean number of simulated Langevin collisions (red) compared to the theoretical Langevin rate (purple). b) Ion's mean energy as function of time. The deviation from linear rate (red line) is due to numerical integration error. Our simulation results are valid up to 6 ms.

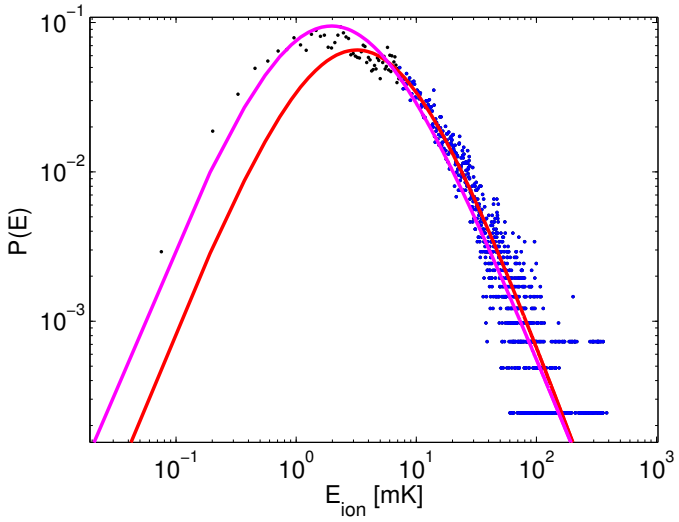

Figure 2.15: **Ion's energy distribution.** Ion's energy histogram (dots) in the time range of 4.5-5 ms as recorded in the numerical simulation (31,000 events). In magenta we fit for a Tsallis distribution using weights linearly proportional to the distribution value. The fit captures the peak however it misses the distribution tail. In red we fit only for the tail of the distribution (blue dots). The fit captures the tail however it misses the distribution peak. For comparison with the experimental results we use the red fit which captures better the power-law tail.

In Fig. 2.15 we show an example of the energy distribution resulting from our simulation. Unlike the more simplified hard-sphere collision simulation (Sec. 2.5.4 and Fig. 2.8), in the more involved simulation which includes the polarization potential it seems that our theory (Tsallis distribution) is incomplete. The method to capture the essence of the power-law is described in the figure caption.

Chapter 3
Ion's experimental system

The ion Paul trap is the heart of the hybrid atom-ion system. Within this Paul trap, ultracold atoms and ground-state cooled ions are overlapped and interact. Our Paul trap is specially designed to satisfy the demanding requirements of hybrid experiments. It is built to overlap a linear chain of ground-state cooled and micromotion compensated ions with a cloud of ultracold atoms. For that, our system should meet the following criteria:

Lamb-Dicke regime - Direct laser cooling of ions to the ground-state requires to operate in a trapping regime known as the Lamb-Dicke regime:

$$\eta = \frac{2\pi}{\lambda}\Delta x_{h.o} \ll 1. \tag{3.1}$$

Here $\lambda = 674$ nm is the wavelength of the cooling laser and $\Delta x_{h.o}$ is the ion's wave-function ground-state extent (Eq. 2.17). This requirement sets a lower limit for the lowest (axial) mode. The radial modes should be roughly twice higher for keeping the ion's linear chain from undergoing a phase transition to zig-zag crystal (see, e.g., [58]). The trap rf frequency is determined by the stability requirements of the Paul trap [58] to be roughly an order of magnitude higher than the radial frequencies. Our typical trap parameters are given in Table 5.1. We can lower our trap frequencies by a factor of few utilizing advanced cooling sequences [70, 71]. The upper limit for the trap frequencies is determined by voltage breakdown between the electrodes. The maximal attainable frequencies in our trap are 2 MHz radially and 1 MHz axially.

Clear path for atoms - This requirement intertwines with the previous one since large traps are limited in their maximal motional frequencies as can be seen from the R^{-2} dependence (Eq. 2.11 and 2.14) of the trap frequency on the ion-electrode distance. We determine the trap electrodes separation from the optical clearance needed for the atoms moving conveyor belt (see Sec. 4.2) which leads to 0.6 mm ion-electrode spacing. We used blade shaped electrodes to increase the NA for both the optical transport and the imaging system (Fig. 3.7). In the final trapping stage, the atoms are trapped in a crossed dipole trap. This leads to an open axial axis design (Fig. 2.3). The axial aperture of radius r=0.6 mm positioned 20 mm from the trap center[1], determines the minimal attainable axial

[1]The aperture hole is used for the construction and alignment of the trap electrodes.

dipole trap beam waist. With this aperture, we are capable to focus the dipole trap axial beam up to 20 μm.

Rf-null line - The requirement for ultracold collisions below the quantum micromotion limit with linear chain of ions boils down to designing a trap with an rf-null line (see theoretical discussion in Sec. 2.4.3). Our trap is designed with long RF electrodes (red in Fig. 2.3a) to minimize the rf gradient along the axial axis.

Trap materials - The trap electrodes are made from Titanium which is non-magnetic. The trap mount is made of machinable Aluminium-Nitride (Shapal^{TM}-M) which has good insulating and thermal proprieties[2].

In the following I will describe in detail the necessary steps in building the ion's apparatus. In Sec. 3.1 I will describe the numerical simulation for determining the trap geometry. Sec. 3.2 will be devoted to the trap assembly and vacuum. In Sec. 3.3 I will describe the dc and rf electric systems of the trap. Sec. 3.4 will be devoted to basic trapping and cooling. In Sec. 3.5 I will describe an experiment performed together with Osip Schwartz on spectroscopic measurement of line-shifts induced by resonant dipole-dipole interactions in linear chains of ions [2]. We perform this experiment with the experimental system which was described up to this point. Sec. 3.6 will be devoted for the coherent control of the ion's electronic state, spin and motion which was used for precision thermometry (Sec. 3.6.2) and excess-micromotion compensation (Sec. 3.6.3).

3.1 Trap's parameters numerical simulation

The analytic discussion of Sec. 2.3 gives a good intuition on the ion motion in the trap but cannot yield the exact trap parameters, a_i, q_i, due to lack of knowledge of the geometrical constants, $\epsilon_{R_0'}$ and $\epsilon_{Z_0'}$. We use CPO[3] simulation program to extract these geometrical constant for our specific trap design. In the simulation we apply 1 Volt on a specific set of electrodes (RF / GND / DC - see Fig. 2.3a) to extract the electric field response (α_i^{elec} $[\frac{1\,\text{Volt}}{\text{m}^2}]$) near the trap center in all trap axes ($i = x, y, z$). The electric field response is found to be linear up to more than 100 μm away from the trap center. For that, we can use the analytic expressions for the ion motion given by the Mathieu equations.

The equations of motion for ion with mass m and charge e are given by:

$$\ddot{u}_i - \frac{e}{m}\left[\sum_{\text{elec}} \bar{V}_{\text{elec}}\alpha_i^{\text{elec}} + \sum_{\text{elec}} \tilde{V}_{\text{elec}}\alpha_i^{\text{elec}}\cos(\Omega t)\right] u_i = 0. \tag{3.2}$$

[2]Resistivity: $1{\cdot}10^{15}$ $\Omega{\cdot}$cm. Thermal conductivity: 92 W/mK. Dielectric strength: 65 KV/mm. Numbers extracted from GoodFellow web-site.

[3]Charged Particle Optics Programs. http://www.electronoptics.com/

Here, $\bar{V}_{\text{elec}}$ are the constant (dc) voltages applied on the electrodes (in our trap $\bar{V}_{\text{DC}} = 475$ V, $\bar{V}_{\text{GND}} = 8$ V and $\bar{V}_{\text{RF}} = 0$) while $\tilde{V}_{\text{elec}}$ are the oscillating (rf) voltages applied on the electrodes (in our trap $\tilde{V}_{\text{RF}}$[4]≈ 790 V and $\tilde{V}_{\text{GND}} = \tilde{V}_{\text{DC}} = 0$). With the use of Eq. (2.9), we can extract the trap parameters:

$$a_i = -\frac{4e}{m\Omega^2}\sum_{\text{elec}} \bar{V}_{\text{elec}}\alpha_i^{\text{elec}}, \tag{3.3}$$

$$q_i = -\frac{2e}{m\Omega^2}\sum_{\text{elec}} \tilde{V}_{\text{elec}}\alpha_i^{\text{elec}}. \tag{3.4}$$

Comparing Eq. (2.10) and (2.11) with Eq. (3.3) and (3.4) we can extract the geometrical factors of our trap. The simulation results of our trap are summarized in table 5.1. We have a very good agreement between the simulated (0.56 MHz) and measured (0.58 MHz) axial trap frequency. Since the rf voltage is unknown, we can only compare the asymmetry between the radial modes created by the voltage on the GND electrode. The simulated asymmetry, $(\omega_x - \omega_y)/(\omega_x + \omega_y) = 0.19$ agrees well with the measured one (0.22).

In addition to trap frequencies, we use the numerical simulation also to extract the electric field created in the trap center when applying voltage on our excess-micromotion compensation electrodes. We use two radial compensation electrodes to create electric dc (and also rf in the future) in the center of the ion trap. Fig. 3.1 shows the orientation of the compensation electrodes in the trap and the resulting radial electric fields. There is a $\sim 30^\circ$ angle between the micromotion detection beams and the electric field vector. The amplitude of the electric field is 6.27 [V/m] for 1 V on the compensation electrodes (we'll compare this value to experimental data in Sec. 3.6.3).

3.2 Ion's vacuum chamber

Collisions with background gas atoms will heat the ion to room temperature. In rare occasions a chemical reaction will occur resulting in a dark ion [5]. Since the majority of background gas atoms are neutral the resulting atom ion interaction is similar to the one discussed in Sec. 2.1 however with much lower densities and rates due to the high vacuum conditions in our system.

The steady state pressure in vacuum systems is given by the balance between the vacuum pumps pumping speed (S $[\frac{\text{L}}{\text{sec}}]$) and the vacuum systems leaks and

[4]The rf voltage value is unknown due to the amplification of the helical resonator. Here, we extract the value from the simulation.

[5]We measured this rate to be roughly one chemical reaction collision in two weeks with pressure of $1 \cdot 10^{-11}$ Torr.

Simulation results	x	y	z
$\alpha_i^{\mathrm{RF}}\left[\frac{1\,V}{\mathrm{mm}^2}\right]$	1.95	-1.95	3.2e-4
$\alpha_i^{\mathrm{GND}}\left[\frac{1\,V}{\mathrm{mm}^2}\right]$	-1.96	1.94	0.0248
$\alpha_i^{\mathrm{DC}}\left[\frac{1\,V}{\mathrm{mm}^2}\right]$	0.0123	0.0124	-0.0245
Voltages	RF	GND	DC
$\tilde{V}_{\mathrm{elec}}$ [Volt]	790	0	0
$\bar{V}_{\mathrm{elec}}$ [Volt]	0	8	475
Trap parameters	x	y	z
q_i	-0.122	0.122	-2e-5
a_i	0.0016	-0.0034	0.0018
ω_i [MHz] - sim.	1.26	0.85	0.56
ω_i [MHz] - meas.	1.29	0.82	0.58
Ω [MHz]	26.5		
R_0 [mm]	0.59		
$R_0^{'}$ [mm]	0.716		
Z_0 [mm]	2.37		
$Z_0^{'}$ [mm]	9.04		

Table 3.1: Calculated trap parameters using CPO simulation.

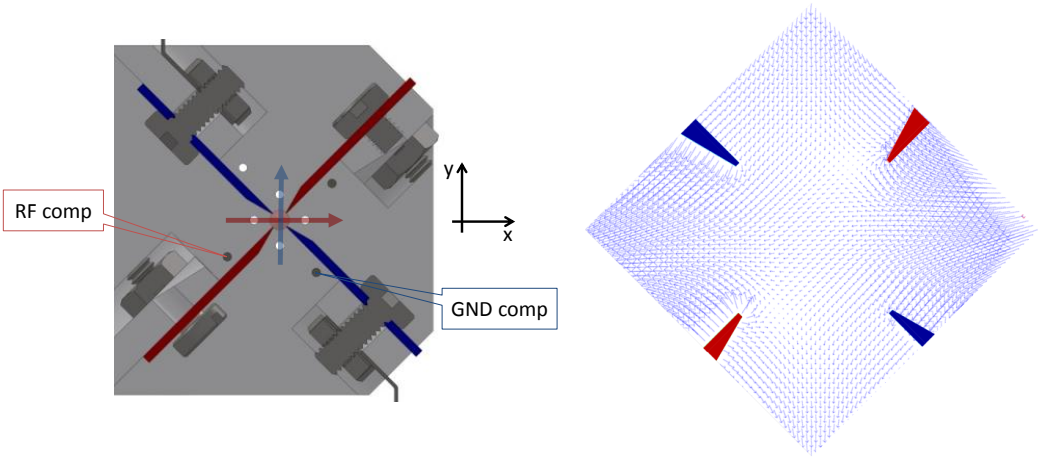

(a) (b)

Figure 3.1: **Radial compensation electrodes.** a) Radial cross section of the ion Paul trap. We use two electrodes to compensate EMM in the radial plane. The RF (GND) compensation electrode is adjacent to the RF (GND) electrode colored in red (blue). b) CPO simulation of the electric fields for -1 V on the RF compensation electrode. These fields moves the ion mostly along the x-axis in the figure. This movement creates motion in the y-direction due the rf-quadrupole fields direction. The GND compensation electrode creates similiar electric fields however 90° rotated.

out-gassing:

$$PS = QA + C\Delta P \tag{3.5}$$

Here, P [Torr] is the vacuum systems pressure, Q $\left[\frac{\text{Torr}\cdot\text{L}}{\text{sec}\cdot\text{cm}^2}\right]$ is the out-gassing from the surfaces (A [cm^2]) of the vacuum system and C $\left[\frac{\text{L}}{\text{sec}}\right]$ is the leak conductance between the vacuum system and the leak source (ΔP is the pressure difference between the leak and the source). To achieve ultra-high vacuum conditions, we need to minimize the leaks and reduce the out-gassing in our system.

3.2.1 Parts and materials

The ion trap mount (Fig. 2.3b) is made of Shapal-M ceramic[6]. We found that even though the material is porous, with long enough bake-out it is ultra-high vacuum compatible. The ion trap electrodes are made of titanium and tungsten metals. The wires connecting the trap electrodes to the vacuum feedthroughs are made of copper[7] and the connectors are made of beryllium-copper[8]. All these metals are vacuum compatible and non-magnetic.

For the main chamber we used a spherical octagon from Kimball-Physics (316 stainless-steel)[9]. All other vacuum components are standard parts from MDC-Vacuum or Kurt-Lesker (304 stainless-steel). These parts are slightly magnetic since even stainless-steel become magnetic when it is machined (the 304ss is more magnetic than the 316ss). For electric conductance to the vacuum chamber we used vacuum feed-through from SST[10] and view-ports from MDC-Vacuum[11] or Kurt-Lesker[12]. These parts are even more magnetic (especially the view-ports) due to the glass-to-metal seal[13].

We designed two special flanges with view-ports for increased NA which were fabricated by MDC-Vacuum. One of the flanges is used also for mounting the trap and it is equipped with four ports for electric feed-thorough's (Fig. 2.3b). This flange was designed such that the ion trap assembly is carried out outside the vacuum chamber and final connection to the vacuum chamber is fast and easy. However, the trap mount assembly attached to the view-port made it highly

[6] machinable Aluminum-Nitride. http://www.shapal.info/characteristics/index.htm.

[7] Solid Sealing Technology (SST) P/N FA21508,FA15065 silver plated copper wires stripped from their Kapton insulation.

[8] SST P/N KT1156x contacts.

[9] P/N MCF600-SphOct-F2C8.

[10] P/N FA11648,FA11666 copper conductor on CF1.33" flange.

[11] P/N 9722005, Fused-Silica glass on CF2.75".

[12] P/N VPZL-275Q mounted on CF2/75". VPZL-275LYAG - AR coated for 1064m.

[13] Both MDC-Vacuum and Kurt-Lesker has non-magnetic option for view-ports not tested in this experiment.

birefringent. A better solution is to separate the window from the mount. These two view-ports were tested in MDC-Vacuum for leaks.[14]

We also designed and manufactured at the Weizmann workshop tilted connectors for the CF.275" view-ports. We use these connectors to mount the view-ports at 2° with respect to the chamber axis. This way, back reflections from the view-port windows do not overlap the beam inside the chamber.

3.2.2 Cleaning and assembly

For cleaning home-made parts we used Deconex (from Borer chemie) solution diluted with ionized water in a hot (50°C) ultrasonic bath. We used the 15 PF-x solution (high PH) to clean most of the parts (stainless steel, titanium, Shapal-M[15] etc.). We used 36-Intensive solution (PH neutral) to clean corrosion-sensitive parts (aluminum, copper and beryllium-copper).

We visually inspected ultra-high vacuum components (vacuum parts, feed-through's, view-ports, connectors, wires etc.) before inserting them without cleaning to the vacuum system[16].

3.2.3 Pumping and bake-out

We use an integrated dry roughing and turbo pump to decrease the chamber's pressure from 1 atm = 760 torr to $\sim 1 \cdot 10^{-6}$ torr. These two pumping stages are not an integral part of our vacuum system. They are connected through an all-metal valve[17] to the system and they are removed in later stage.

There are 3 different types of pumps integrated in our system: ion pump[18], titanium-sublimation-pump (TSP)[19] and non-evaporative-getter (NEG) pumps[20]. We degas the TSP[21] when the ion pump is turned off and the turbo pump is connected to the system. At the same time, we also degassed the Sr ovens by running current in them until the indium seal is breached. We didn't degas the NEG pumps since we can heat them only in the bake-out process. After completing the degassing procedure we turn on the ion pump and wait until it reaches below the turbo pump's pressure ($\sim 1 \cdot 10^{-7}$ torr). We then close the valve which connects the system to the turbo pump and disconnect the turbo pump from our system.

[14] Leak test @ $2 \cdot 10^{-10}$ STD AT. cc/sec Helium.
[15] For the cleaning of Shapal-M we didn't use ultrasonic bath since it disintegrate the part.
[16] We found several non-cleaned view-ports and few vacuum parts with chunks on them.
[17] P/N 54032-GE02 from VAT.
[18] Agilent (Varian) StarCell VacIon plus 40L.
[19] Agilent (Varian) TSP filament cartridge source on CF2.75" P/N 9160050
[20] SAES ST2002/103 pills.
[21] We degassed all there TSP filaments for 7 X 1 minute @ 47A.

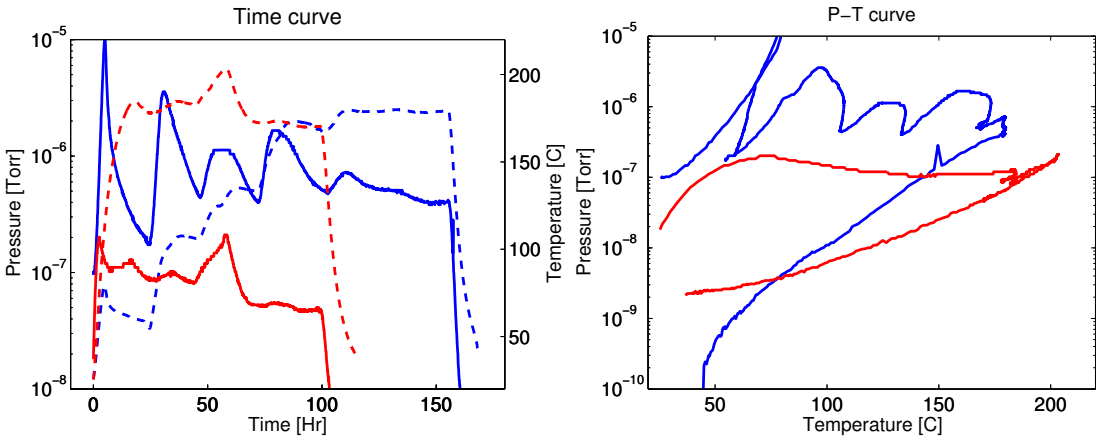

(a) (b)

Figure 3.2: **Bakeout comparison.** a) Pressure (solid lines) and temperature (dashed lines) logs of two different bake-outs. Red line is a log of a bake-out with leaky CF6 window. Blue line is a log of a bake-out of the complete ion system. The duration of the full system bake-out is much longer due to the trap mount ceramic which is porous and the NEGs in the system. b) Pressure-temperature curves for the two systems. The ultimate pressure in the ion system (blue) is much better than the leaky CF6 system (red) due to the leak. There is no indication for the leak until the end of the bake-out procedure.

We monitor the vacuum chamber's pressure at this stage using either the ion pump current or a special UHV gauge[22] installed in our system.

We bake the system at ∼190°C in an home made oven. We wrap the system with many layers of Aluminum foil and monitor the temperature using four thermocouples. We log the pressure readout from the ion pumps controllers and the UHV gauge every five minutes. Bake-outs with different characteristics (leaks, outgassing) are shown in Fig. 4.4.

When the bake-out completes we need to activate the TSP. We fired at 50A only one TSP filament. We fired it three times, each time for one minute. We record the ultimate pressure after bake-out with the UHV gauge[23] cooled down to room temperature using a small fan after one week from bake-out to be below $1.5{\cdot}10^{-11}$ torr[24].

[22] Agilent (Varian) UHV-24p Thoriated Iridium filament on CF2.75"

[23] Gauge setting were: 4mA current, 20 sensitivity and 1 gas correction.

[24] Ultimate pressure reading was $5{\cdot}10^{-12}$ torr. This pressure is below the quoted sensitivity of the gauge.

3.2.4 Tips and tricks

Making a good vacuum system is not an easy nor short task. The building of our vacuum system took almost a year and many iterations and bake-outs. If you have no experience it is good practice to build your system in small steps, learning each time the behavior of the additional component.

In the following I want to share some of the lessons we have learned during the building of our system:

- **Logs** - We log the systems temperature and pressure every 5 minutes during bake-out. This allowed us to compare different vacuum experiments and to understand the impact of any additional component to our system. We observed out-gassing and leak behavior and extrapolate bake time.

- **Patience** - High pressure and long pumping time in the bake-out initial stage is not correlated with the final system's pressure.

- **Leak detection** - Don't skip the use of leak detector to find leaks in your system. We found leaks due to over-sized gaskets, leaks in windows and in feed-throughs. Working with a leak detector requires a lot of experience and patience, if you don't have both ask for help in your first trials.

- **Out-gassing** - Every component in your vacuum system should be cleaned for UHV. Purchased items from vacuum vendors should be examined before assembly[25]. Home-made parts should be cleaned properly before assembly, if you are using a new type of material it should be verified for vacuum compatibility[26].

- **Closing gaskets** - This is basically what you do when building a vacuum system. Use annealed gaskets for view-ports, close the bolts in circular order applying only small torque in each step.

- **Working environment** - The best working environment is a proper clean room. We built our system under a laminar flow. Use gloves and replace them frequently when touching vacuum surfaces. Use mask and hair net when working on inside vacuum components. Clean all your tools for UHV and keep them cleaned.

[25] We found dirt inside nipples and smudge on view-ports from MDC.
[26] We used Chrome-Nickel wire which was not vacuum compatible even after cleaning

3.3 Trap rf and dc

The scheme of the electric connections of the ion's trap electrodes to the vacuum feedthroughs is shown in Fig. 3.3. This scheme can be compared for orientation to a photo of the mounted trap in Fig.2.3b. Both the RF and the GND electrodes are shortened inside the vacuum chamber, any phase-mismatch on these electrodes will result in quadrature micromotion (Sec. 2.4.2). There are no electric filters inside the vacuum chamber.

We use a high-Q ($\sim$500) helical resonator [72] (the rf equivalent circuit is shown in Fig. 3.4) to impedance match and amplify the 50Ω, 4W rf (26.5 MHz) signal of the rf-amplifier[27] to roughly 790 Volt on the RF electrodes. The BIAS voltage applied to the GND electrode is passed through the resonator shield. The dc voltages on the DC and compensation electrodes are filtered using low-pass filters[28] outside the vacuum chamber. We apply a small rf voltage ($\sim$20 Volt) on pair of DC electrodes (Fig. 3.4) to compensate for axial micromotion (Sec. 2.4.3). For that we use a low-Q helical resonator and a bias-tee to couple dc and rf to the electrodes.

Proper electric design improves significantly the trap performance. Improper filtering and grounding of the trap electrodes will increase the ion's heating rates well above the anomalous heating rate threshold. The long-term instability of our dc power supplies induces excess-micromotion drifts. The ion's radial frequency is linearly proportional to the rf voltage on the RF electrode. Therefore, rf voltage stability is crucial if the ion's radial modes are used, e.g, for ground-state cooling. In demanding applications (see, e.g, Oxford group approach in [73] and JQI group approach in [74]), radial modes were stabilized to part-per-million. In our experiment, we found it sufficient to tune the rf frequency to a first-order radial mode frequency insensitive point ($\partial\omega_{\mathrm{rad}}/\partial\Omega_{\mathrm{rf}} = 0$) at which the RF voltage amplitude on the electrodes is at a maximum. Our radial modes stability is few parts-per-thousand which is mainly attributed to amplifier power noise[29]. It is interesting to note that the rf frequency which minimizes the reflections from the trap (impedance matching) is different from this point (see Fig 3.5a).

A simple model which accounts for this discrepancy is given in Fig. 3.5b. The 50Ω voltage source is inductively coupled to the trap (C - trap capacitance, R - wires resistance) using a helical resonator where L_1 and L_2 are the inductance of the resonator antenna and coil respectively. $M=\kappa\sqrt{L_1 L_2}$ is the mutual inductance

[27] Mini-Circuits LZY-1+.

[28] We use 1MΩ resistors and 10nF high-voltage capacitors such that the cut-off frequency is 15Hz.

[29] We have constructed a high-Q resonator with reduced rf frequency of 13 MHz. Using this resonator we should be able to work near the Lamb-Dicke regime without amplifying the function generator signal.

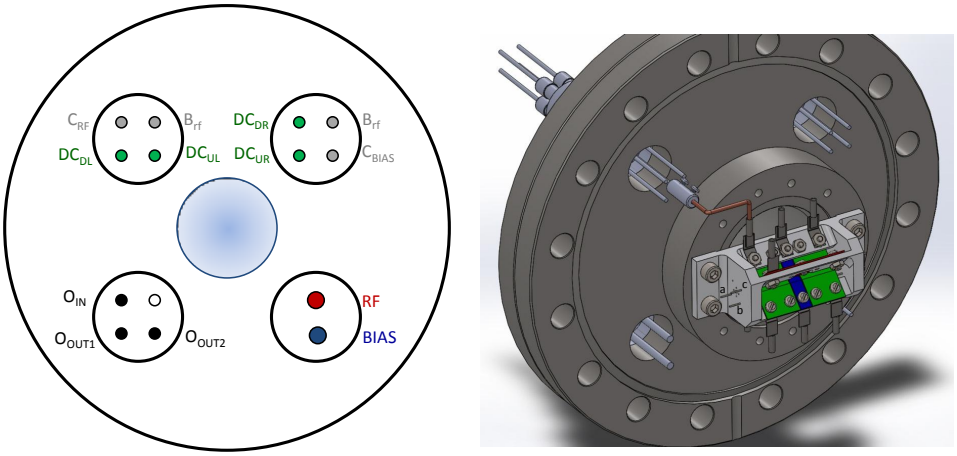

Figure 3.3: **Electric connections.** Diagram of the ion's Paul trap electric connections as seen from outside the vacuum chamber (left) and a SolidWorks drawing of the trap mounted on the CF 6" flange as seen from inside the vacuum chamber (right). A photo of the mounted trap is also available in Fig. 2.3b for comparison. The two RF electrodes (red) are connected inside the vacuum chamber to a single lead (marked as RF in the diagram). The two BIAS/GND electrodes (blue) are also connected inside the vacuum chamber to a single lead (marked as BIAS in the diagram). Each of the four DC electrodes are connected separately to a lead (marked DC in the diagram). The subscripts D(U) stands for down(up) and L(R) for left(right) DC electrode as seen from outside the vacuum chamber. In the SolidWorks drawing the upper-right DC electrode is connected to its lead. There are two compensation electrodes (marked C in the diagram). The subscript RF(BIAS) stands for the compensation electrode which is adjacent to the RF(BIAS) electrode which is marked a(b) in the drawing. These compensation electrodes electrically floats just as all the other electrodes in the Paul trap. The last electrode marked as B_{rf} in the diagram is connected from both sides allowing to pass current through it (marked c in the drawing). The two Sr ovens (see Fig. 2.3b) have a single input lead (marked O_{IN}) and two output leads (marked O_{OUT}).

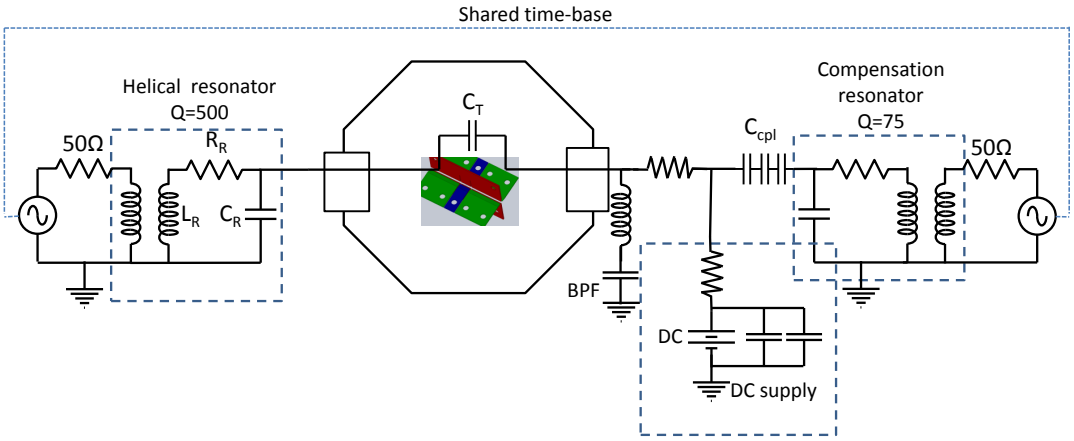

Figure 3.4: **Equivalent electric circuit for the delivery of rf and dc voltages.**

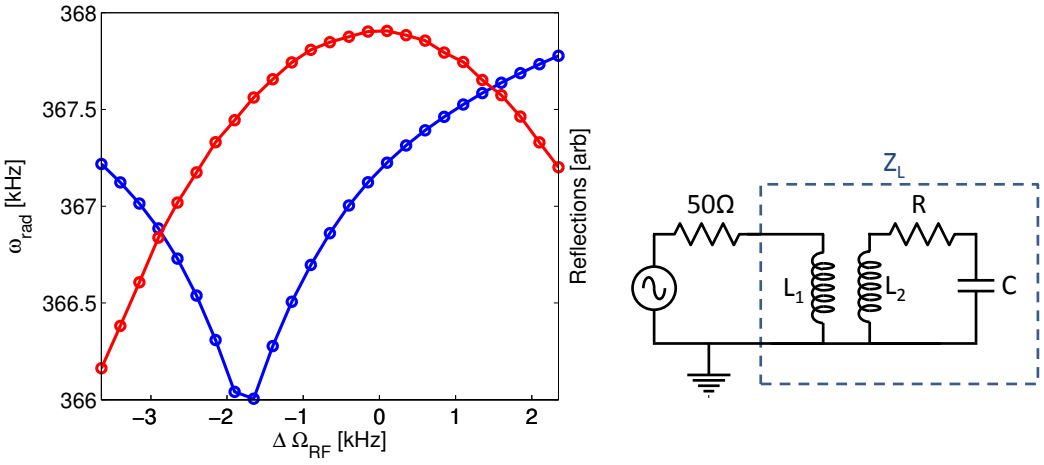

(a) (b)

Figure 3.5: **Tuning the rf-resonator.** a) Trap's radial frequency (red) and power reflections (blue) as function of the rf frequency of the trap. There is an almost 2 kHz shift between the impedance matching condition (minimal reflections) and the maximal trap frequency. b) Simplified circuit of the rf resonator and the trap. L_1 and L_2 are the inductance of the rf-resonator antenna and inner-coil. C is the trap capacitance and R is the wire resistance.

of the coils. The impedance matching condition, which is calculated by minimizing the reflections from the load (Z_L): $\Gamma = (50 - Z_L)/(50 + Z_L)$ to the source is the same as the resonance condition: $\omega_0 = 1/\sqrt{L_2 C}$. The voltage amplification of this circuit is given by:

$$A_v = \frac{(1 + i\omega/\omega_1)M/L_1}{1 - (\omega/\omega_0\sqrt{1-\kappa^2})^2 + i\omega/\omega_1}. \tag{3.6}$$

Here, $\omega_1 = 1/RC \gg \omega_0$ accounts for the dissipation in the system. The maximal voltage amplification is obtained by finding the maximal value of $|A_v|$:

$$\omega_{max} = \omega_0 \frac{\sqrt{1 - (\omega_0/\omega_1)^2/(1-\kappa^2)/2}}{\sqrt{1-\kappa^2}} \approx \omega_0 \frac{\sqrt{1 - (\omega_0/\omega_1)^2/2}}{\sqrt{1-\kappa^2}}. \tag{3.7}$$

Here, the term in the denominator pulls the frequency which maximizes the voltage amplification to higher values ($\kappa < 1$) just as in our experiment. The term in the numerator however, pulls the frequency down. For quantitative comparison to the experiment a more cumbersome model should be applied as in [72].

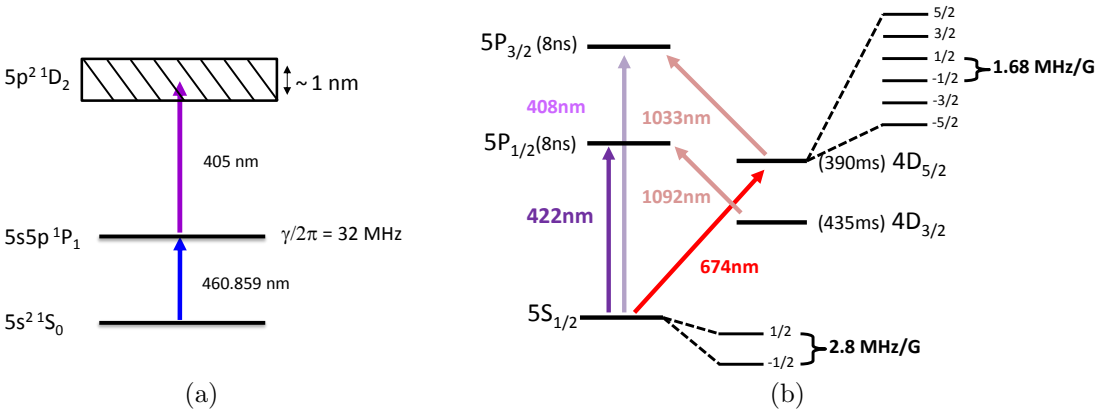

Figure 3.6: **Energy levels** of (a) Sr atom and (b) Sr^+ ion.

3.4 Trapping, cooling and detecting ions

Loading ions into the trap

We load ions into the Paul trap from a home-built neutral Sr atoms oven. The oven is constructed simply from a titanium tube filled with Sr grains[30]. The tube is connected to a vacuum feedthough using copper wires which are also used to align and mount the ovens just underneath the ion Paul trap (see Fig. 2.3b). The trick here is to make the ovens resistance high enough by using a thin wall tube such that most of the power will dissipate in the ovens. The vapor pressure of Sr in room temperature is too low to load ions into the trap. We heat the ovens by passing current through them and a collimated beam of atoms, directed to the center of the trap, emerges.

We photo-ionize Sr atoms using two lasers (see Fig. 3.6a). The first laser is on-resonance with the $^1S_0 \rightarrow ^1P_1$ dipole transition around 461 nm. The second, 405 nm, laser is tuned to a broad auto-ionization level from which the atom decays into a Sr^+ ion and a free electron. When the atom is ionized it is immediately trapped in the Paul trap due to its large and deep capture volume. Below you can find a technical description of the lasers used for photo-ionization:

- **461 nm** - We couple a home-built 922nm ECDL laser (20 mW) to a home-built tapered amplifier which produce 1 W of laser power. The laser is then

[30]Sigma-Aldrich 441899-5G. 99.99% pure Strontium in a vacuum sealed tube. We used Sigma-Aldrich 403326-25G, 99% pure Sr immersed in oil, which is much cheaper, for an atomic reference cell. We cleaned the Sr from residual oil by washing in anhydrous 2-propanol and transferring into vacuum under inert atmosphere. This was done in collaboration with Miri Kazes from Dan Oron's group.

doubled using Toptica SHG module to produce 100 mW of blue light. This laser is locked to a Sr atomic reference using a saturation-absorption technique for absolute frequency stabilization. We focus on-resonance, 0.5mW of laser power to a ∼150 μm spot on the ion.

- **405 nm** - Bare photo-diode[31] with home-built temperature stabilization. We focus 1mW of laser power to ∼400 μm spot on the ion.

The only control on these lasers is by blocking the beam line using a mechanical shutter[32].

Using fluorescence for cooling and detection

When the atom is first ionized, it is trapped in the Paul trap however, it is extremely hot. We cool the ion using 422 nm laser, red-detuned from the $S_{1/2} \rightarrow P_{1/2}$ dipole transition together with a 1092 nm repump laser tuned to the $D_{3/2} \rightarrow P_{1/2}$ dipole transition (see Fig. 3.6b). For initial cooling we use 240 MHz red-detuned light while for Doppler cooling we carefully tune the laser on specific feature of the spectrum. Below you can find a technical description of the lasers used for fluorescence:

- **422 nm** - We use 50μW from Toptica doubled 844nm ECDL stabilized to a Fabry-Perot cavity and locked to atomic reference in the quantum information lab to inject-lock a bare diode in our lab. This way we can get up to 25 mW of narrow and referenced laser power from the slave laser. We use 0.5 mW for off-resonance cooling and up to 10μW for on-resonance cooling and detection. The beam is focused to a 150 μm spot on the ion.

- **1092 nm** - We use half of the light generated in the quantum information lab from a Toptica ECDL laser stabilized to a ULE cavity. We focus 5 μW of laser power to a 250 μm spot on the ion.

We can control these lasers power and frequency by adjusting the rf signal[33] to an AOM in a double-pass configuration. We can turn on and off the laser during the experimental sequence using an rf switch[34].

[31] Sanyo DL5146-101S 40mW diode purchased from Thorlabs for 70$ each.
[32] Uniblitz TS2S.
[33] NovaTech 409B.
[34] MiniCircuits ZASWA-2-50DR+, 10ns switching time.

Collecting photons

The imaging system is designed to collect photons from both the ions (422 nm light) and the atoms (780 nm light). We use a special achromatic objective[35] (f=30 mm) with high numerical aperture (NA=0.38) and long working distance (WD=16 mm). The specification for the focal shift between 422 and 780 nm is 0.2 μm. The confocal design of the imaging allows to block scattered light using an iris from reaching the photon-counter (PC). An additional iris, placed close to the Fourier plane of the imaging system, can be used to reduce aberrations on the expense of reducing the amount of photons collected. A 90:10 beam splitter is used to pass 10% of the light to a CCD[36] which is used to image both the atoms and the ion. The rest of the light is divided using a dichroic mirror. The 422 nm light is directed to the ion's PC[37] while the 780 nm light is directed to the atom's CCD[38]. This CCD is used for absorption imaging of atoms (Sec. 4.3.1). In principle, we can collect signal on all three devices simultaneously.

We measure ion's CCD magnification by using a two ions crystal as a ruler. The distance between two ions in a linear chain (Eq. 2.4.3) is determined by their mass, charge and the trap center-off-mass mode frequency, quantities which we can determine with great accuracy. We found out that each pixel in our imaging system corresponds to 1.02 μm which gives magnification of 10.

To quantify the imaging system collection efficiency (the ratio between number of photons emitted from the ion to the number of photons detected in the PC) we use our ion as a single photon source. We initialize the ion in the meta-stable $D_{3/2}$ state using a short pulse on the $S_{1/2} \rightarrow P_{1/2}$ transition. After scattering on average 17 photons [75] the ion is pumped into the meta-stable $D_{3/2}$ state. We then apply a repump pulse on $D_{3/2} \rightarrow P_{1/2}$ transition. The ion emits a single 422 nm photon and returns to the $S_{1/2}$ electronic ground-state. We repeat this procedure many times to retrieve the total collection efficiency of our detection system (see Fig. 3.8) which is $1 : 179.42(17)$ photons[39].

[35] Lens-Optics special design.
[36] Andor LUCA-S.
[37] Hamamatsu H10682-110.
[38] PCO PixelFly USB.
[39] We performed this experiment on an old configuration of the imaging system. For the present system, the collection efficiency is closer to 1:190.

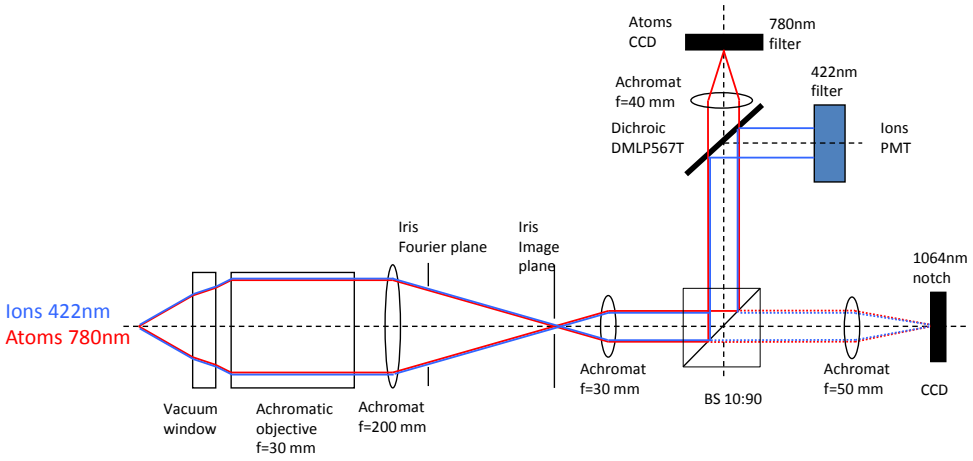

Figure 3.7: **Imaging system.** We collect fluorescence light using a special achromatic objective. The achromatic design allows to image both atoms (780 nm light) and ions (422 nm light) on the same CCD and simultaneously on dedicated atom's CCD and ion's photon-counter. A 10:90 beam splitter is used to pass only 10% of the light to the bichromate CCD. The rest of the light is divided using a dichroic mirror to the ion's photon-counter or the atom's CCD.

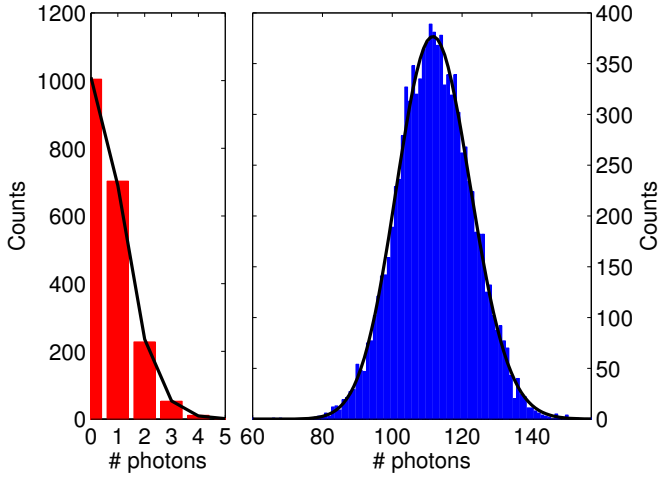

Figure 3.8: **Photon counter collection efficiency.** Histogram of the number of photons detected by the PC after deterministically emitting 20,000 photons (blue) and zero photons (red) from the ion. We repeat the experiment 10,000 times for the bright measurement and 2,000 times for the background measurement. The black curve is a poisson distribution with λ equal to the mean number of photons detected (this is not a fit). This experiment is shot noise limited.

3.5 Article: Cooperative Lamb shift in a mesoscopic atomic array

At this point of my PhD Thesis (Jan. 2013) I decided to sidetrack the main goal of atom-ion experiment and collaborated with Dr. Osip Schwartz from Prof. Dan Oron's group to perform spectroscopic measurement of the cooperative Lamb shift in linear chains of trapped ions [2]. We were the first to observe this small shift in the far-field regime where the ions distances are much larger than the transition wavelength. We were also the first to observe this effect in an ordered and precisely controlled mesoscopic array, and the first to investigate this shift vs. separation.

This work was done with the most elementary tools for ion's spectroscopy: fluorescence from a dipole allowed transition. Even though, we could determine the relative frequency up to few kHz on top of a 20 MHz wide transition. We were able to do so using a technique to probe directly the 2-level spectrum (Lorentzian shape) of a more complicated lambda-level spectrum (see Sec. 3.5.6).

3.5.1 Abstract

According to quantum electrodynamics the exchange of virtual photons in a system of identical quantum emitters causes a shift of its energy levels. Such shifts, known as cooperative Lamb shifts, have been studied mostly in the near-field regime. However, the resonant electromagnetic interaction persists also at large distances, providing coherent coupling between distant atoms. Here, we report a direct spectroscopic observation of the cooperative Lamb shift of an optical electric-dipole transition in an array of Sr^+ ions suspended in a Paul trap at inter-ion separations much larger than the resonance wavelength. By controlling the precise positions of the ions, we studied the far-field resonant coupling in chains of up to eight ions, extending to a length of 40μm. This method provides a novel tool for experimental exploration of cooperative emission phenomena in extended mesoscopic atomic arrays.

3.5.2 Introduction

In quantum electrodynamics, the interaction of individual atoms with electromagnetic vacuum fluctuations brings about spontaneous emission and shifts the atomic energy levels [76]. As pointed out by Dicke [77], the presence of additional proximate atoms changes the character of the radiative decay dynamics dramatically, giving rise to superradiance phenomena and shifting the energy levels of the compound system [78, 79, 80]. Such collective energy level renormalization, known as the cooperative Lamb shift [81, 82, 83, 84], can be thought of as resulting from

an effective resonance interaction, transferring the excitation between individual emitters via emission and reabsorption of virtual photons. In this context, the superradiance effects and the transition frequency shift originate, respectively, from the imaginary and real parts of the resonant dipole-dipole interaction (RDDI).

RDDI has been observed in diverse systems, ranging from an X-ray magnetic dipole transition in ^{57}Fe nuclei [83] to optical dipole-dipole interaction in a gas of Rb atoms [82] to microwave domain transitions in Rydberg atoms [85, 86, 87] and superconducting qubits [88]. In free space, RDDI is predominantly observed as a near-field phenomenon, as the coupling decays cubically with distance when the interatomic separation is much smaller than the transition wavelength [89]. At these small distances, RDDI dominates over relaxation processes, which enabled its observation in pairs of individual quantum emitters such as two fluorescent molecules separated by 12nm, embedded in a dielectric film [90]. The strong near-field RDDI has also been utilized to prevent the transition of more than one Rydberg atom to the excited state, bringing about the phenomenon known as Rydberg blockade [91, 92, 93].

Although RDDI has been mostly studied as a near-field coupling mechanism, it has a long-range term scaling inversely proportional to the distance, which becomes dominant at interatomic separations much greater than the transition wavelength. Detection of RDDI in the far-field regime enables precise measurement of cooperative effects under controlled conditions, in the absence of other types of interactions between the emitters. The far-field coupling regime was first explored by Brewer and DeVoe [94], who detected superradiance in a system of two trapped ions in a Paul trap. Far-field RDDI also plays a central role in a variety of superradiance phenomena, such as the emergence of directionality, which occur in extended mesoscopic samples [95, 96, 97, 98, 99, 100, 101].

Here, we experimentally investigate RDDI in a mesoscopic array of atomic-ions separated by distances much larger than the transition wavelength. To this end we perform a direct spectroscopic measurement of the cooperative Lamb shift of the $5S_{1/2} \leftrightarrow 5P_{1/2}$ optical dipole transition frequency in a system of several Sr^+ ions suspended in a linear Paul trap. Varying the number of trapped ions from two to eight, we carry out the first observation of cooperative emission phenomena in a mesoscopic array of coupled quantum emitters. The high degree of isolation from the environment and the precise control over the positions of emitters achievable in radio-frequency (RF) ion traps allowed for unobstructed detection of cooperative effects even with an array length that extends to approximately a hundred times the resonant wavelength.

3.5.3 Two ions Cooperative Lamb shift

First, we consider cooperative shifts in a system of two trapped ions. A level scheme of the system, taking into account only the ground state $5S_{1/2}$ denoted by $|g\rangle$ and the $5P_{1/2}$ excited state denoted by $|e\rangle$, is shown in Fig. 3.9a. Both states have a total angular momentum of $\hbar/2$, thus each single ion electronic state has two corresponding spin states. The two-ion system therefore has 16 states: four ground states $|gg\rangle$, eight singly-excited states $|eg\rangle \pm |ge\rangle$, and four doubly excited $|ee\rangle$. For the purposes of discussing the energy level arrangement and the cooperative shifts in a two-ion system, we assume that magnetic field is sufficiently small that we can disregard the Zeeman splitting of the levels [102].

In the absence of interaction, all of the eight singly-excited states are degenerate. The RDDI creates a coupling between the singly-excited states and lifts this degeneracy. The resulting energy splitting is the cooperative line shift. The strength of the RDDI is generally given by the expression [79, 89]

$$V_{iq\,js} = \frac{\mathrm{k}^3}{4\pi\epsilon_0\hbar}\left[-\Big(\mathbf{d_{ij}}\cdot\mathbf{d_{qs}} - \big(\hat{\mathbf{r}}\cdot\mathbf{d_{ij}}\big)\,\big(\hat{\mathbf{r}}\cdot\mathbf{d_{qs}}\big)\Big)\frac{\cos(\mathrm{kr})}{\mathrm{kr}} + \right.$$
$$\left. + \Big(\mathbf{d_{ij}}\cdot\mathbf{d_{qs}} - 3\big(\hat{\mathbf{r}}\cdot\mathbf{d_{ij}}\big)\,\big(\hat{\mathbf{r}}\cdot\mathbf{d_{qs}}\big)\Big)\left(\frac{\sin(\mathrm{kr})}{(\mathrm{kr})^2} + \frac{\cos(\mathrm{kr})}{(\mathrm{kr})^3}\right)\right], \quad (3.8)$$

where $\mathbf{d_{ij}}$ and $\mathbf{d_{qs}}$ are the transition dipole moments of the two ions, one transferred from state i to j, and the other from q to s. Here, $k = 2\pi/\lambda$, $\hat{\mathbf{r}}$ is the unit vector in the direction connecting the two ions and r is the distance between them.

The 1/r long-range first term of Eq. (3.8) describes the far-field coupling, whereas the other two correspond to the near-field interactions. At the relatively large inter-ion distances achievable in our ion trap, $\mathrm{r} \simeq 5\mu\mathrm{m} \simeq 12\lambda$, the far-field coupling dominates.

The spin dependence of this interaction can be intuitively explained in terms of emission and absorption of virtual photons. Choosing the spin quantization along the trap axis, one observes that only $\sigma_\pm$ photons can be emitted from one ion towards the other, while π photons are not emitted in this direction. At the same time, momentum conservation requires that the ion spin must be flipped whenever a $\sigma_\pm$ photon is emitted or absorbed. These considerations lead to the energy level splitting shown in Fig. 3.9a. The energy levels of symmetric combinations of the interacting states, $\frac{1}{2}\big(|eg\rangle + |ge\rangle\big)\big(|\uparrow\downarrow\rangle + |\downarrow\uparrow\rangle\big)$ and $\frac{1}{2}\big(|eg\rangle - |ge\rangle\big)\big(|\uparrow\downarrow\rangle - |\downarrow\uparrow\rangle\big)$, are shifted by δ, where

$$\delta\,(\mathrm{r}) = -\frac{3}{8}\mathrm{A}_{\uparrow\downarrow}\frac{\cos(\mathrm{kr})}{\mathrm{kr}} + \mathcal{O}\left(\mathrm{kr}^{-2}\right). \quad (3.9)$$

Here, $\mathrm{A}_{\uparrow\downarrow} = {}^2\!/_3\mathrm{A}_0$ is the oscillator strength of the spin-flipping transition, the factor ${}^2\!/_3$ is a Clebsch-Gordan coefficient, and $\mathrm{A}_0 = 20.05(48)$ MHz is the total

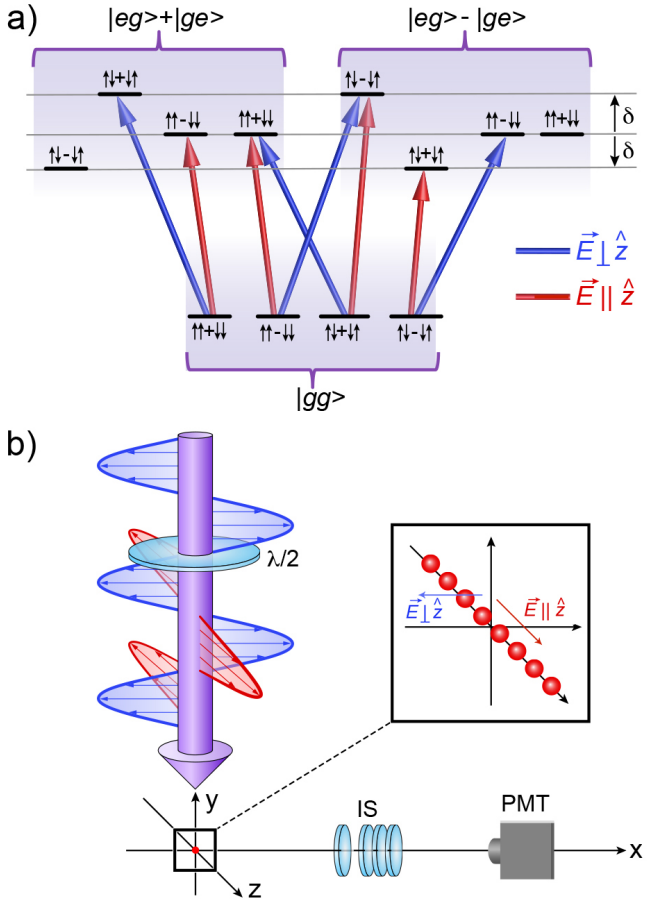

Figure 3.9: **a) Energy level diagram of a two-ion system.** $|g\rangle$ and $|e\rangle$ denote electronic ground and excited states. $(\uparrow)$ and $(\downarrow)$ denote the ion spin projection on the trap axis. The states $\frac{1}{2}\big(|eg\rangle + |ge\rangle\big)\big(|\uparrow\downarrow\rangle + |\downarrow\uparrow\rangle\big)$ and $\frac{1}{2}\big(|eg\rangle - |ge\rangle\big)\big(|\uparrow\downarrow\rangle - |\downarrow\uparrow\rangle\big)$, which turn into themselves upon excitation transfer from one ion to the other $|e\rangle \Leftrightarrow |g\rangle$ and simultaneous spin exchange $\uparrow\Leftrightarrow\downarrow$, are shifted by δ given by Eq.(3.9). The states which acquire a minus sign upon such exchange, $\frac{1}{2}\big(|eg\rangle \pm |ge\rangle\big)\big(|\uparrow\downarrow\rangle \mp |\downarrow\uparrow\rangle\big)$, are shifted by $-\delta$. **b) System geometry.** Two or more Sr^+ ions are trapped in the center of a linear Paul trap (trap electrodes not shown). The ions form a chain along the trap axis $\hat{z}$. A linearly polarized probe beam, propagating along the $\hat{y}$ direction, illuminates the ions uniformly. The probe beam polarization can be rotated using a $\lambda/2$ plate. In our experiments, the beam was polarized either along the trap axis (red arrows), or orthogonal to it, in the $\hat{x}$ direction (blue arrows). The light scattered by the ions was collected by the imaging system (IS) and detected by a photo-multiplier tube (PMT).

oscillator strength of the $5S_{1/2} \leftrightarrow 5P_{1/2}$ transition [103]. The two antisymmetric combinations $\frac{1}{2}\big(|eg\rangle \pm |ge\rangle\big)\big(|\uparrow\downarrow\rangle \mp |\downarrow\uparrow\rangle\big)$, are shifted by $-\delta$. The four singly excited states with parallel spin projections $\frac{1}{2}\big(|eg\rangle \pm |ge\rangle\big)\big(|\uparrow\uparrow\rangle \pm |\downarrow\downarrow\rangle\big)$ do not participate in the far-field interaction and are not shifted.

A probe beam polarized orthogonally to the trap axis causes transitions from the four equally populated ground states to a set of excited states shown by the blue lines in Fig. 3.9a. The resulting mixture of excited states includes two levels shifted by $\delta(\mathrm{r})$ and two unshifted. The center of the observed spectral line is given by the mean shift of the four transitions, $f(\mathrm{r}) = \frac{1}{2}\delta(\mathrm{r})$. If instead the probe beam is polarized along the trap axis, it excites a mixture of states shown by red lines in Fig. 3.9a, of which one is shifted by δ, another by $-\delta$, and the rest are unshifted. In this case, the excited states have zero average shift, and, in contrast to excitation with orthogonal polarization, no line center shift is expected.

The magnitude of the cooperative shift given by (3.9) gives a peak-to-peak frequency shift of $\delta \simeq 130$ kHz at a distance of about 5 μm, much smaller than the natural transition line width $\Gamma_0 = 21.5$ MHz [103]. The shifted and unshifted states of the two-ion system are therefore spectrally unresolved. Nevertheless, the cooperative shift can be probed by detecting the shift of the line center, which can be determined with an accuracy much greater than the linewidth, provided that the resonance spectrum can be measured with a high signal-to-noise ratio.

To measure the resonance line shifts, we used an experimental apparatus shown schematically in Fig. 3.9b. The ions were suspended in a linear Paul trap, cooled close to the Doppler limit and prepared in the $S_{1/2}$ ground state. The distance between the ions was varied by tuning the tightness of the axial confinement in the trap. A weak probe beam close to resonance with the $5S_{1/2} \leftrightarrow 5P_{1/2}$ transition was aligned orthogonally to the trap axis, so that the two ions experienced the same phase of the light wave. The probe beam intensity, stabilized by a feedback circuit, was set well below saturation.

The detection sequence consisted of a cooling and repumping procedure interlaced with an 8μs probe pulse, during which all other light was extinguished and the scattered probe photons were collected by an optical system and detected using a photomultiplier tube. The frequency of the probe beam was scanned across the $5S_{1/2} \leftrightarrow 5P_{1/2}$ transition using an acousto-optical frequency shifter, producing a Lorentzian-shaped line profile with a width of 24.6 MHz. Finding the centroid of the spectral line, we were able to determine the transition frequency with an accuracy of about 50 kHz, limited by the frequency drifts in our apparatus. To overcome this limitation, we resorted to a relative measurement, switching cyclically between different inter-ion distances, spending 30s at every point. The long-term drifts of the system are thus shifting the measured resonance frequency equally for all the measurement points without affecting the relative frequency shift between

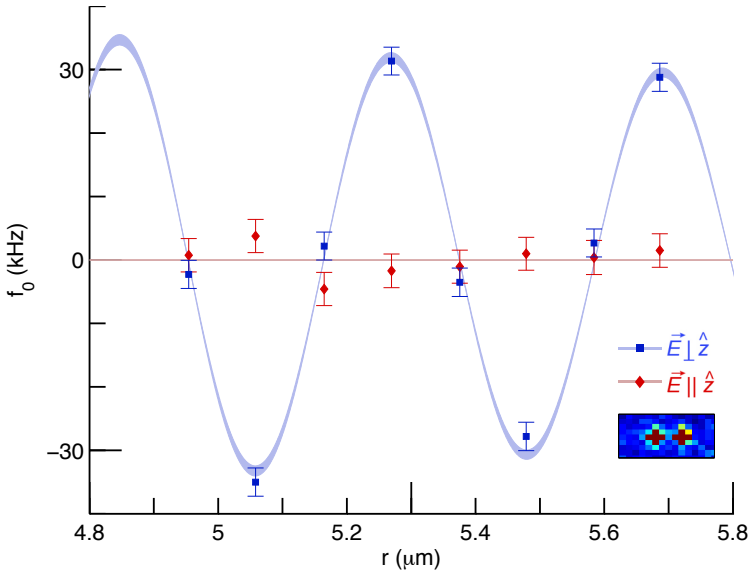

Figure 3.10: **Cooperative line shift in a system of two Sr^+ ions.** The data points show the measured relative frequency shift as a function of distance between the ions. The blue squares and red diamonds correspond to the probe beam polarization orthogonal and parallel to the trap axis, respectively. The light blue line shows the theoretical shift of $\frac{1}{2}\delta(\mathrm{r})$ with $\delta(\mathrm{r})$ given by Eq. (3.9). The width of the line reflects the uncertainty in the oscillator strength value. The error bars represent one standard deviation statistical uncertainty. The observed peak to peak spectral shift is approximately $2 \cdot 10^{-3}$ of the line width.

different distances [102].

The distance dependence of the $5S_{1/2} \leftrightarrow 5P_{1/2}$ transition frequency for two ions is shown in Fig. 3.10. With integration time of 8.6 hours per point, the measurement reached an average statistical uncertainty of 2.2 kHz, which is a factor of 10^4 smaller than the transition line width. Since in our scheme only the relative frequency shifts between distances are measured, the average frequency shift of all distance points was set to the theoretically predicted value of $\bar{f}_0 = \frac{1}{2}\langle\delta(\mathrm{r}_i)\rangle$, where r_i are the distances at which the measurements were carried out. The root-mean-square deviation of the measured points from the theoretical curve of 2.15 kHz suggests no statistically significant discrepancy with theory. We have also performed the cooperative shift measurement with the probe beam polarized along the trap axis, in which case the cooperative shift is predicted to vanish. Indeed, the measurement results shown as red diamonds in Fig. 3.10 demonstrate no distance-dependent frequency shift for the parallel polarization of the probe beam.

The good agreement of data with theory suggests we can use this measurement to extract the magnitude of the oscillator strength. Fitting the perpendicular polarization data to Eq. (3.9) with oscillator strength (A_0) as a single free parameter gives: $A_0^{FIT} = 19.71(88)$ MHz in good agreement with the previously measured value: $A_0 = 20.05(48)$ MHz [103].

3.5.4 Up tp eight ions linear chains

The cooperative shift measurement can be extended to a system of several quantum emitters by loading additional ions into the RF trap. The ions arrange themselves in a line with the axial positions given by $r_m = t_m p$, where t_m are constant normalized distances determined by the competition between the harmonic trap potential and the Coulomb repulsion [104]. The scale coefficient p is controlled by the trap stiffness. The inter-ion distances are determined analytically from the axial center-of-mass mode frequency which we measured independently [102].

Similarly to the case of two ions, the role of the Zeeman structure is reducing the observed cooperative shifts by a factor of 1/2. Disregarding the spin structure, the symmetric excited state of M ions created by the weak probe beam can be described as

$$|\psi\rangle = \frac{1}{\sqrt{M}} \sum_{i=1}^{M} |g_1 \dots e_i \dots g_M\rangle \,, \tag{3.10}$$

and the RDDI Hamiltonian is given by $\hat{V} = \frac{1}{2}\sum_{i\neq j} \delta(r_i - r_j)\left[\sigma_{+i}\sigma_{-j} + \sigma_{-i}\sigma_{+j}\right]$, where $\delta(r)$ is given by Eq. (3.9), $\sigma_{+i} = |e_i\rangle\langle g_i|$ and $\sigma_{-i} = \sigma_{+i}^{\dagger}$. For a chain of $M > 2$ ions, $|\psi\rangle$ is no longer an eigenstate of the interacting system. The observed line shape is given by a weighted sum of Lorentzian resonances, each representing an eigenstate of $\hat{V}$ and shifted by the corresponding eigen-energy. Since the peaks of individual eigenstates are unresolved, the observed line shape is a single Lorentzian-like spectral profile with an apparent shift given by a weighted sum of the eigenstate shifts. This shift can be expressed as the expectation value of the interaction in the excited state [102],

$$\delta_M = \langle\psi|\,\hat{V}\,|\psi\rangle = \frac{1}{M}\sum_{i\neq j} \delta(r_i - r_j). \tag{3.11}$$

The results of the cooperative Lamb shift measurements for three to eight ions are presented in Fig. 3.11a-f. The data are compared to the theoretically predicted distance dependence curves of Eq. (3.11) shown by the light blue lines.

The experimental results demonstrate a good agreement with theory. In the three ion case, the chain being equidistant, the contributions of the three ion pairs

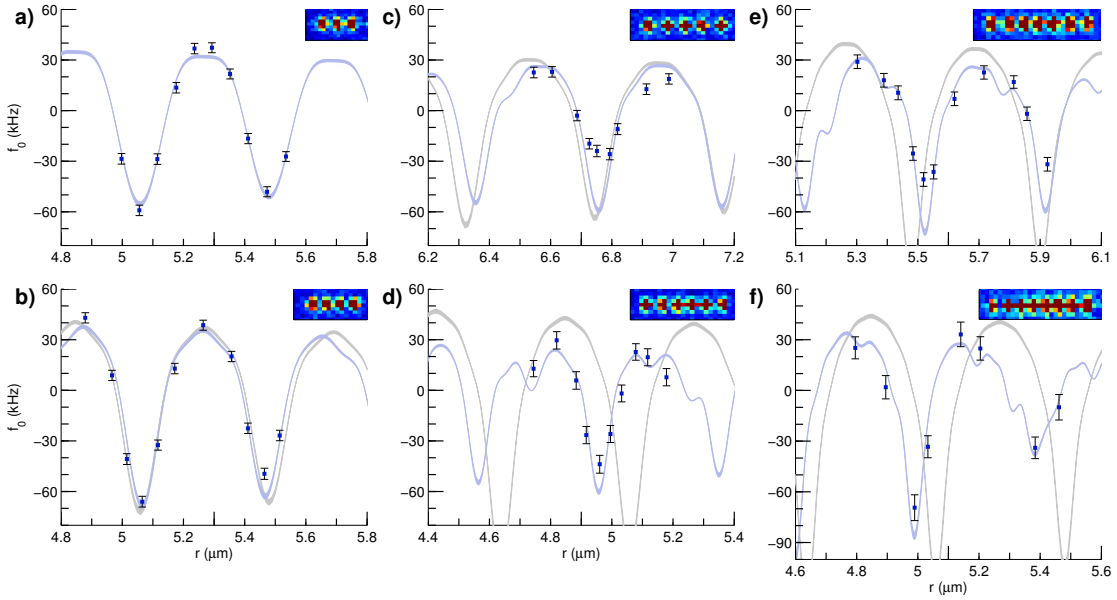

Figure 3.11: **Cooperative shift in a linear chain of several ions.** The panels **a-f** correspond to chains of three to eight ions. In each panel, the cooperative shift is measured as a function of the distance r between two adjacent ions closest to the middle of the chain. The light blue lines show the theoretical shift of Eq. (3.11) [105]. The error bars represent one standard deviation statistical error. Both the shift scale and the distance scale are the same in all panels. The grey lines, shown for comparison, represent the theoretical shift for equidistant chains. The width of theoretical lines represents the uncertainty in the oscillator strength value.

are in-phase and add constructively at periodic intervals, producing sharp peaks in the distance dependence of the line shift. For an equidistant chain of more than three ions, the periodic peaks will grow sharper with increasing number of ions. The predicted line-shift of periodic ion chains is marked by the grey lines in Figs. 3.11b-f. However, in harmonic ion trap a chain of more than three ions is no longer equidistant, so the contributions of different ion pairs have incommensurate spatial frequencies. The distance dependence of the shift thus exhibits beating between the spatial frequencies corresponding to all ion pairs. We chose the distance range in our experiments so as to maximize the visibility of the peaks for a given number of ions.

As the features in the distance dependence of the cooperative shifts get sharper, the position uncertainty caused by thermal motion of the ions becomes significant and causes a washing out of the sharp spectral features. The deviation from theory is more pronounced at larger distances, which require smaller axial trap stiffness leading to a greater position uncertainty. Nevertheless, the fact that the data points follow the sharp features and the nontrivial shapes of the theoretical distance dependence of the shifts demonstrates that the entire ion chain participates in the interaction.

3.5.5 summary

The cooperative line shifts investigated here are closely related to the resonance shifts observed in a system comprising an ion and a mirror [106]. In such a system, instead of interacting with other ions, the ion interacts with its own mirror image, leading to a shift of the resonance frequency [107, 108]. Fundamentally, both types of shifts arise from the same mechanism, i.e., emission and immediate reabsorption of a virtual photon, similarly to the original Lamb shift [76]. The mirror-ion experiments are related to the present work also on another level. Recently, the same group has shown that such ion-mirror systems can form a cavity, with the ion serving as the second cavity mirror [109]. In context of that work, in our experiment the ions can be considered as playing the role of mirrors, reflecting the fields created by other ions.

In summary, we have detected spectroscopically a frequency shift associated with energy transfer between distant atoms. We have demonstrated cooperative effects in which up to eight atomic ions collectively participated. The scope of our work is limited to small emitter arrays and singly-excited states. However, the approach demonstrated here opens the door for spectroscopic studies of larger ion crystals that are common in ion trapping experiments, as well as to investigations of quantum physics beyond single-photon excitations. These experiments open the door to the research of far-field cooperative emission phenomena in controllable mesoscopic systems.

This work was financially supported by the US-Israel Binational Science Foundation, the Crown Photonics Center, ICore - Israeli excellence center "circle of light" and the European Research Council (consolidator grant 616919-Ionology).

3.5.6 SM - Cooperative Lamb shift

Experimental setup

We trap Sr^+ ions in a linear segmented RF Paul trap with inherently reduced RF-driven motion (micromotion) along the crystal axis. The trap radial harmonic frequency is kept at a high setting (1.8 MHz) to reduce the thermal motion amplitude. Excess micromotion amplitude in the radial direction is monitored throughout the experiment and kept below 5nm in the center of the trap. The axial frequency is kept at low settings (250–810 kHz) compared to the radial frequency to keep the linear ion crystal stable. We control the inter-ion distances by changing the trap axial frequency. We measure the axial center-of-mass mode frequency using an external drive on one of the compensation electrodes. The relative frequency uncertainty of this measurement is below 10^{-4} implying that the errors in estimating the equilibrium ion positions do not contribute to the measurement error.

The 422nm light used for cooling and spectroscopy is generated by a bare diode laser injection-locked to a frequency-doubled 844nm external cavity diode laser (ECDL). The 844nm laser is locked to a Fabry-Perot cavity referenced to a Rb absorption line. From the excited $P_{1/2}$ state, the ions can spontaneously decay to the metastable $D_{3/2}$ level (0.5sec lifetime). We use a 1092nm (ECDL referenced to in-vacuum cavity) repump beam on resonance with the $4D_{3/2} \leftrightarrow 5P_{1/2}$ electric dipole transition to return the ions to the $P_{1/2}$ level.

Resolving the line center frequency

The line shape observed with both 422nm ($5S_{1/2} \leftrightarrow 5P_{1/2}$ transition) and 1092nm ($4D_{3/2} \leftrightarrow 5P_{1/2}$ transition) beams turned on simultaneously is complicated due to dark resonances. To restore a simple Lorentzian line shape, we apply a detection sequence composed of an 8μs cooling pulse, during which the off-resonant 422nm cooling beam is turned on together with the 1092nm repump beam, followed by an 8μs detection pulse (Fig. 3.12). During detection, only the weak 422nm probe beam is turned on. During each detection pulse, an average of nine photons are scattered from the entire ion crystal. The probability of transferring an ion to the metastable $D_{3/2}$ level is thus kept moderate.

The observed spectral line profile shown in Fig. 3.13a agrees very well with a Lorentzian line shape. The observed width of the Lorentzian, $\Gamma = 24.63(12)$

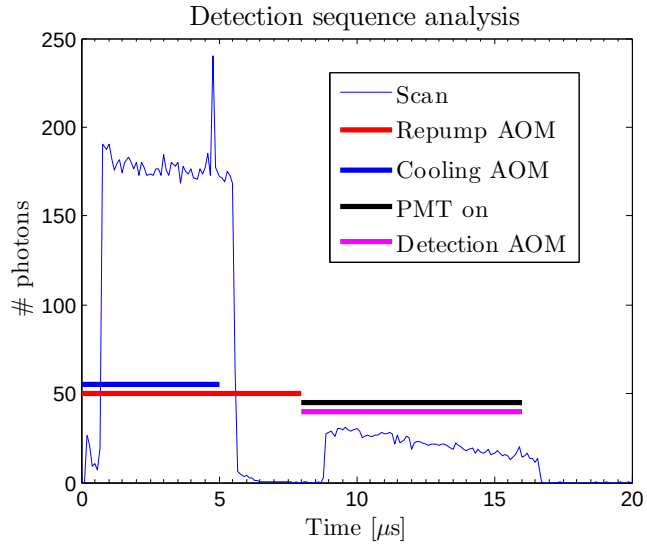

Figure 3.12: **Cooperative Lamb shift detection scheme.** The colored thick stripes indicates the rf-switch signal for the different lasers and the PC acquisition time. The thin blue line is the number of photons collected in 10,000 of these sequences (0.1 μs binning). We turn on the cooling beam (blue stripe) at t=0 sec for 5 μs. The AOM has a 0.8 μs delay due to propagation of the acoustic wave inside the AOM. The repump beam (red stripe) is turned on at t=0 sec for 8 μs. We see a tail of photons reaching our detector until t=6.5 μs. These photons are attributed to events which the ion ended in the $D_{3/2}$ level after the cooling sequence ended. We turn on only the detection beam (magenta stripe) at t=8 μs for 8 μs and count photons. We can scatter on average 17 photons until the ion is pumped to the $D_{3/2}$ dark state. This detection scheme allowed us to measure a clean Lorentzian spectrum (see Fig. 1a in the SM of our article) and eventually to determine the center position with excellent accuracy.

MHz, is slightly larger than the natural line-width due to power broadening, finite magnetic field and population transfer to the $4D_{3/2}$ level.

To measure the central frequency of a Lorentzian line profile most efficiently,

$$\mathrm{L}(\nu) = \frac{\mathrm{A}}{1 + \left(\frac{\nu - f_0}{\frac{\Gamma}{2}}\right)^2} \tag{3.12}$$

we parameterize it with three variables: the center frequency f_0, the line width Γ and the amplitude A. (The background count rate is measured independently and does not contribute to the observed line profile). The three parameters are determined from the measured photon flux values at three spectral points: $\mathrm{L}^0 \equiv \mathrm{L}(f')$, $\mathrm{L}^{\pm} \equiv \mathrm{L}(f' \pm \frac{\Gamma'}{2})$. Here, f' and Γ' are our initial guess for the center frequency (f_0) and the line width (Γ). It is assumed that $f' - f_0 \ll \Gamma$ and $\Gamma' - \Gamma \ll \Gamma$. The central frequency is then determined as

$$f_0 = f' + \frac{\Gamma'}{2}\frac{\mathrm{L}^+ - \mathrm{L}^-}{2(\mathrm{L}^+ + \mathrm{L}^-) - \frac{4\mathrm{L}^+\mathrm{L}^-}{\mathrm{L}^0}} \approx f' + \frac{\Gamma'}{2}\frac{\mathrm{L}^+ - \mathrm{L}^-}{\mathrm{L}^0} \tag{3.13}$$

In this scheme, the statistical measurement uncertainty is $\Delta f_0 = \frac{1}{2}\frac{\Gamma}{\sqrt{N}}$, where N is the total number of photons detected, thus improving as a square root of photon collection time. However, as the interrogation time is increased, the frequency drifts in the system accumulate, eventually forestalling further improvement of the measurement accuracy. To overcome this limitation, we resort to a relative measurement, switching cyclically between different inter-ion distances, spending 30s at every point. The long-term drifts of the system are thus shifting the measured resonance frequency equally for all the measurement points without affecting the relative frequency shift between different distances.

The results of a typical relative shift measurement are illustrated in Fig 3.13b. The graph shows a histogram of 93300 individual measurements of the relative frequency shift of two different inter-ion distances conducted over 30.4 hours. On average, $n = 662$ photons were detected in each measurement at each distance point. The histogram demonstrates a near-perfect agreement with a Gaussian fit with a standard deviation of 0.4963(12)MHz, which is close to the expected root-mean-square deviation of $\frac{\Gamma}{2\sqrt{n}} = 0.469$MHz. The difference in resonance frequency between the two inter-ion distances (f_0) is measured to be 50.6 ± 1.6 kHz as marked by the red vertical line. To demonstrate the ability of our interlacing technique to detect frequency shifts with kilohertz accuracy, we conducted an Allan variance analysis on the same data set. Fig. 3.13c shows the uncertainty of the central frequency as a function of integration time for both the drift-limited frequency measurement and the frequency shift between two distance points. The graph shows that for the non-interlaced frequency measurement, the accuracy

stops improving after reaching uncertainty of about 50 kHz. In contrast, the Allan variance of the relative frequency measurement demonstrates no deviation from shot noise limited uncertainty throughout the duration of the experiment, reaching a measurement uncertainty of 2.4 kHz, which amounts to about 10^{-4} of the transition line width.

Computing the observed line shift for more than two ions

For M non-interacting ions the Hilbert space of the system is spanned by 2^{M} eigenstates with M+1 energetically-degenerate subspaces. We focus our attention on the M-dimensional subspace of singly-excited states of the form $|\psi_i^0\rangle = |g_1 ... e_i ... g_M\rangle$ (disregarding the spin degrees of freedom). The RDDI interaction Hamiltonian $\hat{V}$ does not mix different degenerate subspaces, hence we may consider its effect only on the relevant singly-excited subspace.

Our system is prepared in the symmetric state of the singly-excited subspace, the so-called W-state,

$$|\psi\rangle = \frac{1}{\sqrt{\mathrm{M}}} \sum_{\mathrm{i}} |\mathrm{g}_1 \ldots \mathrm{e}_\mathrm{i} \ldots \mathrm{g}_\mathrm{M}\rangle \tag{3.14}$$

which is not an eigenstate of the interacting system for $M > 2$. The observable line shape can be calculated using master equation formalism [Ref. 4 in the main text]. In the leading order, the line shape is reduced to a weighted sum of Lorentzian profiles corresponding to the eigenstates of the interaction,

$$I(\nu) = \sum_i L(\nu - \nu_i) \left|\langle\psi|\psi_i\rangle\right|^2, \tag{3.15}$$

where $L(\nu)$ is the Lorentzian spectral shape and $|\psi_i\rangle$ are the eignestates of $\hat{V}$ with eigen-energies ν_i,

$$\hat{V} |\psi_i\rangle = \nu_i |\psi_i\rangle . \tag{3.16}$$

Taking into account that $\nu_i \sim 10^{-3}\Gamma$, i.e. the width of each Lorentzian overwhelms the shifts, the total lineshape $I(\nu)$ appears as a single shifted Lorentzian-like spectral profile. The shift of the centroid of the spectal line (δ_M) is given by a weighted sum of ν_i,

$$\delta_\mathrm{M} = \sum_i \nu_i \left|\langle\psi|\psi_i\rangle\right|^2 = \langle\psi| \left(\sum_i |\psi_i\rangle \nu_i \langle\psi_i| \right) |\psi\rangle = \langle\psi| \hat{V} |\psi\rangle . \tag{3.17}$$

This expression shows that the observable average shift of the line shape is just the expectation value of the interaction operator in the excited state, which, using

$\hat{V}$ from the main text and $|\psi\rangle$ from Eq. (3.14), is found to be

$$\begin{aligned}\delta_{\mathrm{M}} &= \frac{1}{2\mathrm{M}}\sum_{\mathrm{i}}\langle g_1...e_{\mathrm{i}}...g_{\mathrm{M}}|\sum_{k\neq l}\delta\left(\mathrm{r_k}-\mathrm{r_l}\right)\left[\sigma_{+\mathrm{k}}\sigma_{-\mathrm{l}}+\sigma_{-\mathrm{k}}\sigma_{+\mathrm{l}}\right] \\ &\times\sum_{\mathrm{j}}|g_1...e_{\mathrm{j}}...g_{\mathrm{M}}\rangle=\frac{1}{\mathrm{M}}\sum_{\mathrm{i}\neq\mathrm{j}}\delta\left(\mathrm{r_i}-\mathrm{r_j}\right), \qquad (3.18)\end{aligned}$$

arriving to Eq. (4) of the main text.

Magnetic field

Although in our analysis we neglected the magnetic field, the experiment was performed in the presence of a weak (about 1G) magnetic field applied in the direction orthogonal to the trap axis, which allowed us to avoid optical pumping of the ions during the cooling pulses. While the magnetic field contributes to the spectral line broadening, it does not lead to a shift of the line center since the ions are initially unpolarized. At the same time, any residual polarization of the ions that might lead to a Zeeman shift of the line would not depend on the distance between the ions and thus would not be observable in our experiments.

3.6 Coherent control

Our main tool for controlling the ion's motional state and spin, which allows us to cool the ion to the ground-state, prepare it in a specific spin state and reduce its excess-micromotion (EMM), is a narrow line-width laser (100Hz) on an optical quadrupole transition (see Fig. 3.6b for the ion's energy scheme). Due to the long lifetime of the meta-stable D level (390ms) we can perform coherent manipulation of the ion between its electronic ground-state and excited-state. The static magnetic field in our system (2.8G) separates the different Zeeman levels of the ground and excited-states by a few MHz such that addressing individual Zeeman levels is easily achieved.

The narrow laser system is based on a Toptica ECDL with extended arm referenced to an ultra-low-expansion (ULE) in-vacuum cavity. The light transmitted from the cavity is used to inject-lock a bare diode. We pass the injected diode's beam through an AOM which follows another in-vacuum and temperature stabilized cavity. This entire system is positioned in the quantum information lab. We use 50 μW of the narrow signal to inject lock additional bare diode which produce 50 mW laser power. The laser is passed through AOMs for switching and controlling its power and frequency and through a set of polarizing beam splitters and motor-driven waveplates which direct the laser beam into one of three ports (see

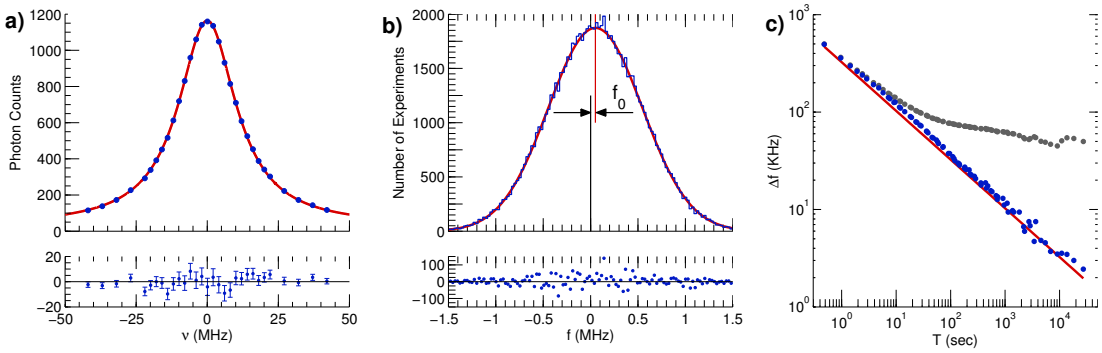

Figure 3.13: **Frequency shift measurement strategy**. **a)** Line shape of the $5S_{1/2} \leftrightarrow 5P_{1/2}$ optical electric dipole transition. The ion fluorescence intensity is plotted as a function of the laser frequency detuning ν. The red line shows a Lorentzian fit. The difference between the experimental data points and the fit are shown in the graph underneath. **b)** Frequency shift histogram. The blue line shows a histogram of 93300 measurements of the frequency shift between two different ion spacings. The red curve shows a Gaussian fit. The vertical red line shows the centroid of the distribution, which is displaced from zero by $f_0 = 50.6 \pm 1.6$ kHz. The lower panel shows the differences between the histogram and the fit. **c)** Allan variance. The measurement uncertainty is plotted as a function of signal accumulation time for the frequency measurements at a single inter-ion distance (grey) and for the frequency difference between two inter-ion distances (blue). The single distance measurement accuracy is limited to about 50 kHz due to system frequency drifts. The uncertainty of the frequency difference follows the photon shot-noise limited scaling (red line) throughout the duration of the experiment.

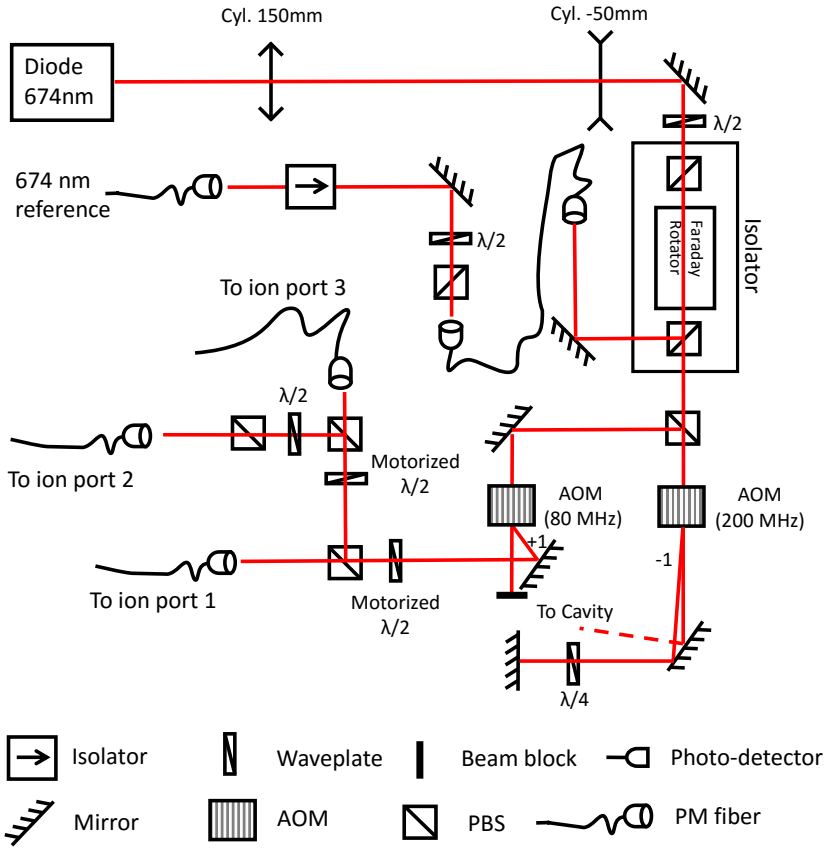

Figure 3.14: **Narrow laser slave system.**

Fig. 3.14). We use three ports for EMM compensation in all three axes of our ion's motion (Sec. 3.6.3). Switching between the ports takes a few seconds. This slow switching time is acceptable since we perform compensation on hourly basis while during the experiment we use only a single port. A scheme of all ion's lasers beam surrounding the vacuum chamber is depicted in Fig. 3.15.

Together with the narrow linewidth laser we use a 1033 nm repump on the $D_{5/2} \rightarrow P_{3/2}$ dipole allowed transition. This is a Toptica ECDL locked to in-vacuum cavity. We use half of the light created in the quantum information lab.

3.6.1 Rabi spectroscopy

The derivation of laser-atom interaction can be found in many textbooks. I will follow D. Leibfried [60] derivation with minor changes[40]. The ion Hamiltonian

[40]Mainly, generalization to three modes.

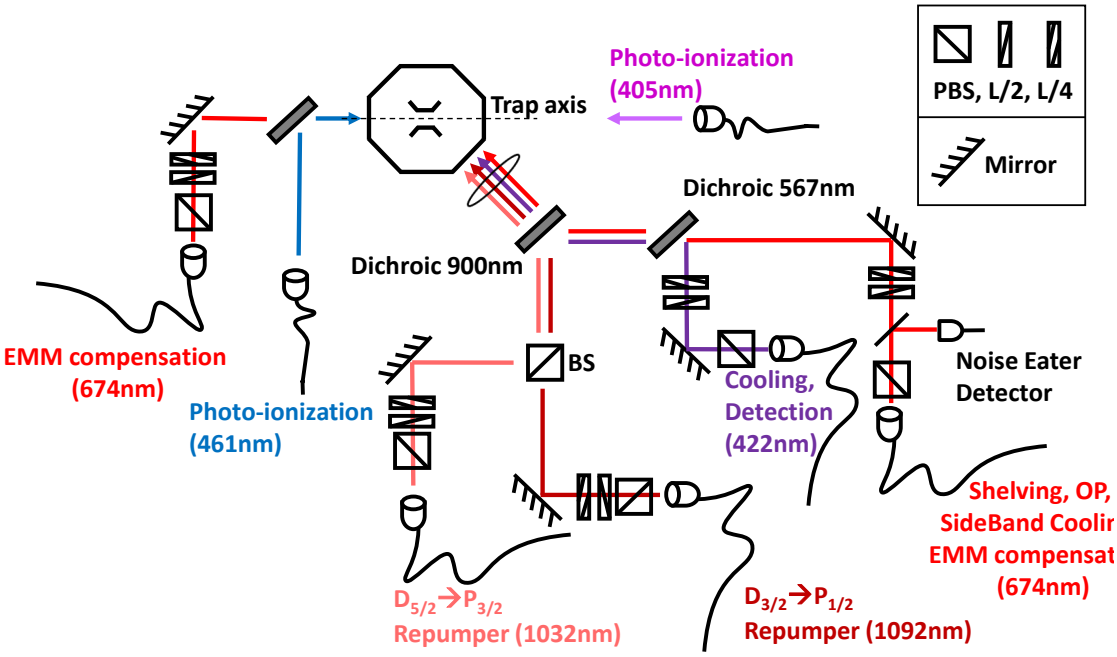

Figure 3.15: **Sketch of the beam lines passing through the ion's chamber.** We use polarization-maintaining (PM) fibers to dis-entangle the ion's beam alignment from the lasers and switching system. Most of the beams are delivered from single port which makes alignment easier by using an iris outside the vacuum in the approximate location of the ion. This iris is used to overlap the beams on a single point. Then we can steer all the beams together using a single lens. We can control the lasers polarization using a PBS and two wave plates. The ionization lasers are oriented along the trap axis, perpendicular to the Sr oven. When the 405nm laser is aligned on the ions we see quantum jumps to the $P_{3/2}$ level. We align the 461nm laser such that it is coupled to the 405nm fiber. We monitor the 674 nm light power and stabilize it using a noise-eating servo. Two additional 674 nm ports (only one is shown) are used for excess-micromotion detection and compensation.

is composed of electronic part: $\hat{\mathrm{H}}^{(e)} = \hbar\frac{\omega_0}{2}\hat{\sigma}_z$ (Here, ω_0 is the energy difference between the ground and excited states and $\hat{\sigma}_z$ is the Pauli operator) and a motional part which is in general described by the Mathieu equations but after neglecting the fast micromotion terms can be written as $\hat{\mathrm{H}}_i^{(m)} = \hbar\nu_i(\hat{a}_i^\dagger\hat{a}_i + \frac{1}{2})$ (Here, ν_i is the mode frequency (i=x,y,z) and $\hat{a}^\dagger(\hat{a})$ are the raising (lowering) operators). The full Hamiltonian is given by: $\hat{\mathrm{H}} = \hat{\mathrm{H}^{(e)}} + \sum_i \hat{\mathrm{H}}_i^{(m)} + \hat{\mathrm{H}}^{(i)}$. $\hat{\mathrm{H}}^{(i)} = \frac{\hbar}{2}\Omega\hat{\sigma}_x(e^{i(\mathbf{k}\hat{\mathbf{x}}-\omega t+\phi)} + e^{-i(\mathbf{k}\hat{\mathbf{x}}-\omega t+\phi)})$ couples the light field[41] and the atom. Here, Ω is the on-resonance Rabi frequency, $\mathbf{k}$ is the laser wave vector[42], ω is the laser frequency and $\hat{\mathrm{x}}_i = \sqrt{\frac{\hbar}{2m\nu_i}}(\hat{a}_i + \hat{a}_i^\dagger)$ is the position operator.

Next, we move to the interaction picture with free Hamiltonian $\hat{\mathrm{H}}_0 = \hat{\mathrm{H}^{(e)}} + \sum_i \hat{\mathrm{H}}_i^{(m)}$. In this picture the interaction Hamiltonian takes the form: $\hat{\mathrm{H}}_{\mathrm{int}} = e^{i/\hbar\hat{\mathrm{H}}_0^\dagger t}\hat{\mathrm{H}}^{(i)}e^{-i/\hbar\hat{\mathrm{H}}_0 t}$. After performing the rotating-wave approximation which neglects fast oscillating terms we are left with:

$$\hat{\mathrm{H}}_{\mathrm{int}} = \frac{\hbar}{2}\Omega_0\hat{\sigma}_+\exp\{i\sum_i \eta_i(\hat{a}_i e^{-i\nu_i t} + \hat{a}_i^\dagger e^{i\nu_i t})\}e^{(i(\phi-\delta t))} + \mathrm{H.c.} \tag{3.19}$$

Here, $\hat{\sigma}_+ = \frac{1}{2}(\hat{\sigma}_x + i\hat{\sigma}_y)$ is the electronic raising operator. $\eta_i = \mathrm{k}_i\sqrt{\frac{\hbar}{2m\nu_i}}$ is the Lamb-Dicke parameter for the i-th mode (k_i is the projection of the laser k-vector along the mode i), $\delta = \omega - \omega_0$ is the laser detuning from resonance and $\Omega_0 = \Omega/\prod_i(1 + q_i/2)$ is the scaled interaction strength due to micromotion breathing (see Eq. 69 in Ref. [60]).

The interaction Hamiltonian in Eq. 3.19 can be further simplified in the so-called Lamb-Dicke regime where the extension of the ion's wavefunction is much smaller than the laser wavelength:

$$\hat{\mathrm{H}}_{\mathrm{LD}} = \frac{\hbar}{2}\Omega_0\hat{\sigma}_+\{1 + i\sum_i \eta_i(\hat{a}_i e^{-i\nu_i t} + \hat{a}_i^\dagger e^{i\nu_i t})\}e^{i(\phi-\delta t)} + \mathrm{H.c.} \tag{3.20}$$

By setting the laser detuning on-resonance with the ground to excited energy $\delta = \omega - \omega_0 = 0$, we can excite the "carrier" transition which does not change the ion motional state: $|n_i; g\rangle \rightarrow |n_i; e\rangle$. In our experiment we use this transition to measure the ion's temperature (see Sec. 3.6.2). Alternatively, we can set the laser detuning on-resonance with one of the motional-modes $\delta = \pm\nu_i$. These transitions couples between the electronic state and motional state of the ion: $|n_i; g\rangle \rightarrow |n_i \pm 1; e\rangle$. Blue (red) detuning of the laser excites "blue sidebands"

[41] We treat the laser as classical field.
[42] $\mathrm{k} = \frac{2\pi}{\lambda}$ with λ=674nm.

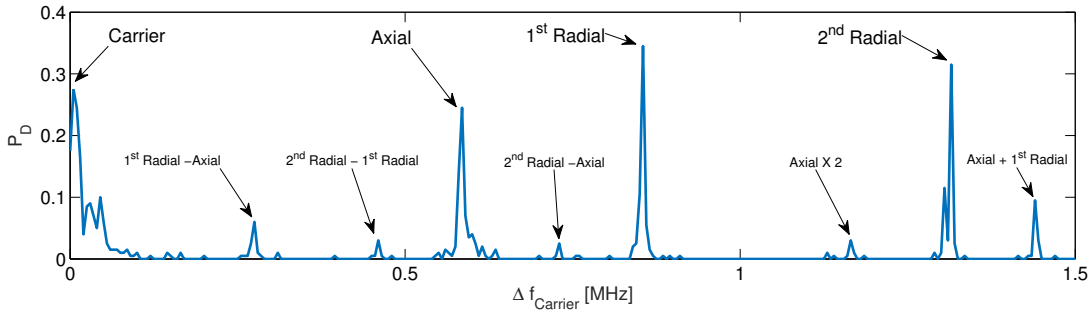

Figure 3.16: **Ion's mode spectroscopy.** We scan the detuning of the 674nm laser and measure the population in the excited state (D level) after a short pulse. We trace each peak in the spectrum to a specific expansion of Eq. 3.19. The ion's mode frequencies are: 580kHz, 0.85kHz and 1.3MHz.

("red sidebands") transitions. The "red sidebands" are used for cooling the ion to its ground-state.

We can take the second order expansion in the Lamb-Dicke parameter of Eq. 3.19. This will lead to two-phonon transitions which can also mix between the different modes of the ion (See Fig. 3.16).

3.6.2 Ion thermometry

As discussed in Sec. 3.6, depending on the laser detuning, Eq. 3.19 can change the motional state while coupling the electronic states. The coupling strength is given by [60]:

$$\Omega_{n,n+s} = \Omega_0 |\langle n+s| e^{i\eta(\hat{a}+\hat{a}^\dagger)} |n\rangle|. \tag{3.21}$$

For the special case of s=0 ($\delta = 0$) we do not excite any motional states and the coupling for three dimensions, can be written as:

$$\Omega_{n_x n_y n_z, n_x n_y n_z} = \Omega_0 \prod_i e^{-\frac{\eta_i^2}{2}} \mathrm{L}_{n_i}\left(\eta_i^2\right). \tag{3.22}$$

Here, $\mathrm{L}_n(x)$ is the Laguerre polynomial of degree n.[43] Eq. 3.22 can be expanded in Taylor series of η which gives the well known carrier coupling: $\Omega_{n,n} \approx \Omega_0(1 - \eta^2(n+\frac{1}{2}))$. Note that for large n's (typically, n>100) this commonly used formula is inadequate.

[43] $\mathrm{L}_n(x) = \sum_{m=0}^{n}(-1)^m \binom{n}{n-m}\frac{x^m}{m!}$. Since evaluating L_n for large n's involves calculation of large factorials, an easy method for calculating the Laugerre polynomial is to use the recursion formula: $\mathrm{L}_0(x) = 1$, $\mathrm{L}_1(x) = 1 - x$, $\mathrm{L}_{k+1}(x) = \frac{(2k+1-x)\mathrm{L}_k(x) - k\mathrm{L}_{k-1}(x)}{k+1}$.

The probability of populating the electronic excited-state is given by $\mathrm{P}_e(t) = \sin^2(\Omega_{n,n}t)$ assuming the ion is initialized in the electronic ground-state. However, this is true only if the ion is in a definite Fock-state, n. It is more likely that the ion has some distribution (in general a density matrix) of phonons. In the case of a thermal distribution[44] with no correlation (zero off-diagonal elements in the density matrix) the probability to occupy n-level is: $\mathrm{P}_{\bar{n}_i}(n_i) = \frac{1}{\bar{n}_i+1}\left(\frac{\bar{n}_i}{\bar{n}_i+1}\right)^{n_i}$ such that the excited-state probability is given by:

$$\mathrm{P}_e(t;\bar{n}_x,\bar{n}_y,\bar{n}_z) = \sum_{n_x,n_y,n_z} \mathrm{P}_{\bar{n}_x}(n_x)\mathrm{P}_{\bar{n}_y}(n_y)\mathrm{P}_{\bar{n}_z}(n_z)\sin^2(\Omega_{n_xn_yn_z,n_xn_yn_z}t). \quad (3.23)$$

The ion temperature is given by: $\mathrm{k_B T}_i = \frac{\hbar\nu_i}{\ln(\frac{\bar{n}_i+1}{\bar{n}_i})}$ [60][45]. In the case of a single ion with no coupling between the modes the equipartition theorem doesn't hold and each mode could acquire a different temperature. However, immediately after laser cooling all the modes are thermalized such that we can assign a single temperature for the ion: $\mathrm{T}_i = \mathrm{T}\ \forall\, i$.

Evaluating Eq. 3.23 for a distribution with large n's, which is the case for the power-law distribution after atom-ion collisions, is highly demanding. To speed numerical calculation time, we change from a 3D sum to 1D integral by switching to continuous total energy, instead of discrete states, distribution:

$$\mathrm{P}_e(t;\{x\}) = \int_{\mathrm{E}} \mathrm{P}_{\{x\}}(\mathrm{E})\sin^2(\Omega_{\mathrm{E}}t). \quad (3.24)$$

Here, $\mathrm{E}= \sum_i \hbar\nu_i(n_i + 1/2)$ is the total energy and $\{x\}$ are the distribution parameters. The single temperature thermal distribution is now: $\mathrm{P}\,(\mathrm{E}) = \frac{\mathrm{E}^2}{2\mathrm{T}^3}e^{-\mathrm{E}/\mathrm{T}}$ where the E^2 term accounts for the density of states of 3D harmonic oscillator and T is the parameter which defines the distribution. Now, we can also calculate the excited-state probability for a Tsallis distribution (Eq. 5.1) and compare our results to the experimental data (Ch. 5).

3.6.3 Excess micromotion minimization

Following Berkeland [42] we consider a laser field in the rest frame of the ion undergoing excess-micromotion (EMM):

$$\mathbf{E}(t) = \mathrm{Re}[\mathbf{E}_0 \exp\left(i\mathbf{k}\cdot(\mathbf{u}_0 + \mathbf{u}_{\mathrm{EMM}}) - i\omega_{laser} + \phi_{laser}\right)], \quad (3.25)$$

[44]The Boltzmann distribution follows: $\mathrm{P}(\epsilon_n) \propto e^{-\epsilon_n/\mathrm{k_B T}}$ with $\epsilon_n = \hbar\omega(n+\frac{1}{2})$ for harmonic oscillator.

[45]In the classical limit where $\bar{n}_i \gg 1$ the equipartition theorem holds and the temperature is equal to the total average energy: $\mathrm{k_B T}_i \approx \hbar\nu_i(\bar{n}_i + \frac{1}{2})$.

where $|\mathbf{u}_{\mathrm{EMM}}|$ is the amplitude of EMM and $|\mathbf{u}_0|$ is the amplitude of secular motion. The laser field undergoes FM modulation: $\mathbf{k}\cdot\mathbf{u}_{\mathrm{EMM}}(t) = \beta\cos(\Omega t+\delta)$, with the modulation index:

$$\beta = \sqrt{\left(\sum_i \mathrm{k}_i \mathrm{u}_i^{\parallel}\right)^2 + \left(\sum_i \mathrm{k}_i \mathrm{u}_i^{\perp}\right)^2}, \tag{3.26}$$

and phase shift:

$$\delta = \tan^{-1}\left(\frac{\sum_i \mathrm{k}_i \mathrm{u}_i^{\perp}}{\sum_i \mathrm{k}_i \mathrm{u}_i^{\parallel}}\right) - \frac{\pi}{2}. \tag{3.27}$$

Here, $\mathbf{u}_{\mathrm{EMM}} = \mathbf{u}^{\parallel}\cos(\Omega t) + \mathbf{u}^{\perp}\sin(\Omega t)$ such that $|\mathbf{u}^{\parallel}|$ is the micromotion amplitude which oscillates in-phase with the trap rf frequency and $|\mathbf{u}^{\perp}|$ oscillates with 90 degrees phase shift (quadrature) to the rf frequency.

We can re-write Eq. 3.25 in terms of infinite Bessel function series:

$$\mathbf{E}(t) = \mathrm{Re}[\mathbf{E}_0 e^{i\mathbf{k}\cdot\mathbf{u}_0}\sum_n \mathrm{J}_n(\beta)e^{in(\Omega t+\delta+\pi/2)-i\omega_{laser}+\phi_{laser})}], \tag{3.28}$$

from which we can deduce a resonance condition: $\omega_{laser} = \omega_0 + n\Omega$. Since the modulation index is always small ($\beta < 0.1$) we expect only the first sideband ($n = \pm 1$) to appear in the spectrum. Our method of detecting EMM is based on this resolved sideband spectroscopy of the sidebands. By comparing the Rabi frequency of the carrier (Ω_0) and the EMM sideband (Ω_1) we can extract the modulation index:

$$\frac{\Omega_1}{\Omega_0} = \frac{\mathrm{J}_0(\beta)}{\mathrm{J}_1(\beta)} \approx \frac{\beta}{2}, \tag{3.29}$$

from which we can extract the EMM amplitude along the laser $\mathbf{k}$-vector:

$$|\mathbf{u}_{\mathrm{EMM}}| = \frac{\beta\lambda}{2\pi} = \frac{\Omega_1\lambda}{\Omega_0\pi}. \tag{3.30}$$

We detect EMM in our system using three 674 nm detection beams (see Fig. 3.14 and 3.15) each beam detects the projection of EMM amplitude along the beam direction.

Systematic shifts

This method is based on detecting a modulation of the energy difference between the ground and excited states in the rf frequency. In the case of EMM, the Doppler shift associated with the ion's oscillatory motion induce this energy modulation. However, any other source of rf frequency modulation of the energy levels will also be detected as EMM signal. We call all these sources - "systematic shifts"

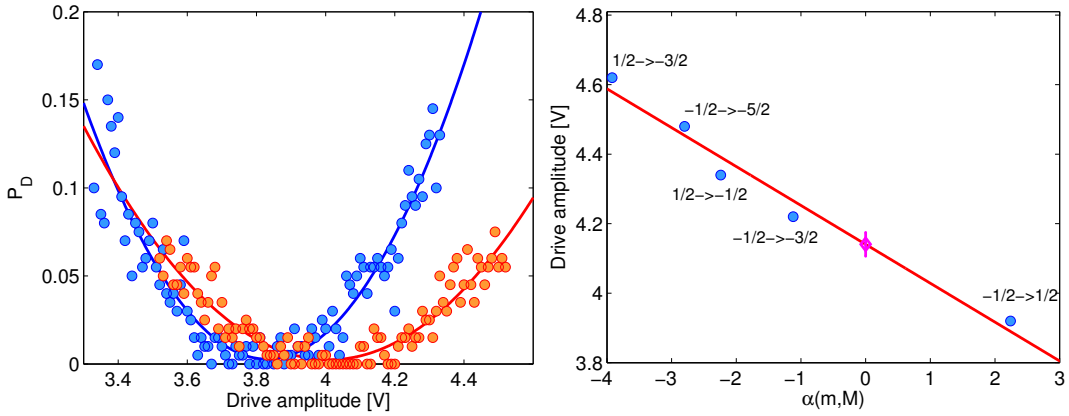

(a) (b)

Figure 3.17: **Systematic shifts** a) Excited state population after 400 μs pulse on the EMM sideband as function of the compensation electrode value (in this case, the axial EMM drive amplitude). In red we flop on the $S_{-1/2} \rightarrow D_{-3/2}$ Zeeman sublevels and in blue on the $S_{1/2} \rightarrow D_{3/2}$. Solid line is a fit to a parabola. b) Compensation value for different Zeeman transitions ($\alpha(\mathrm{m}, \mathrm{M}) = -2.802\mathrm{m} + 1.680\mathrm{M}$ [MHz/G] is the $S_{1/2} \rightarrow D_{5/2}$ Zeeman susceptibility as illustrate in Fig. 3.6b). Line is a linear fit. Purple circle indicates the compensation value for no Zeeman shifts ($\alpha = 0$).

and their magnitude is usually much smaller than the EMM signal. Since the systematic shifts depend on the Zeeman structure while the Doppler shift doesn't, we can distinguish between the EMM signal and the systematic shifts by comparing different Zeeman sub-levels (Fig. 3.17).

The main contribution for the systematic shifts is the ac-Zeeman shift. This shift is induced by rf currents in the trap electrodes which results in oscillating magnetic fields in the trap center. In practice, we determine the EMM compensation value from the mean of measurement on two opposite Zeeman sublevels.

Radial compensation

We perform EMM compensation in the radial plane using two dc compensation electrodes (see Fig. 3.1a) and two detection beams with projections on the radial plane. For minimizing EMM it is sufficient to find dc values which reduce the coupling to the EMM sidebands for both beams simultaneously. This is done with an iterative scheme which converges fast, however, we can't determine using this approach the residual EMM in our system when the Rabi π-time becomes

longer than our coherence time[46]. In this case, the residual Rabi frequency for the compensated point can no longer be reliably evaluated[47].

A more elaborate analysis of the radial EMM in our system is shown in Fig. 3.18. In this experiment we deliberately create a large micromotion amplitude such that the Rabi π-time on the micromotion sideband is shorter than our coherence time. By fitting the Rabi flopping on the carrier and sideband we can extract the ions micromotion amplitude. Measuring the amplitude for different compensation voltages we can extrapolate the compensated voltage and ion minimal amplitude by fitting to a simple model in which the total micromotion amplitude is composed from two linearly independent components, in-phase (Sec. 2.4.1) and quadrature (Sec. 2.4.2) EMM:

$$|\mathbf{u}_{j\,\mathrm{EMM}}| = \sqrt{(\tilde{\gamma}_j(\mathrm{V}-\mathrm{V}_0))^2 + |\mathrm{u}_j^{\perp}|^2}. \tag{3.31}$$

Here, $|\mathrm{u}_j^{\perp}|$ is the projection on the radial plane of the quadrature micromotion on the laser k-vector. By varying only dc compensation voltages this micromotion component can't be compensated and therefore sets a minimum to the excess micromotion. We found that $|\mathrm{u}_j^{\perp}| \approx 1$ nm in both radial directions which corresponds to total average kinetic energy of about 200μK. The first term in Eq. 3.31 is the projection on the radial plane of the in-phase micromotion which can be nulled (V=V_0) using the dc compensation electrodes.

Far from the EMM compensated point, micromotion amplitude grows linearly with the dc compensation voltage: $|\mathbf{u}^i_{j\,\mathrm{EMM}}| = \tilde{\gamma}^i_j(\mathrm{V}^i - \mathrm{V}^i_0)$. Here, the i-index corresponds to which compensation electrodes is being altered. We can read the slope from the graphs: $[\tilde{\gamma}_y^{\mathrm{RF}}, \tilde{\gamma}_x^{\mathrm{RF}}, \tilde{\gamma}_y^{\mathrm{GND}}, \tilde{\gamma}_x^{\mathrm{GND}}]$=$[7.478\pm0.058, 2.630\pm0.032, 1.876\pm 0.082, 4.586\pm0.033]$ nm/V (x,y corresponds to different laser beam directions) and compare this measurement to the simulated value from Sec. 3.1:

$$\tilde{\gamma}^i = \sqrt{\sum_j \tilde{\gamma}_j^{i2}} = \frac{e\mathrm{E}_{\mathrm{CPO}}}{m\omega_i^2}\frac{q_i}{2}. \tag{3.32}$$

Where $\mathrm{E}_{\mathrm{CPO}} \approx 6.27$ [1V/m] is the value extracted from numerical simulation. Inverting Eq. 3.32 we get $\mathrm{E}_{\mathrm{Exp}} \approx 4.3$ [1V/m] in relatively good agreement.

We use this measurement to calibrate the amount of EMM energy injected into our system due to deliberately or dc uncompensated value:

$$\gamma^i \equiv \frac{\mathrm{T}_{\mathrm{EMM}}}{\left(\mathrm{V}^i - \mathrm{V}^i_0\right)^2} = m\left(\frac{\tilde{\gamma}^i\Omega_{\mathrm{RF}}}{2}\right)^2/\mathrm{K_B} \tag{3.33}$$

[46]The coherence time is mostly dominated by magnetic field noise.

[47]Evaluating the residual micromotion from the uncertainty in the compensating fields fails in the radial plane since it only account for in-phase micromotion.

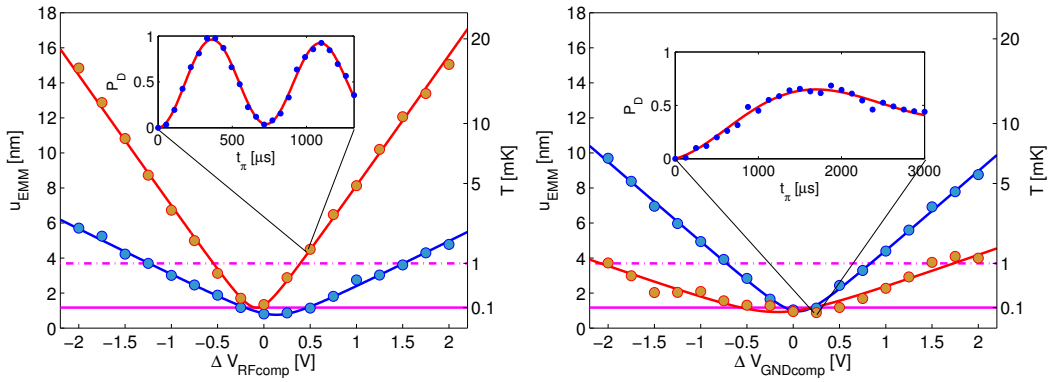

(a) (b)

Figure 3.18: **Radial EMM.** We scan the voltage on the compensation electrodes (left panel "RF", right panel "GND" - see Fig. 3.1a) and measure the EMM amplitude projected on two axes of the radial plane (x axis (blue) and y axis (red) as defined in Fig. 3.1). We extract the EMM amplitude from a Rabi flop scan on the carrier and sideband (inset show an example of such a scan) using $|\mathbf{u}_{j\,\mathrm{EMM}}| = 2\frac{\Omega_1}{\Omega_0}\frac{\lambda}{2\pi}\frac{1}{\cos(\theta_j)}$. Here, θ_j is the angle between our detection beam and the radial plane for axes x (20°) and y (45°). We fit the data to Eq. 3.31 (solid lines). Dashed and solid pink lines indicate 100 μK and 1 mK EMM energy respectively.

Plugging the numbers we get: $\gamma^{\mathrm{RF}} = 4.608\pm0.065\frac{\mathrm{mK}}{\mathrm{V}^2}$ and $\gamma^{\mathrm{GND}} = 1.800\pm0.045\frac{\mathrm{mK}}{\mathrm{V}^2}$. As seen from Eq. 3.32 these numbers depends on the specific trap parameters being used.

Axial compensation

As described in Sec. 2.4.3, we have a non-vanishing, constant, component of rf field along the axial trap axis even when dc fields are perfectly compensated. To compensate for this field we inject an oscillatory rf fields at the same magnitude and opposite phase (Sec. 3.3). We detect the axial EMM using a 674 nm laser beam aligned directly on the axial axis. This beam is sensitive only to axial micromotion. We scan the compensation field amplitude and its relative phase to the rf resonator (Fig. 3.19). Without micromotion compensation the ion oscillates with an amplitude of 4.25 nm which corresponds to kinetic energy of 1.3 mK. After compensating the micromotion we are left with an amplitude which its kinetic energy is smaller than 1 μK[48].

[48]This residual EMM is inferred from fit uncertainties.

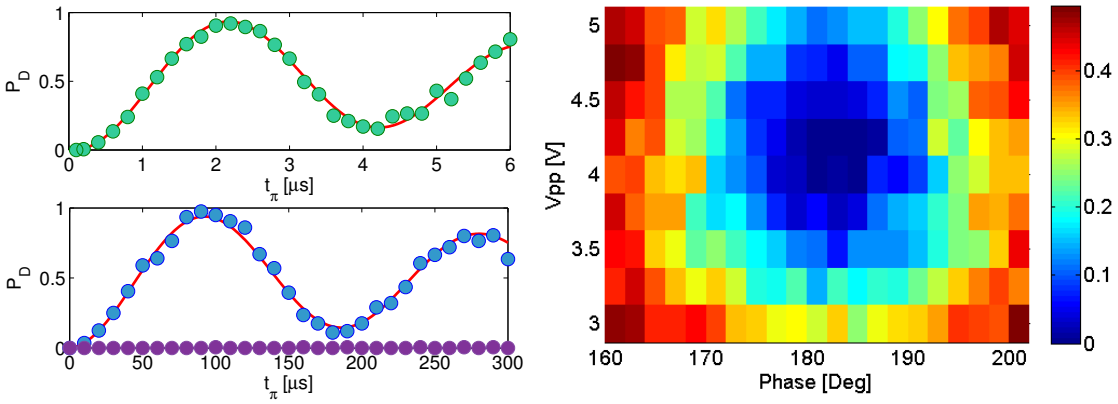

(a) (b)

Figure 3.19: **Axial EMM.** a) Top (green) Rabi flop on the carrier transition. Lower (blue/purple) Rabi flop on the first EMM sideband without/with axial micromotion compensation. b) 2D scan of the axial drive amplitude (y-axis) and phase (x-axis) while monitoring the EMM sideband amplitude (c-axis).

EMM stability

EMM is mainly induced by the dc and rf power supplies. Drifts in the dc power supplies voltages on both the DC and compensation electrodes will lead to drifts in the in-phase EMM compensation point. Drifts in the rf power on the RF electrodes will lead to drifts in the axial (and also quadrature) EMM compensation values.

UV light and atoms deposited from the trap ovens was shown to change significantly the EMM compensation values in other traps [110]. In our trap however, we didn't observe any effect from UV or ovens.

A log of the compensation voltages stability is shown in Fig. 3.20. For half an hour compensation rate we can maintain the in-phase EMM below 50 μK and the axial EMM below 1 μK. With a small improvement of our dc power supplies we believe we can reduce the EMM stability to below 10 μK for even slower compensation rate. This makes the uncompensated quadrature EMM in the radial plane (200 μK) the largest EMM source in our system.

3.6.4 Ion's electric heating

Cold ion sitting in a Paul trap heats up due to improper filtering of electric noise in the bandwidth of the trap mode frequencies or due to anomalous heating [111]. We cool the ion to its ground-state and measure the heating rate using motional sideband spectroscopy [60]. Assuming each of the modes is thermally distributed

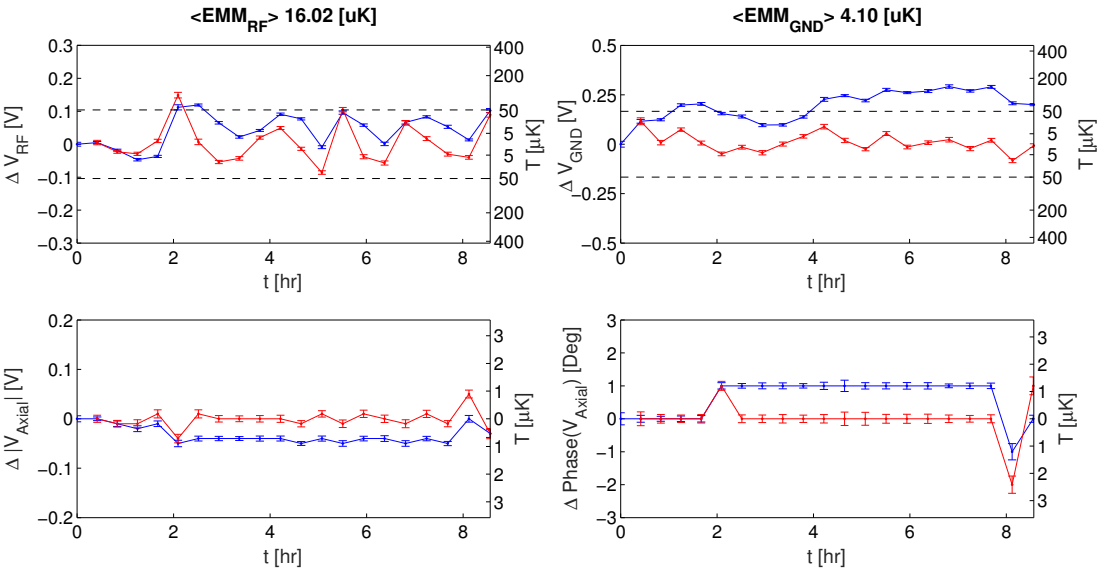

Figure 3.20: **EMM stability.** We measure the drift (blue lines) in the compensation values of the RF (upper left) and the GND (upper right) DC compensation electrodes and also for the amplitude (lower left) and the phase (lower right) of the axial compensation. Using the calibration method described in Fig. 3.18 we assign kinetic energy for the DC uncompensated values. For the axial compensation we use the measurement in Fig. 3.19a to calibrate compensation voltage to EMM amplitude. This stability measurement lasts for more than 8 hours during which the compensation values can drift significantly (upper right panel). However, since in each compensation measurement we re-calibrated the compensation values the actual compensation drift is the difference between two consecutive measurements (red lines). The drift doesn't exceed 50 μK for the DC compensation (upper panels) and 1 μK for the axial compensation (lower panels).

(with different temperatures in different modes), the mean occupation number is given by:

$$\bar{n}_i = \frac{R_i}{1 - R_i}. \tag{3.34}$$

Here, $R_i = \mathrm{P}_e^{\mathrm{rsb,i}}/\mathrm{P}_e^{\mathrm{bsb,i}}$ where $\mathrm{P}_e^{rsb,i}$ ($\mathrm{P}_e^{bsb,i}$) stands for the excited state population after on-resonant pulse (with arbitrary time) on the red (blue) sideband. The index, i, stands for the different motional modes.

From this measurement we extract the population after ground-state cooling: $\bar{\mathbf{n}}$=(0.1, 0.09, 0.01) and the heating rates: (0.96(9), 4.5(4), 0.52(1)) μK/ms for the axial and two radial modes respectively.

Chapter 4
Hybrid experimental system

On Jan. 2014 we set to combine the ion and atom apparatuses which where independent experiments up to that point. The atomic setup was constructed by Yoni Dallal and it described in detail in his PhD thesis. A SolidWorks design of the hybrid system is shown in Fig. 4.1.

We use six beams of 780 nm cooling light and a single beam of 780 nm repump to load ∼15 million ^{87}Rb atoms into a magneto-optical-trap (MOT) from a heated source of isotope enriched atoms[1]. We then decrease the beams power and increase the cooling laser detuning such that the atoms enter an intermediate state of higher density and lower temperature. The atoms shift to the position of zero magnetic field where a CO_2 laser beam (λ_{CO_2}=10 μm) is focused.

We load 200,000 atoms into the CO_2 dipole trap (Fig 4.2a). Then we evaporatively cool the atoms by ramping down the laser power. The atoms cool down in the CO_2 trap and subsequently loaded to the optical lattice trap.

We use two counter propagating YAG laser beams (λ_{YAG}=1 μm) to create a 1D optical lattice which is few μK deep. After switching off the CO_2 dipole trap we are left with 60,000 atoms in the optical lattice (Fig. 4.2b). We align the lattice trap with the center of the CO_2 dipole trap by minimizing the spatial oscillation of atoms upon their loading to the lattice. We use the 1D lattice trap as a conveyer-belt for atoms (escalator). We move the atoms by changing the relative frequency between the two lattice arms (see Sec. 4.2 for more details).

For ion atom-in-a-lattice experiments we move the atoms all the way down until they overlap with the ion (Fig. 4.2c)[2]. We align each lattice beam to overlap the ion by maximizing the ac-Stark shift induced by the 1064 nm beam on the 1033 nm repump transition (see Fig. 3.6b for ion's energy levels). We align the vertical ion-atom distance by looking on the increased atom loss due to ion-atom interactions.

For ion atom-in-a-crossed-dipole-trap experiments we transport the atoms with the lattice and bring the lattice to a stop 60 μm above the ion position. At this point we load the atoms into a crossed dipole trap composed of the bottom lattice beam and the additional horizontal YAG beam. We move the atoms to overlap the ion using a piezoelectric driven mirror on the horizontal beam line. We align

[1] Alvatec isotope enriched (98%) dispensers heated using a current of 3.7A.

[2] The distance between the CO_2 dipole trap and the ion trap is 25cm.

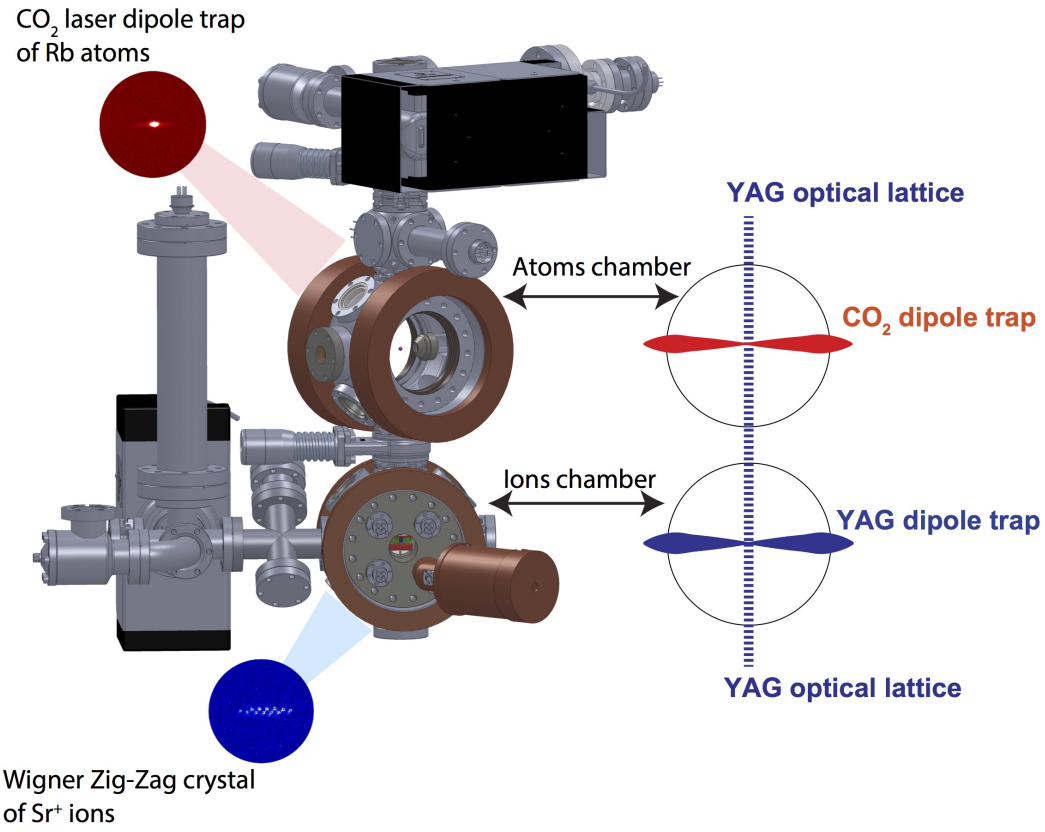

Figure 4.1: **SolidWorks design of the atom-ion apparatus.** Atoms are loaded into a CO_2 dipole trap in the upper chamber while ions are loaded in a Paul trap in the bottom chamber. For overlapping atoms and ions, the atoms are loaded into a vertical 1D optical lattice which is used to transport them to the ions chamber where they are overlapped with the ions.

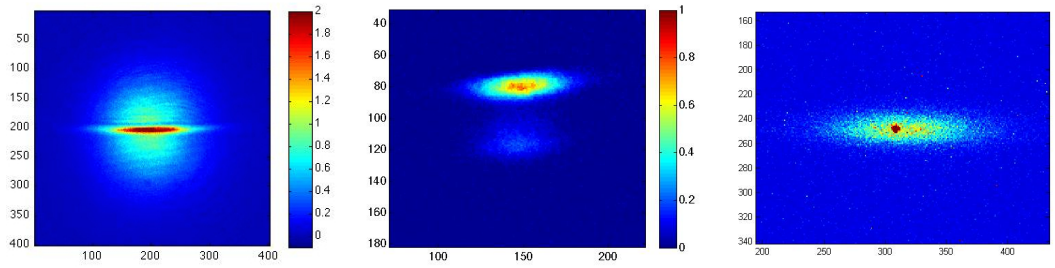

(a) (b) (c)

Figure 4.2: **Overlapping atoms and ion.** a) Loading the CO_2 trap from a MOT. Here, the waist and Rayleigh range of the CO_2 trap are larger then what is used in the experiment. b) Loading the escalator trap from the CO_2 trap. After shutting off the CO_2 laser the majority of atoms are trapped in the escalator trap (top cloud) while the hot atoms (bottom cloud) fall freely. c) Atoms trapped in a dipole trap overlapped with a single ion trapped in a Paul trap. In the first 100 μs of the 0.5 sec CCD exposure, we image the atoms using 780 nm light and then release them from the trap. 300 ms later, we image the ion with 422 nm light.

the horizontal YAG beam by maximizing the ac-Stark shift on the ion (see Sec. 4.3 for more details on the crossed dipole trap).

After interaction with the ion we release the atoms from the trap and monitor their profile after time-of-flight (TOF). We image the atoms by either fluorescence or absorption imaging using a bi-chromatic imaging system for both the atoms and the ions (Fig. 3.7). Few ms later, the atoms left the trap and we perform combined coherent and non-coherent dual spectroscopy.

4.1 Connecting both apparatuses

Both atoms and ions apparatuses require ultra-high-vacuum (UHV) for performing experiments. In the atoms chamber we collect atoms and evaporatively cool them to μK temperatures. Low background pressure is crucial for collecting more atoms at higher densities and colder temperatures. In the ion chamber the interaction between atoms and ions takes place. The bare atomic life time (without atom-ion interactions) is determined by the background gas pressure. We want this life time to be at least order of magnitude higher than the loss rate due to atom-ion interactions, even at low densities where three-body collisions are suppressed.

Prior to connecting the apparatuses, the pressure in the ion's chamber was below 10^{-11} Torr. In this pressure the trapped ion's life-time limited by chemical reactions is roughly 20 days. The atoms chamber maintained a pressure of 10^{-10}

Torr which gave life time of 10's seconds in the CO_2 dipole trap limited by elastic collisions of trapped atoms with background atoms.

The CO_2 beam enters, and exists, the atoms chamber through ZnSe windows which are transparent to 10.6 μm radiation. These windows are prone to leaks and also limit the bake-out temperature to 150°C. For that, we initially built the ion's chamber with a gate-valve[3] on top of it for keeping the UHV during the connection procedure. We vented the atoms chamber to atmosphere and installed new Rb[4] and Sr[5] ovens. A special translation stage was made to align both chambers during the connection process. During the first connection trial, due to mechanical stress, a vacuum bolt was torn inside the gate valve which kept the UHV in the ions chamber (see Fig 4.3). Surprisingly, the vacuum in the ions chamber was not broken while we drilled out the torn bolt[6]. In the second trial, after reducing mechanical stresses, we managed to connect the chambers.

To reach UHV we baked the system in a special oven-tent[7] built around the system on the optical table. We baked the system for three weeks (see Fig. 4.4), with the gate-valve between the chamber closed, after which the ions chamber gauge showed 10^{-11} Torr while the atoms chamber gauge showed only $5 \cdot 10^{-9}$ Torr. During the few weeks after bake-out, we noticed that the pressure in the atoms chamber is still decreasing. We decided not to bake-out again or check for leaks. The pressure half a year after bake-out was 10^{-10} Torr which is sufficient for our purposes. There is a thin tube[8], just underneath the gate-valve, which keeps the differential pressure between the chambers even when the gate-valve is open.

4.2 Atoms transport to the ion's chamber

To move the atoms to the ion's chamber and trap them we use a 40W YAG laser[9]. We divide the laser beam to three distinct lines. We use two lines to form a 1D optical lattice for moving the atoms from the top to the bottom chamber. The third line creates a dipole trap which overlaps the center of the ion trap. We pass each beam line through an AOM[10] which is used to switch the beam on and off

[3]VAT mini UHV gate valve #01032-UE01.

[4]Alvasource enriched $^{87}Rb^{+}$ source AS-2-Rb87-25-S.

[5]Home-made ovens filled with 99.99% purified Sr from Sigma-Aldrich #441899.

[6]There was an increase in pressure up to 10^{-9} Torr probably due to outgassing from the viton seal. The pressure returned to normal after 50°C bake-out.

[7]The bake-out tent was made by Hemi-Heating and was improved by Rostyslav Baron and Asif Sinay.

[8]We drilled a hole in a blank gasket to secure a 6 cm long bolt with a nut. The bolt is drilled in its center.

[9]Mephisto MOPA 40W from Coherent.

[10]Crystal Tech. AOM #3080-197.

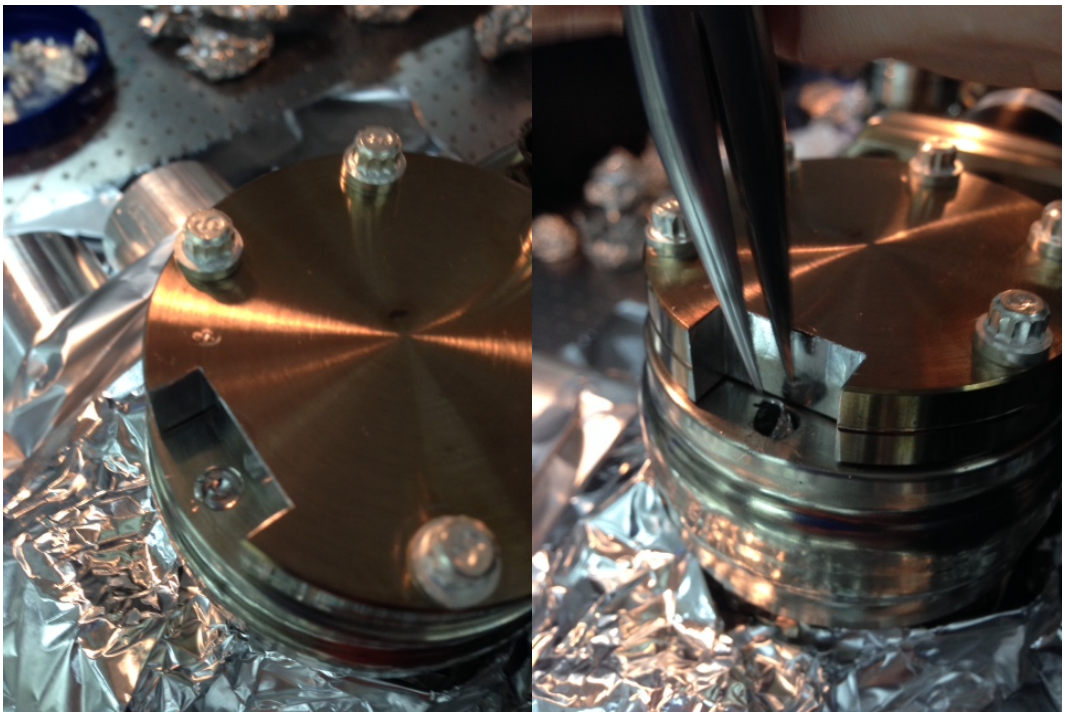

(a) (b)

Figure 4.3: **Removing torn bolt from a gate vale under 14 order of magnitude pressure difference.** Pictures of the torn bolt and the protecting cap made for the extraction of the bolt from the UHV gate valve. This gate valve didn't leak even when we applied excessive mechanical stress on it. We observed only small outgassing (probably from the viton ring) mainly when we banged it with a hammer. This small outgassing was pumped during the early stages of the bake-out.

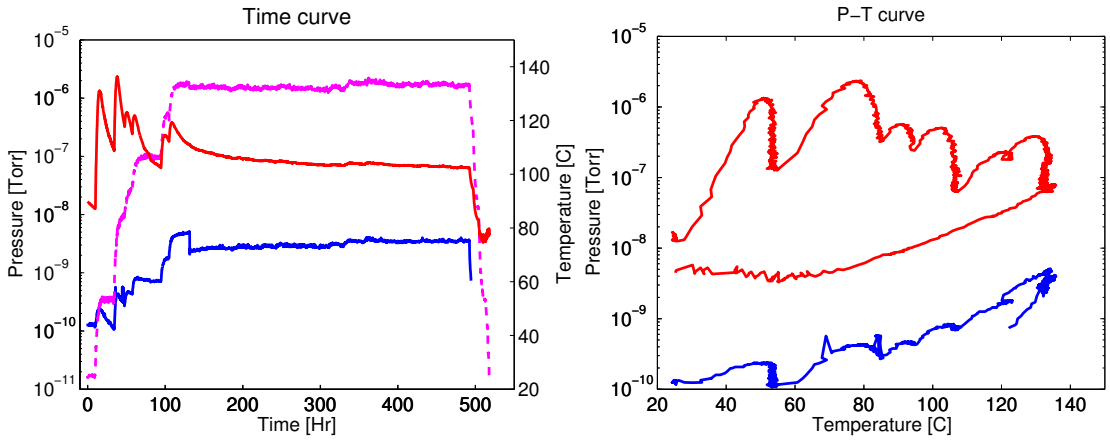

(a) (b)

Figure 4.4: **Full system bake-out.** a) Log of the pressure in the atoms chamber (red) and the ions chamber (blue) for the hybrid system final bake-out. The bake-out lasted for three weeks due to the low bake-out temperature (magenta) of 150°C. The ion's gauge signal dropped to zero (below 10^{-10} Torr) in the cooling process. b) Plot of the pressure vs. temperature for the same bake-out. The atoms curve (red) shows severe out-gassing typical for systems exposed to atmosphere conditions. However, the cooling curve indicates a leak (non linear P-T cooling curve) and the pressure only dropped by factor of two during the bake-out. This seemingly disastrous indication proved wrong when the pressure continued to drop by factor 15 during the next few months.

and also to control the frequency and power of the beam. We couple the lines into special high power optical fibers[11] which are used to decouple the beams alignment on the ions and the atoms from the control section. A sketch of the distribution and control system is depict in Fig 4.5 and explained in more detail in figure caption.

We create the 1D optical lattice by coupling the light from one fiber to the second fiber to create a standing wave such that both beams overlaps each other and also the position of the atoms and the ion. We designed the beams waists (250 μm) to overlap the center of the ion's trap. This waist size ensures that only 1% of the beams power[12] is reflected from the trap electrodes (750 μm wide)[13]. We first align the bottom escalator beam on both the ion and the atoms using a 422 nm alignment beam. The blue beam scatters light from the ion and ionizes the atoms. We overlap the bottom escalator beam with the 422 nm beam to get initial rough alignment of the escalator. To further improve the alignment we couple 1092 nm beam into the escalator line fiber. With this beam we align the YAG precisely on the ions (1092 nm is the ion rempuper). Iteratively, we monitor the oscillations of the atoms after loading into the lattice for further improvement of the lattice-CO_2 alignment (Fig. 4.2b). For final refinement of the escalator beams alignment, we measure the ac-Stark shift induced by each escalator beam on the $D_{5/2}$ level through off resonance coupling to the $P_{3/2}$ (1033 nm) dipole transition using our narrow laser and the 674 nm transition. This alignment guarantees that both YAG beams, and consequently the atoms, overlap the ion position. Assuming that both beams polarization is the same[14], it is also a measurement of the beams intensity imbalance inside the chamber. A sketch of the escalator line around the apparatus is depicted in Fig. 4.6 and explained in detail in the figure caption.

By changing relative optical frequency of the two arms of the escalator, the standing wave starts to move at a velocity:

$$v\left(\mathrm{t}\right)=\frac{\lambda}{2}\Delta f\left(\mathrm{t}\right). \tag{4.1}$$

Here, $\lambda = 1.064\mu$m is the laser wavelength and $\Delta f\left(\mathrm{t}\right)$ is the instantaneous frequency difference between the beams[15]. Integrating over Eq. 4.1 gives us the distance the atoms traveled. We control the frequency on both of escalator arms

[11] Schäfter&Kirchhoff PM fibers with end-caps for high power #PMC-E-980-9.9-NA008-3-APC.EC-250-P.

[12] Each beam is roughly 1.5 W on the ion.

[13] The actual beam waists are $\sim$220 μm for bigger error margin.

[14] We can use the ion to tune both beams to the same polarization if we set the YAG polarization such that the $D_{5/2}(m=\pm 5/2)$ is not shifted.

[15] Due to the double-pass AOM configuration there is a factor of two between the AOMs frequency difference and the lattice frequency.

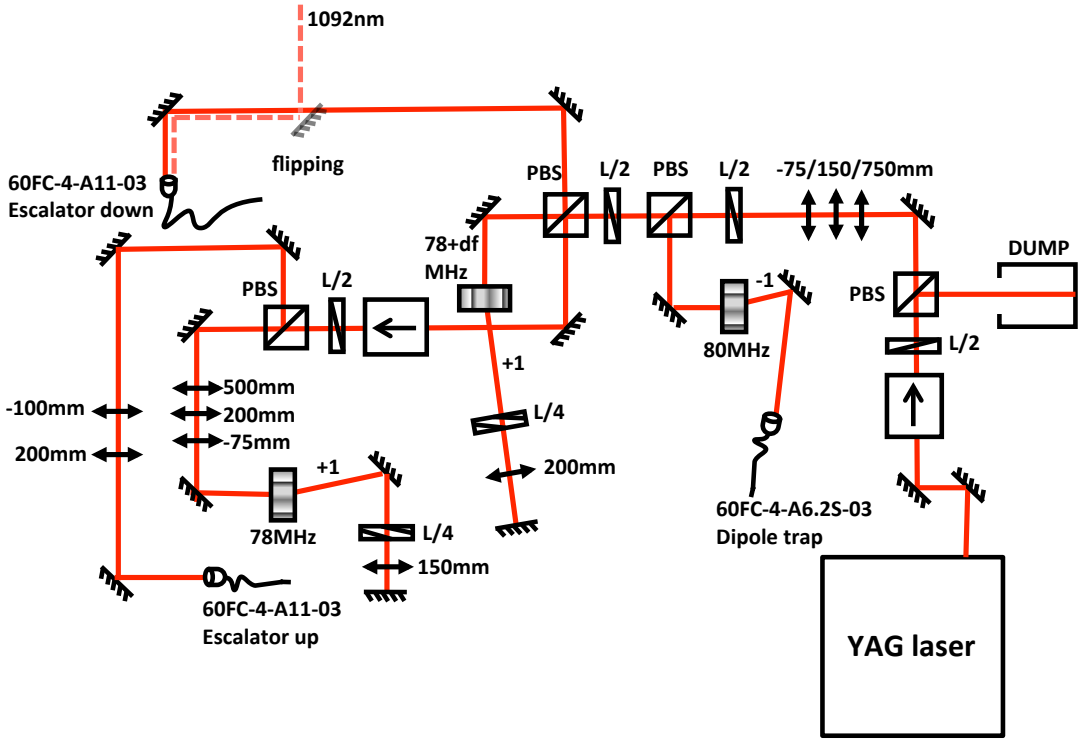

Figure 4.5: **Sketch of the YAG laser control and distributing system.** From the laser head, we pass the beam through an isolator and then a polarization beam splitter (PBS) and half wave-plate (HWP) to control the total power distributed to the beam lines. The second HWP and PBS divides the power between the dipole line and the escalator lines. The last HWP and PBS divide the power between the two escalator lines. The dipole line pass through the AOM's -1^{st} order in a single-pass configuration. The escalator lines pass through the AOMs $+1^{st}$ order in a double-pass configuration. This way the escalator lines and the dipole line are separated by 240 MHz which eliminates interference effects. Using AOM in double-pass configuration in the escalator lines allows us to sweep the AOM frequency without changing the power coupled to the fibers. We use optical isolators to stop reflections from reaching the laser head, to decouple both arms of the escalator and to provide an exit dump to the escalator beams. We use three different telescopes to control the beam size and waist location on the AOMs and fibers. This way our coupling efficiency is around 50% for the entire line (double-pass and fiber coupling).

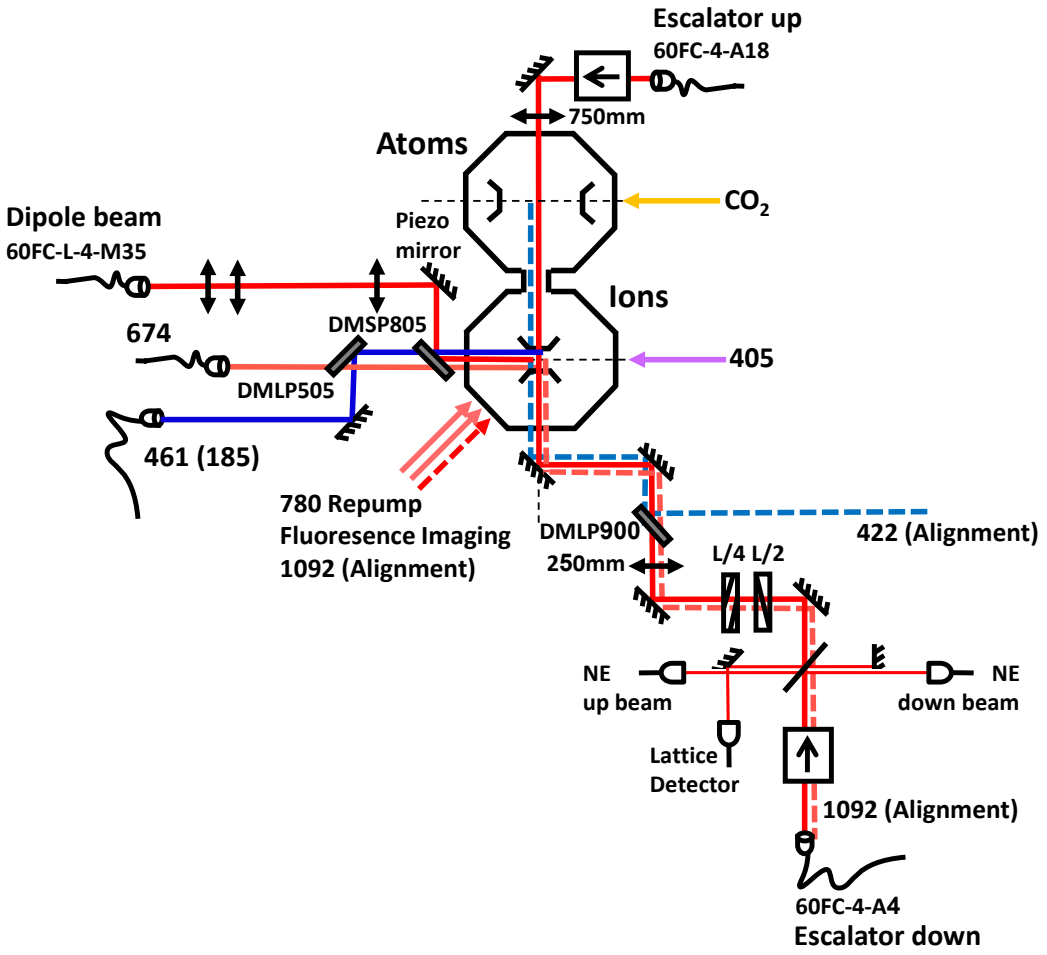

Figure 4.6: **Sketch of the atoms escalator and dipole lines.** We pass both escalator lines through optical isolators to avoid beam circulation and protect the fibers from the increased lattice intensity. We create a Mach-Zender interferometer using a reflection from the facet of a window oriented at 45° angle to the beam line. We use the interferometer to monitor the lattice alignment, lock the lattice position and count the distance the atoms traveled. We use the reflection from the second facet of the window to lock the beams power using a noise-eating (NE) servo. We use a quarter and half wave-plates to correct for birefringence effects of the vacuum chamber windows. The bottom beam passes through the vacuum chamber and it is coupled to the upper fiber. A 422 nm beam is coupled by a dichroic mirror for rough alignment on the atoms and ions. A 1092 nm beam which is coupled through the down escalator fiber is used for fine alignment on the ions. A horizontal YAG beam together with the escalator down beam creates a cross dipole trap in the center of the ion trap. We can change the position of the dipole trap with respect to the ion using a piezoelectric driven mirror.

using Tektronix AFG3252C two-channel function generator which drives the AOMs on the beam lines. The function generator creates trapezoidal sweeps of the frequency (ramp up, delay, ramp down). Changing the frequency in a single beam of the escalator, we can accelerate the atoms and then decelerate them to full stop after they traveled the required distance. Using both of the escalator arms, we can transport the atoms to any position and bring them back to their original position. Such two way transport is shown in Fig. 4.7. Typically, we use a single-way transport of 0.3 sec. The efficiency is almost 100% when the ion Paul trap is turned off.

The main source of atoms loss during transport is the electric fields generated by the ion trap. Our trap is designed to reach the Lamb-Dicke regime which requires high electric fields to generate high trapping frequencies (up to 1.8 MHz). For comparison, other atom-ion experiments works at much lower trap frequencies (typically 200 kHz). When the atoms reach the ion trap they experience high electric field gradient in the entrance to the trapping region. This electric field gradient modifies the atoms trapping potential which leads to atom loss. With the current escalator beams power this limits the maximal ion trap radial frequency to around 1.5 MHz.

4.3 Overlapping atoms and ions

With the escalator we can transport the atoms all the way to overlap with the ion. Aligning the traveling distance, which overlaps the atoms with the ion, using the imaging system (see Fig. 4.2c) is highly in-accurate[16]. Instead, we look on the loss rate of atoms from the trap due to atom-ion elastic collisions, the best overlap maximize the loss rate.

The density profile in the optical lattice is highly inhomogeneous along the lattice axis which makes experimental analysis complicated. For that, we usually transport the atoms with the escalator up to roughly 60 μm above the ion. Then we turn on a horizontal YAG beam[17] and turn off the upper arm of the escalator[18]. This way we create a cross dipole trap with a nice Gaussian density distribution. To overlap the atoms with the ion we use a piezoelectric driven mirror to move the atoms down in 5 ms[19]. We achieve a perfect overlap by maximizing the ac-Stark

[16]The imaging system is only sensitive in two axes, it has inherent chromatic shifts due to the different wavelengths of the atom and ion fluorescence and moreover, the imaging beams moves the atoms in fluorescence imaging due to radiation pressure.

[17]Roughly, 1.5 W power and $\sim$30 μm waist on the ion.

[18]We also increase the power of the bottom escalator beam to match the ac-Stark shift of two beams.

[19]We use short transport time to reduce the additional interaction within the time of transport and also to reduce anomalous heating time.

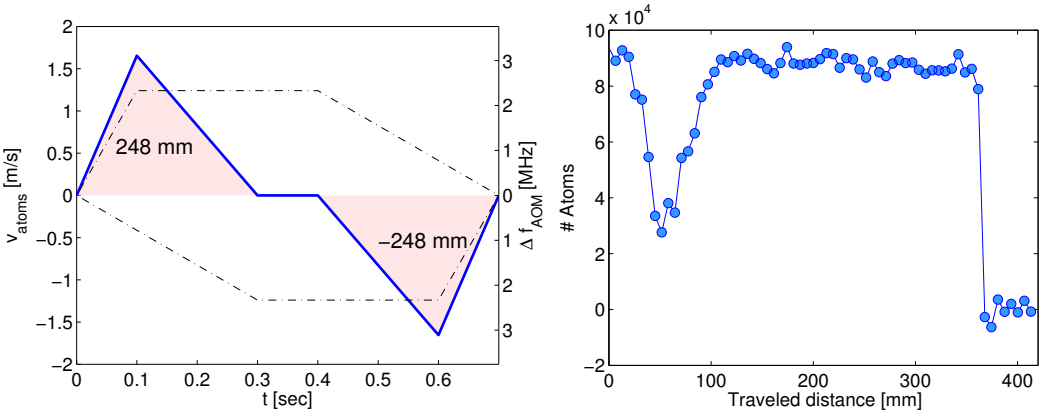

(a) (b)

Figure 4.7: **Atoms transport.** a) In blue we plot the instantaneous velocity of the atoms during transport. The atoms accelerate to their maximum velocity of ∼1.6 m/sec and immediately decelerate to rest. During this period the atoms traveled ∼248 mm (shaded red area) which is the approximate distance between the top chamber atoms trap and the ion trap. After a variable hold time the atoms are accelerated upwards back to their original position. In dashed-doted lines we show the AOM frequency change of the two escalator arms (note that we increase the frequency in both arms) during this transport. b) Number of atoms after a round trip with increasing distance. Here, the ion Paul trap (at ∼248 mm) is turned off. Just underneath the atoms initial position lies a region of increased atoms loss. We avoid atom loss by minimizing the time spent in this region.

shift of the crossed dipole beams on the ion.

Atom-ion interaction starts before the end of the dipole transport stage due to the finite size of the atomic cloud. We take this into account by calculating an additional effective interaction time. We assume the atomic cloud has a Gaussian profile:

$$n(x,y,z) = n_0 e^{-x^2/2\sigma_x^2 - y^2/2\sigma_y^2 - z^2/2\sigma_z^2}. \tag{4.2}$$

Here, n_0 is the peak atomic density, $\sigma_x = \sigma_y \approx 3.7$ μm and $\sigma_z \approx 70$ μm were measured using absorption imaging (see Sec. 4.3.1 below). During the transport, the atomic density on the ion's position is given by: $n(t) = n_0 e^{-(v_y t)^2/2\sigma_y^2}$. Here, v_y=53 μm/5 ms is the calculated (average) ion's velocity during transport. We assume the ion is positioned in (0,0,0) and define t=0 as the end of the transport time. By integrating $n(t)$ over the transport time we extract an effective interaction time, τ:

$$\tau = \frac{1}{\tilde{n}_0}\int_{-\infty}^{0} n(t)dt = \frac{n_0}{\tilde{n}_0}\sqrt{\frac{\pi}{2}}\frac{\sigma_y}{v_y}. \tag{4.3}$$

Here, $\tilde{n}_0 = 0.86 \cdot n_0$ is the effective density due to atomic cloud oscillation which we will address shortly. We can take the initial integration time to $-\infty$ since there is no overlap between the atoms and ion in the beginning of the transport (t=-5 ms). Plugging the numbers we get τ=0.503(43) ms.

As pointed out earlier, due to the short transport time the atoms oscillate for 10's ms with an amplitude of roughly y_0=3 μm (see Fig. 4.8). We take into account this oscillations by calculating the effective density, $\tilde{n}_0$, which is the density in the ion's position averaged over one period of oscillation ($f_{osc} \approx 1$ kHz):

$$\tilde{n}_0 = \frac{\omega}{2\pi}\int_0^{2\pi/\omega} n_0 e^{-(y_0\cos(\omega t))^2/2\sigma_y^2} dt = n_0 e^{-y_0^2/4\sigma_y^2} \mathrm{I}_0(y_0^2/4\sigma_y^2), \tag{4.4}$$

Which yields $\tilde{n}_0/n_0$=0.86(2) for our experimental parameters (I_0(z) is the first modified Bessel function of the first kind).

4.3.1 Atomic density estimation

All above calculations depend on the knowledge of the atomic density profile. We use time-of-flight (TOF) absorption imaging to extract the profile parameters (see Eq. 4.3). In TOF the cloud size expands as: $\sigma_i^2 = \sigma_{0,i}^2 + \sigma_{v,i}^2 \cdot t^2$ where σ_0 is the initial width of the atomic cloud and $\sigma_v = \sqrt{\mathrm{k_B T}/m}$ is the cloud "thermal" size. The proper time, t, is the TOF time plus half the CCD exposure time[20]. We measure the atomic cloud profile widths, σ_y and σ_z, for four TOF times (200,400,600 and

[20]We verified this by a numerical simulation.

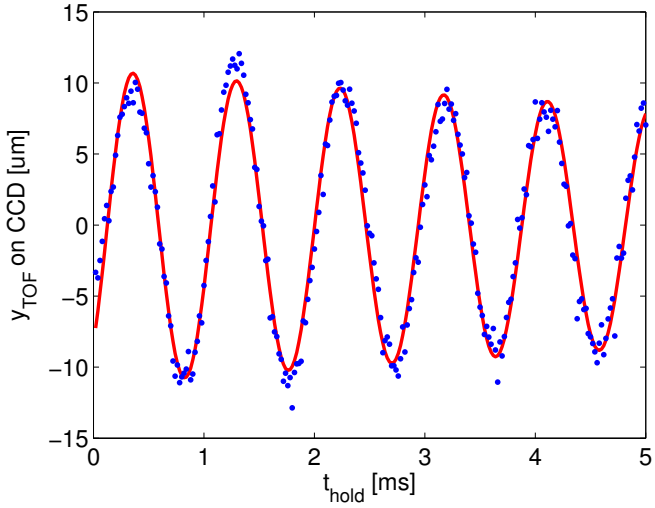

Figure 4.8: **Atoms oscillation after dipole transport.** We record the atoms' position on the CCD (blue dots) after time-of-flight (TOF) of t_{TOF}=0.55 ms (TOF + exposure time/2). We fit the data to a function: $y_{TOF}(t)=(y(t)+\dot{y}(t)\cdot t_{TOF})e^{-t/\tau}$ which takes into account the translation of the atomic cloud during TOF. From $y(t)=y_0\cos(\omega t+\phi)$ we extract the atomic oscillation amplitude, y_0=2.898(68) μm, and frequency, $\omega/2\pi$=1.066(1) kHz. The 1/e time constant of the oscillations decay is 18(3) ms.

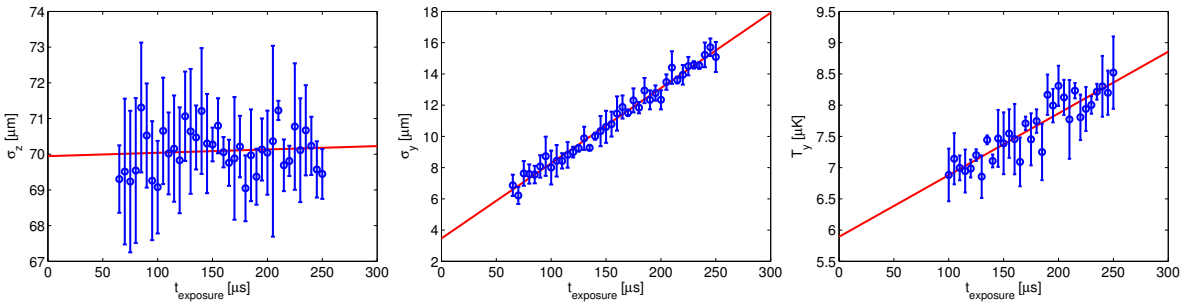

(a) (b) (c)

Figure 4.9: **Extrapolation of TOF parameters to zero exposure time.** a) $\sigma_{0,z}$=70(1) μm. b) $\sigma_{0,y}$=3.47(18) μm. c) T_y=5.89(16) μK.

800 μs) from which we extract the temperature[21], T_y, and the initial widths, $\sigma_{0,y}$ and $\sigma_{0,z}$. Even though we included the exposure time in the TOF analysis, we still see mechanical effect due to the absorption beams. We repeat the above experiment for exposure times from ∼50 μs to 250 μs and extrapolate for zero exposure time. We present the results in Fig. 4.9.

We can now check our profile results for consistency. First, the ratio of the radial to axial widths should follow the ratio of the axial to radial atomic trap frequencies: $\sigma_y/\sigma_z = \omega_z/\omega_y \approx 1/20$. We measured independently the radial frequency (Fig. 4.8) to be 1 kHz and the axial frequency to be 50 Hz with good agreement with the atomic profile ratio. We can also compare the atomic density using two different methods. First, using the atomic profile widths:

$$n = \frac{N}{(2\pi)^{3/2}} \frac{1}{\sigma_{0,x}\sigma_{0,y}\sigma_{0,z}}. \tag{4.5}$$

Here, we need to assume that the profile is symmetric in the radial direction: $\sigma_{0,x} = \sigma_{0,y}$. The resulting density is $1.51(11)\cdot10^{12}$ cm^{-3} for 20,000 atoms in the trap. Second, using the atomic temperature:

$$n = N \left(\frac{m\bar{w}^2}{2\pi \mathrm{k_B T}} \right)^{3/2}. \tag{4.6}$$

Here, $\bar{\omega} = (\omega_x\omega_y\omega_z)^{1/3}$ where we assume that $\omega_x = \omega_y$ and also that the atoms are in thermal state in which T=T_y. The resulting density is $1.17(5)\cdot10^{12}$ cm^{-3} for 20,000 atoms. We take the average of these two measurement and conclude that the atomic density is $1.35(2)\cdot10^{12}$ cm^{-3} for 20,000 atoms which yields an atomic size of 70(1) μm axially and 3.66(27) μm radially.

[21]The cloud initial size is too big in the z-axis to extract the temperature in this axis.

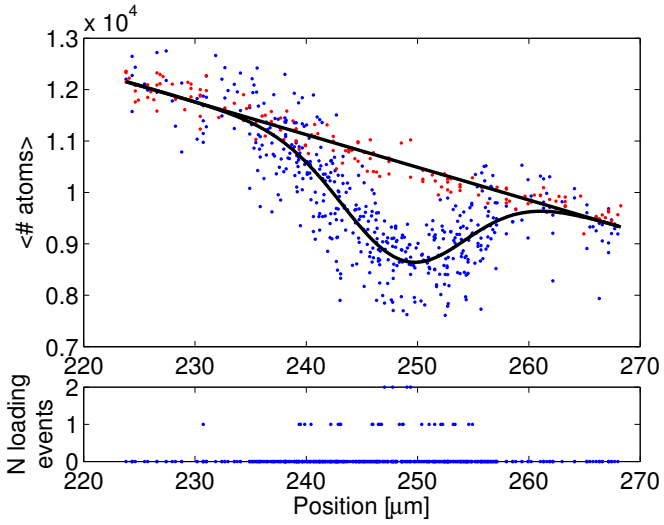

Figure 4.10: **Atomic profile via atom-ion interactions.** Using the piezoelectric driven mirror we move the atoms to different relative positions with respect to the ion. We interact for 1.7 sec after which we detect the number of atoms (upper plot - blue dots). We also count the number of ion loss events (lower plot - blue dots). We perform the same experiment without an ion (red dots). Black line is a fit for a Gaussian distribution with linear offset extracted from the background measurement. This linear offset is due to increased loss for longer transport distances.

The atomic profile is best measured using absorption imaging. In Fig. 4.10 we show an alternative method which utilize the atom-ion elastic and in-elastic interactions for measuring the atomic profile. This method is based on our ability to accurately position the dipole trap center with respect to the ion. The resulting atomic profile width of σ=5.5(2) μm overestimates the real width extracted from absorption imaging, possibly due to the power-law tail energy distribution of the ion.

4.4 Experimental aspects

One of the main challenges in our experiment is the long experimental data acquisition which can take days. As in any other cold atoms experiment, due to atoms preparation (i.e. MOT loading, evaporation etc.), each experimental sequence takes at least few seconds. However, in contrast to other cold atoms experiments where in each experimental shot the signal is averaged over many atoms, in our experiment we typically acquire only one bit of information from our single ion. This

makes data acquisition lengthy (on the orders of hours/days) and makes experimental control pivotal. During a day of data acquisition, we need to monitor the experimental parameters for drifts. We perform automatic, hourly calibrations of excess-micromotion compensation, ground-state cooling calibration, ion-atom overlap alignment and laser tuning.

During our experiment, due to in-elastic processes (Sec. 2.2), the Sr^+ ion is lost from the trap (see Sec. 4.4.1 for analysis of the in-elastic process product) and we need to load a new ion. The rate of these events depends on the type of experiment, mainly the atom-ion interaction time. In my type of experiments the interaction times are usually short and we lose an ion every few hours. Our approach for automatic loading a new ion is very simple, we just turn on the ovens and ionization lasers until a new ion appears. We decided to keep the Sr ovens off during the experiment to reduce the effect of collisions with the neutral hot Sr vapor and also to eliminate the Zeeman shift created by the current running in the ovens wires near the ion's trap. We run the ovens with relatively low current (4.7A) mainly for safety reasons[22]. We pay by a relatively long ion loading time of few minutes. Recently, we learned to suppress charge-exchange events even more by aligning the atoms spin polarization with the ion (Sec. 6). This will even reduce more the need of more elaborate loading schemes such as loading from a cold source [112].

Even though in-elastic processes are suppressed, we can still load unwanted Rb^+ ions into the Paul trap by accidently ionizing the atomic cloud. In-situ imaging, i.e. 1064 nm + 780 nm light, of the atoms inside the Paul trap will generate many Rb^+ ions. This is also the case for 1064 nm + 461 nm light[23]. A more sever experimental problem is the combination of 1064 nm and 422 nm photons. We noticed that for this combination we get Rb^+ ions even when the atoms cloud is not present in the ion trap. This is probably due to μK cold atoms which are guided by the lattice beams into the ion trap. For that, we Doppler cool the ion with short, sub-ms, pulses every few hundred ms during the atoms transport.

In our experiment we cool the ion to the ground-state prior to overlapping it with the atoms. Due to anomalous heating (Sec. 3.6.4), we need to perform the ground-state cooling as close as possible before the interaction begins. In atoms-in-a-crossed-dipole-trap experiments this is easily done by tuning the laser frequencies according to the bottom escalator YAG beam ac-Stark shift[24]. In escalator experiments however, the ac-stark shift oscillates due to the spatial intensity profile of the lattice. We found that for relative frequencies above 500 kHz in the lattice arms the oscillations are fast enough to give a sharp line which we can perform

[22] In the case that the ovens will run indefinitely due to software problem.

[23] This was discovered accidently in the experiment, there is no apparent reason to shine 461 nm light not in the loading sequence.

[24] The horizontal beam is far enough not to induce any Stark shift.

ground-state cooling on. The efficiency of the cooling deteriorates as the atoms decelerate to a stop.

4.4.1 Mass spectroscopy

In our experiment, in-elastic processes can result in either Rb^+ ion or $(RbSr)^+$ molecule (see Sec. 2.2). One method for determining the product specie is mass spectroscopy. By driving an electric field in the trap's resonance frequency of the expected element followed by fluorescence imaging we can determine whether our initial guess was correct[25]. This single shot spectroscopy is done in the dark which is important for revealing loosely bound molecules. A more relaxed method (Fig. 4.11) is to continuously scan the drive frequency while fluorescing from the ion. When hitting resonance, the fluorescence decreases and the spatial size on the CCD increases. Since the products of the in-elastic processes are all dark, we use a two ion's crystal where the second ion is used to detect the trap frequency. In the following we show how to calculate the trap frequency for two ion's crystals with different elements.

The potential energy near the ion's trap center is well approximated by an harmonic potential. In the axial direction the potential is given by $\mathrm{V} = \frac{1}{2}\mathrm{m}\omega_z^2 z^2$. Here, z is the displacement of the ion from the trap center and $\omega_z \propto \frac{1}{\sqrt{\mathrm{m}}}$ is the trap axial frequency which is inversely proportional to the square-root of the ion's mass, m.

For more than one ion, the Coulomb repulsion displaces the ions from the center of the trap such that the potential energy in the axial direction[26] is given by,

$$\mathrm{V} = \sum_{i=1}^{\mathrm{N}} \frac{1}{2}\mathrm{m}_i\omega_{z,i}^2 z_i^2 + \sum_{i\neq j}^{\mathrm{N}} \frac{e^2}{8\pi\varepsilon_0}\frac{1}{|z_i - z_j|^2}. \tag{4.7}$$

Here, the i-index indicates the different ions in the lattice chain, e is the electron charge and ε_0 is the vacuum permittivity. We can find the ions' equilibrium positions by solving $\frac{\partial \mathrm{V}}{\partial z_i} = 0$. Since $\mathrm{m}_i\omega_{z,i}^2 = \text{const}\ \forall i$ ($\omega_{z,i} \propto \frac{1}{\sqrt{\mathrm{m}_i}}$) the equilibrium positions do not depend on the masses of the species trapped, only on their charge. The equilibrium positions can be found analytically for two and three ions and numerically for more than three ions [61].

The Lagrangian of the ions in the crystal is given by:

$$\mathcal{L} = \frac{1}{2}\sum_{i=1}^{\mathrm{N}} \mathrm{m}_i\dot{q}_i^2 - \frac{1}{2}\sum_{i,j=1}^{\mathrm{N}} q_i q_j \left(\frac{\partial^2 \mathrm{V}}{\partial z_i \partial z_j}\right)_0. \tag{4.8}$$

[25] This can be done, e.g, by looking on the fluorescence re-cooling curve.

[26] Usually, the trap radial frequencies are much higher than the axial frequency such that the ions form a crystal along the axial direction

2^{nd} ion specie	m_2	$\Omega_-/\omega_{z,1}$
$^{88}Sr^+$	87.91	1
$^{87}Rb^+$	86.91	1.003
$(RbSr)^+$	174.81	0.798

Table 4.1: Calculated axial center-of-mass mode frequency ratio between two identical $^{88}Sr^+$ ions and a chain composed of one $^{88}Sr^+$ ion and an additional in-elastic product ion.

Here, $q_i(t) = z_i(t) - z_i^0$ are the small displacements around the equilibrium positions of the ions. The eigen frequencies (Ω) of the system are given by solving $\left|\left(\frac{\partial^2 V}{\partial z_i \partial z_j}\right)_0 - \Omega^2 m_{ii}\right| = 0$. In the case of two ions the eigen frequencies are given by:

$$\begin{aligned}\Omega_\pm &= \sqrt{\left(\omega_{z,1}^2 + \omega_{z,2}^2\right) \pm \sqrt{\omega_{z,1}^4 + \omega_{z,2}^4 - \omega_{z,1}^2\omega_{z,2}^2}} \\ &= \omega_{z,1}\sqrt{1 + \frac{m_1}{m_2} \pm \sqrt{1 + \frac{m_1^2}{m_2^2} - \frac{m_1}{m_2}}}\end{aligned} \tag{4.9}$$

Where $\omega_{z,1}$ is the axial frequency of single ion of mass m_1. For identical ions Eq. 4.9 reduce to the well known result of $\Omega = \omega_{z,1}, \sqrt{3}\omega_{z,1}$. A change of one ion in a two ion crystal from $^{88}Sr^+$ to $^{87}Rb^+$ will induce a 0.3% axial frequency shift (see Table 4.1), which as seen in Fig. 4.11b can be easily detected.

4.5 What to do after power shut down?

This is probably the most important part of this thesis. Here, I would like to list all the lab's quirks which can be extremely painful to detect without prior knowledge. I'll start by specifying all the things to do after a lab disaster such as power shut down[27]:

- Check that the ion pumps are working.
- Check the temperature in the lab[28], if the temperature is not stable there is no point of locking the lasers. First, find out why is the temperature drifting. Make sure that the temperature goes back to its original value[29].

[27]Note that from the time this list was written, there might been a lab upgrade which made some of the instructions obsolete.

[28]HOBO® temperature, relative humidity and light data logger.

[29]The HOBO temperature reading should be 24±0.2°C.

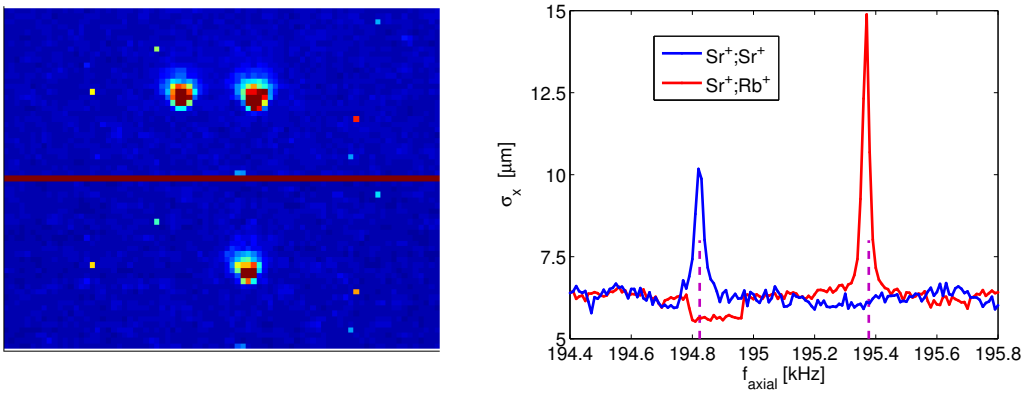

(a) (b)

Figure 4.11: **Charge exchange and mass spectroscopy.** a) CCD image of the fluorescence of two $^{88}Sr^{+}$ ions in the trap (top) before overlapping them with ^{87}Rb atoms. During the interaction, one of the ions becomes dark (bottom) while the bright ion remains in its relative position (if one ion was lost form the trap then the remaining ion will change its position to the center of the trap). b) Axial center-of-mass mode spectroscopy. We measure the ion's spatial size on the CCD (the image is over saturated) while constantly driving an RF field on the B_{rf} electrode (see Fig. 3.3). The axial frequency for two bright ions (blue) is 194.82 kHz while for one dark and one bright ion (red) is 195.36 kHz. The frequency ratio indicates that the dark ion has same mass of ^{87}Rb (magenta lines).

- Go over all diode controllers and turn them on. Make sure they are at their last settings [30]. If the temperature control went off, wait few minutes before locking the laser.

- Go over the frequency sources. The Keithley's and the Tektronix function generators have a tendency to reset after power shut down. Even though they are automatically set by the computer to their original values, you should check that the output power is on and also that the power units are set to dBm (except for the EMM resonator which should be set to Vpp). check the DDS (IONIT) of the 1033 nm AOM[31], after power shut down it might stop working, restart it[32]. Check that the EMM and rf resonator are phased locked.

- Go over all dc power supplies, some of the amplifier voltage sources might turn off, turn them on. Look on the EMM compensation power supplies and check if they are responding to voltage change in the Dictator GUI, if not, restart them.

- If the computer crashed, restart Labview and load the most updated target[33], slave[34] and host[35]. Note that some parameters were not saved and got lost during the crash. If the Labview GUI seems to not respond, click the "release freeze" (green) buttons to release it. If the 780 nm offset locking doesn't lock click the update ADF4113 button in the, check that the period setpoint value is correctly set[36].

After that seemingly all the lab instruments were turned on and set to their correct values, it is time to trap an ion. Here is a list of do's and don'ts when you just can't trap an ion:

- Don't be tempted to touch mirrors or move the CCD. Usually the problem is much more simple and doesn't require any alignments.

- First, make sure that all lasers are locked, simultaneously. The relevant

[30] The current and temperature values should match the sticker value on the controller.

[31] The best way is to look on the power going to the ion's chamber.

[32] The best way is to kill the Dictator GUI, turn off and on the power-supply and then load again the Dictator GUI.

[33] Last version: `BLENDER_FPGA_v14_b_AtomIonCombined.vi`

[34] Last version: `BLENDER_FPGA_Slave_v14_c_AtomIonCombined.vi`

[35] Last version: `BLENDER_HOST_v14_c_AtomIonCombined.vi`

[36] Usually it should be 131. If it is not set use the PIGEON programming line: `prog.GenAO('PeriodSP',131)` to set it.

lasers are the 461 nm for photoionization and the 422 nm cooling[37] and 1092 nm repump.

- Check positively (with an IR card and a piece of paper or alternatively with a power detector) that all lasers are actually reaching the ion's chamber. On top of the above mentioned lasers make sure the 405 nm is on.

- Check the rf source[38] and the dc voltages. If you check the actual voltage on the electrodes remember that there is a resistor which acts as a voltage divider. Check that the EMM dc voltages make sense. Look on the power supply itself, sometimes it gets stuck on a wrong default value. If you are not sure that the EMM resonator phase is correct, reduce the EMM resonator voltage to 0.1 V and increase the rf power.

- Check that the ovens are on. At 4.7 A there is no problem to keep them on for an hour. Don't forget to turn them off eventually.

- Check beam alignments. The 422 nm and 1092 nm lasers should pass through an iris which is located at the approximated position of the ion outside the chamber[39]. Check that the 405 nm beam is coupled back to the 461 nm fiber.

- The auto-loading script automatically clears the trap every two minutes. Try to load manually a big ion cloud.

- Change the CCD zoom magnification in the Dictator GUI, maybe the ions are not in the frame. The imaging system magnification is pretty low such that moving the CCD is usually unnecessary. To get more signal on the CCD you can remove the 90:10 beam splitter which deflects most of the light to the ion's PC and atoms CCD.

- Remember that ions are loaded into the trap even without cooling lasers. If all hell breaks loose, keep the ovens and ionization lasers on and start to scan the cooling and repump beams together in a raster fashion[40] until you hit the ions.

[37] Here you should check both the master lock in lab 185 and the slave injection lock in our lab.

[38] Labview GUI should indicate above 35 dBm.

[39] There is a flipping mirror to direct the beams to the iris instead of the ion. If the beams pass through the iris without aligning, most likely that the beam line is OK, don't touch it. The iris position which maximizes the 1092 nm beam and 422 nm beam is not exactly the same, however, it's close enough such that both beams pass through. Keep the iris aligned on the 422 nm beam.

[40] Use the last lens mounted on a translation stage, after making sure that the beams overlap on the aligning iris

Chapter 5

Article: Dynamics of a ground-state cooled ion colliding with ultracold atoms

This chapter and the resulting manuscript [1] is the essence of my PhD research. This work demonstrates the innovation of our experimental apparatus. The ion is ground-state cooled prior to interaction with the atoms. All "technical" energy scales (EMM, atoms energy) are brought to minimum and more importantly, below the fundamental energy scale for atom-ion collisions which is related to the attraction between the ion and the atom during the collision. We performed coherent spectroscopy and revealed the ion's energy distribution after few collisions and in steady-state. All the above where "for the first time" experimental efforts.

As hard the experimental effort to build and make this system work, the measured physics was mindboggling. In the beginning, it seemed like nothing adds up. Only the introduction of non-equilibrium dynamics and the resulting power-law distributions, which were initially assumed to only have a small contribution to the measured data, made all the puzzle pieces come into place.

This work paves the way towards a new quantum regime of atom-ion experiments. We believe that the results presented here will serve as a pillar work in this field. Any future work aiming at achieving ultracold temperatures will be influenced by the physics we measured and analyzed for the first time.

5.1 Abstract

Ultra-cold atom-ion mixtures are gaining increasing interest due to their potential applications in ultra-cold and state-controlled chemistry, quantum computing and many-body physics. Here, we studied the dynamics of a single ground-state cooled ion during few, to many, Langevin (spiraling) collisions with ultra-cold atoms. We measured the ion's energy distribution and observed a clear deviation from Maxwell-Boltzmann, characterized by an exponential tail, to a power-law distribution best described by a Tsallis function. Unlike previous experiments, the energy scale of atom-ion interactions is not determined by either the atomic cloud temperature or the ion's trap residual excess-micromotion energy. Instead,

it is determined by the force the atom exerts on the ion during a collision which is then amplified by the trap dynamics. This effect is intrinsic to ion Paul traps and sets the lower bound of atom-ion steady-state interaction energy in these systems. Despite the fact that our system is eventually driven out of the ultra-cold regime, we are capable of studying quantum effects by limiting the interaction to the first collision when the ion is initialized in the ground-state of the trap.

5.2 Introduction

Since its first inception [22, 23, 24], observing quantum mechanical phenomena was one of the important goals of hybrid atom-ion research [15, 16, 18, 45, 20, 19, 21]. The polarization potential between atoms and ions scales as r^{-4} and extends to 100's of nm. Similarly to other form of atomic interaction it exhibits quantum features such as Feshbach [113, 30] and shape resonances [31] at sufficiently low temperatures, however, due to its long length-scale, it is also predicted to form macroscopic objects [29]. Ultra-cold atom-ion systems are an appealing new platform for performing quantum computation [27, 28] and many-body physics [25]. However, all experiments so far relied on sympathetic cooling of the ion by the atomic cloud and were limited to the mK energy scale [114] and above.

The interplay between the ion's radio-frequency (rf) trap oscillating electric fields and sympathetic cooling has been known for a long time [35]. However, only recently the full understanding of this dynamical system is beginning to reveal [115]. In particular, it was theoretically shown that sympathetic cooling of the ion results in a non-thermal energy distribution with a power-law tail, the magnitude of which depends on the atom-ion mass ratio and trap parameters [36, 38, 39, 116, 117]. This phenomenon is closely related, among other examples, to anomalous diffusion in optical lattices [64] and is well described by non-Maxwellian statistics which was introduced by Tsallis [37]. If the ion is sufficiently lighter than the cooling atoms its mean energy diverges and collisions eventually result in ion loss from trap.

In stable mixtures the mean steady-state energy of the ion is proportional, albeit with potentially a large amplification factor, to the energy of a single collision at the trap center which is determined by, e.g., residual excess-micromotion (EMM) [38] or the atoms' temperature [39]. It is therefore interesting to ask what would determine the steady state temperature and ion dynamics when the ion is initialized in the ground state of the trap and both ion's EMM and atoms' temperature are negligible? Recently, the energy involved in a single collision was calculated to be determined by the atom-ion attraction during collision which pulls the ion away from the trap minimum into finite rf regions of the trap [43]. Furthermore, the quantum dynamics of ultra-cold atom-ion collisions was calculated and has

shown significant heating that depends on the trap parameters used [118].

5.3 Experimental setup

In this experiment, we studied the dynamics of an ion, initialized in the ground-state of all trap modes, during collisions with ultra-cold atoms and negligible EMM, thus investigating the fundamental limits to the temperature of atom-ion mixtures in Paul traps. The species we used are ^{87}Rb atoms and $^{88}Sr^{+}$ ion which have almost equal masses, in contrast to previous experiments where light atoms and heavy ions were used. This choice of masses amplifies the deviation from Maxwell-Boltzmann to a power-law energy distribution which was not observed in experiments before. Our results show a clear deviation from Maxwell-Boltzmann to a power-law distribution best described by a Tsallis function. Moreover, the heating observed in our system is consisted with that generated by the pulling of the ion from the trap center calculated by molecular dynamics simulations.

During a collision the atom is polarized by the electric field of the ion, leading to an attractive potential $V(r) = -C_4/2r^4$. Here, r is the atom-ion separation and C_4, which is proportional to the polarizability of the atom, characterizes the interaction strength. Classically, atom-ion collisions are divided into glancing and Langevin (spiraling) collisions by the impact parameter $b_c=(2C_4/E_{col})^{1/4}$, where E_{col} is the collision energy. Glancing collisions, which have a larger impact parameter than b_c, are purely elastic and involve only very small momentum transfer. In contrast, Langevin collisions involve large momentum transfer and can also lead to inelastic processes such as spin exchange or relaxation [44], charge exchange [33], molecule formation [45] and three-body recombination [46]. While the loss of atoms from the trap in the presence of an ion is dominated by glancing collisions [38] we expect the heating of the ion to be dominated by the large momentum transfer of Langevin collisions, the rate of which, $\Gamma_L = 2\pi n_{at}\sqrt{C_4/\mu}$, is energy independent. For our experimental parameters (reduced mass $\mu = (m_{at}m_{ion})/(m_{at}+m_{ion}) \approx m_{ion}/2$ and atomic peak density $n_{at} \approx 1.2 \cdot 10^{12}$ cm^{-3} - see Sec. 4.3.1) the mean time between Langevin collisions is $t_L = 1/\Gamma_L = 0.35$ ms. In-elastic processes such as reactive or three-body collisions which could change the state and energy of the ion are suppressed by 4-5 order of magnitude compared to the elastic Langevin collisions such that they don't play a significant rule.

During collisions the ion's energy distribution develops a power-law tail [36, 38, 39, 63]. We use the Tsallis distribution [37] which is a generalization of the thermal Maxwell-Boltzmann distribution to fit both our simulation (Sec. 2.5) and

experiment results,

$$P(E) = A_n \frac{E^2}{\left(1 + \frac{E}{nk_BT}\right)^n}. \tag{5.1}$$

Here, $A_n = (n-3)(n-2)(n-1)/\left(2(nk_BT)^3\right)$ is a normalization factor, k_B is the Boltzmann constant, E is the ion's energy and T and n are parameters of the distribution. In the literature, Tsallis functions are usually defined with the q-parameter, q_T. Here we define $n = 1/(q_T - 1)$ such that in the limit of $n \to \infty$ ($q_T \to 1$) the distribution in Eq. 5.1 becomes a thermal distribution of a 3D harmonic oscillator: $P(E) \propto E^2 e^{-E/k_BT}$. For finite n-values the distribution exhibits power-law asymptotic tail: $P(E) \sim E^{2-n}$. It is also important to notice that the distribution is non-normalizable for $n \leq 3$ and the distribution mean diverges for $n \leq 4$.

Our experiment (see Fig. 5.1a and Ch. 4 additional information) is designed to overlap ultra-cold ^{87}Rb atoms ($\sim$5 μK) trapped in a cross dipole trap with ground-state cooled $^{88}Sr^+$ ion ($\bar{n}<0.1$ in all three modes of motion) trapped in a linear segmented Paul trap. The ion's EMM amplitude, x_{EMM}, which is the spectral part of motion oscillating in the rf frequency (Ω_{rf}), is routinely evaluated and minimized using side-band spectroscopy on a narrow optical transition. The resulting EMM energy, $E_{EMM} = m_{ion}(x_{EMM}\Omega_{rf})^2/4$, is below 0.5 mK$\cdot k_B$. Using optical-pumping, we initialized the ion in the $5s^2S_{1/2}\,(m = -1/2)$ Zeeman sub-level (see Fig. 5.1b for the ion's energy levels scheme). The atoms are prepared in the F=1 hyperfine manifold of their ground electronic state and are not polarized. We typically overlapped 20,000 atoms with the ion for a variable interaction times ranging from 0.5 ms to several seconds, at the end of which the atoms are released from the dipole trap. Following interaction, we measured the ion's energy. Different interaction times lead to different ion energies and therefore two different ion-thermometry methods were used. Following short interaction times and with energies up to few mK, carrier Rabi spectroscopy ([60] and Sec. 3.6) of the narrow electric quadrupole transition was used. For longer interaction times, we used the Doppler re-cooling (DRC) method [119] on a strong dipole allowed transition [120].

Each experimental run, typically lasting few seconds of atom cloud preparation, transport and atom-ion interaction, ended with ion interrogation. Since atom-ion collisions lead to spin de-polarization [44, 121], we used a short optical pumping (OP) pulse to transfer the population back to the $5s^2S_{1/2}\,(m = -1/2)$ state before performing Rabi spectroscopy. Immediately after, we shined a pulse of light resonant with the $5s^2S_{1/2}\,(m = -1/2) \to 4d^2D_{5/2}\,(m = -5/2)$ narrow quadrupole transition for a duration t_R, after which we determined whether the ion was shelved to the meta-stable D-state using state selective fluorescence on the $S_{1/2} \to P_{1/2}$

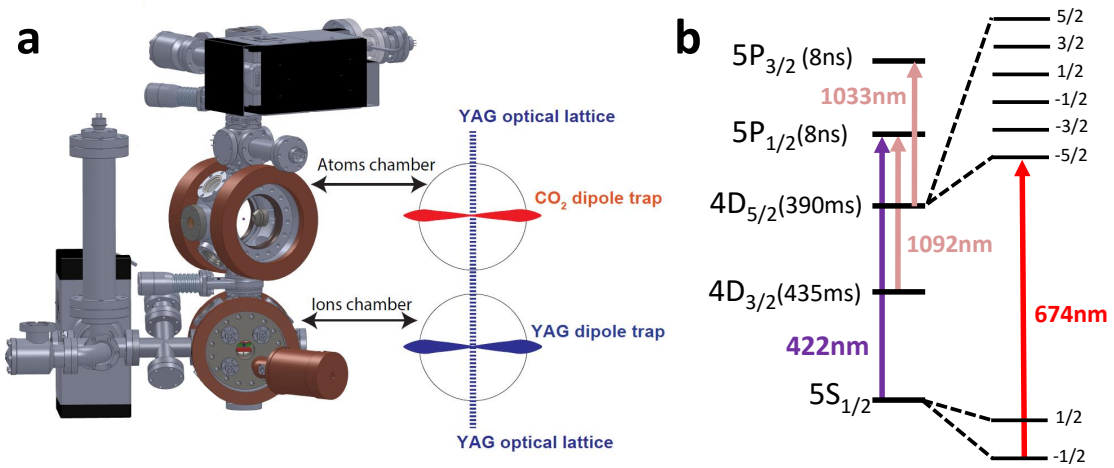

Figure 5.1: **a) Experimental system.** Our apparatus is composed of two vacuum chambers, connected by a thin tube. In the top chamber, we collected atoms and cooled them to a temperature of several μK using standard magneto-optical trapping and evaporative cooling in a CO_2 dipole trap. We then transfered the atoms to the bottom chamber using a 1-D moving optical lattice where they are re-trapped in a crossed dipole trap and overlapped with a single ground-state cooled ion. **b) $^{88}Sr^+$ ion energy levels.** We prepared the ion in the $5s^2S_{1/2}$ ($m = -1/2$) electronic and Zeeman ground-state. We used a narrow line-width laser resonant with the $S_{1/2} \rightarrow D_{5/2}$ quadrupole transition at 674nm together with a re-pump laser resonant with the $D_{5/2} \rightarrow P_{3/2}$ at 1033nm to perform coherent Rabi thermometry. We used a 422nm laser resonant with the $S_{1/2} \rightarrow P_{1/2}$ dipole transition together with a 1092nm re-pump on the $D_{3/2} \rightarrow P_{1/2}$ transition for state-selective fluorescence and Doppler re-cooling thermometry.

transition. The shelving probability is given by,

$$P_D\left(t_R\right)=\sum_{\mathbf{n}}P\left(\mathbf{n}\right)\sin^2\left(\Omega_{\mathbf{n}}t_R\right). \tag{5.2}$$

Here, $\mathbf{n}=(n_x,n_y,n_z)$ is the ion's harmonic oscillator state. $\Omega_{\mathbf{n}}=\Omega_0\prod_i e^{-\frac{\eta_i^2}{2}}L_{n_i}\left(\eta_i^2\right)$ is the carrier Rabi frequency with Ω_0 the bare Rabi frequency, $L_{n_i}\left(x\right)$ is the Laguerre polynomial of degree n_i and η_i is the Lamb-Dicke parameter of the i-th mode. The ion's total energy is $E=\sum_{i=x,y,z}(\hbar\omega_i n_i+1/2)$ where $\omega_i/2\pi$ is the i-th mode frequency and $\hbar$ is the reduced Planck constant. The ion's energy distribution $P\left(E\right)$ is given by Eq. 5.1.

5.4 Atom-ion distribution after few collisions

The experimental results for atom-ion interaction times lasting up to 6.5ms, which correspond to up to 20 Langevin collisions on average, are shown in figures 5.2a-f. We scanned the pulse duration, t_R, and fitted the measured shelving probability (shown by the filled circles) to Eq. 5.2 using the distribution of Eq. 5.1. We estimated the distribution free parameters, T and n, using maximum likelihood (Sec. 5.8) (the best fit is shown by solid lines). As seen, the ion heats up due to collisions with the atoms, and as it does, the contrast of the flopping curve decays due to incoherent sum of contributions from different motional states. As seen in Fig. 5.2h, the energy distribution changes from thermal ($n\gg1$) to a power-law distribution with n=4.0(2) over the course of several collisions. A comparison to the best fitted thermal distribution is shown by the dashed lines in figures 5.2a-f. As seen, a thermal distribution fails to faithfully explain our observations.

Once the energy distribution of the ion has been determined, we examined the rate of ion heating as a function of the interaction time. Since the ion's mean energy is not well defined for this power-law we characterized the distribution using the most probable energy, E_{mode},

$$k_BT_{Ion}=E_{mode}/2=k_BTn/\left(n-2\right), \tag{5.3}$$

which we will hereafter refer to as the ion's temperature. Note that for thermal distribution $T_{Ion}=T$. The temperature of the ion is shown by the filled circles in Fig. 5.2g. The heating is linear with a rate of 296(37) μK/ms which corresponds to, on average, 100(13) μK per collision. After 6.5 ms the ion's temperature exceeds 2 mK and the carrier thermometry losses sensitivity. At this point the ion has already heated up significantly beyond its EMM energy. It is important to note that even though our ion is initialized in the ground-state the first point in Fig. 5.2g is significantly higher than the ground-state temperature. This is due

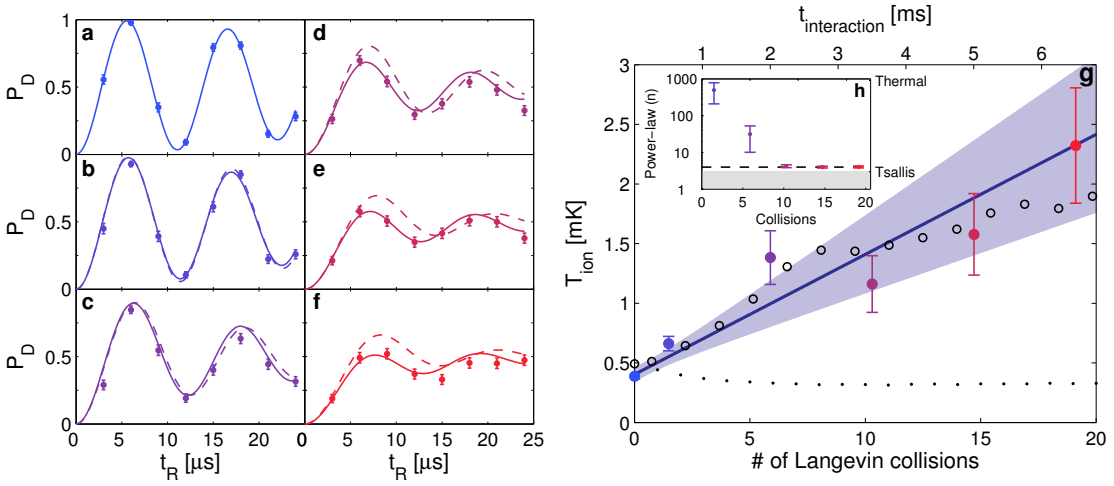

Figure 5.2: **Carrier Rabi spectroscopy for few atom-ion Langevin collisions. a-f)** Each graph corresponds to a different interaction time (0,0.5,2,3.5,5,6.5 ms for graphs a-f). We scanned the shelving pulse time t_R, and measured the shelving probability P_D. Each data point corresponds to 170 experiments. Error-bars are binomial distribution standard-deviation. We fitted the data using Eq. 5.2 together with the Tsallis distribution (Eq. 5.1). We extracted the distribution free parameters (T and n) using maximum likelihood estimation (Sec. 5.8). The resulting curve is shown in solid lines. Dashed lines show fit of our data to a thermal distribution. **g)** The ion's temperature ($T_{Ion} = Tn/(n-2)$) increases linearly with a rate of 296(37) μK/ms which is equivalent to 100(13) μK per collision. Error-bars are one sigma standard deviation. Shaded area represents linear fit confidence bounds (one sigma). Open circles are the results of a simulation which takes into account the reaction of the polarization potential on the ion's position. Black dots are simulation results taking into account only hard-sphere collisions. **h)** Ion's power-law parameter, n. The ion's energy distribution starts with $n \gg 1$ consistent with a Maxwell-Boltzman distribution, and converges to n=4.0(2) after $\sim$10 collisions. For n>10 Thermal and Tsallis distributions are almost indistinguishable as can be seen in 5.2a-c. The grey shaded area represents the non-normalizable region of the distribution (n<3). The dashed line represent the threshold (n=4) for mean energy divergence.

to beam-pointing drifts during the longer than day data acquisition time in this experiment. The beam pointing only affects the cold temperature points at which Rabi flops have high contrast (Fig. 5.2a).

To gain better understanding of the heating dynamics, we compared our results to a molecular-dynamics simulation (Sec. 2.5). First, we used a simulation similar to Ref. [38] which only takes into account hard-sphere collisions and therefore is only affected by EMM and the temperature of the atoms (black dots in Fig. 5.2g). Here, the ion equilibrates with the residual EMM energy (set to 0.5 mK$\cdot k_B$ in the simulation). The resulting ion's energy distribution is also power-law with n=3.83. However, the ion's steady-state temperature of ∼0.35 mK is almost order of magnitude lower than the last data point of our experimental results which shows no steady-state behavior in the measured regime. As a second step, we added to our simulation the polarization force between the atom and ion and calculated the particles trajectories in a similar fashion to Ref. [43] (empty circles in Fig. 5.2g). In this case, the simulation faithfully reproduces our experimental results. The ion's temperature increases linearly at the experimental rate to 2 mK and the distribution power-law, n, converges to n=3.8. While the steady-state power-law of the distribution is the same in both simulations, implying that the power-law is independent of the heating mechanism, the resulting steady-state temperature is considerably different. As seen, in the absence of EMM and negligible atomic temperature, the ion dynamics is dominated by the reaction of the polarization potential on the ion, pulling it away from the trap center into finite RF-regions in the trap. This is the first observation of atom-ion collision dynamics which is not determined by the atom's temperature or the ion's EMM.

5.5 Atom-ion distribution in steady-state

The heating rates measured using Carrier Rabi spectroscopy of the narrow linewidth transition show a linear increase in temperature throughout the entire measurement range (few mK). To measure the ion's temperature after longer interaction times we used DRC thermometry, which is sensitive from ∼10 mK to few Kelvin. We performed DRC using a laser slightly red-detuned (-1.8 MHz) from the $5s^2S_{1/2} \rightarrow 5p^2P_{1/2}$ dipole transition and a re-pump red-detuned (-16.5 MHz) from the $4d^2D_{3/2} \rightarrow 5p^2P_{1/2}$ transition. In the re-cooling analysis we took into account the eight-levels involved in the DRC, cooling of all the ion modes, radiation pressure, effects of ion micromotion and the non-thermal energy distribution of the ion [122].

To better understand the role of EMM on our ion's steady-state temperature, we scanned the EMM energy by almost three orders of magnitude from 0.5 to 200 mK$\cdot k_B$. We overlapped the atoms with the ion for 200 ms during which more

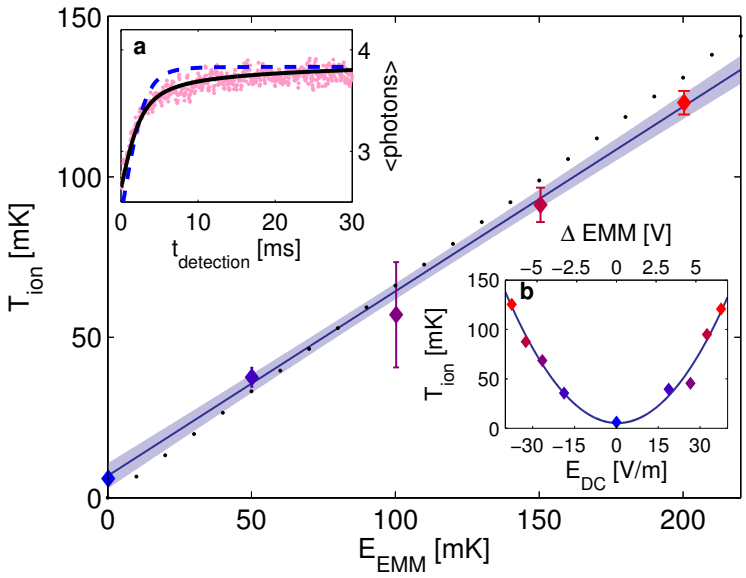

Figure 5.3: **Ion's steady-state temperature after 100's of atom-ion collisions.** We extracted the ion's temperature from a fit to a time resolved fluorescence signal. Figure inset (a) shows a re-cooling curve (pink dots, 150μs moving average) for 150 mK$\cdot k_B$ EMM experiment and a fit for power-law (black solid line) and thermal (blue dashed line) energy distributions. Figure inset (b) shows the ion's temperature as function of the difference in the voltage on the electrode from the compensated value (top x-axis) and the resulting electric field at the ion's position (bottom x-axis). The solid blue line shown is a parabolic fit. In the main figure, the two opposing-sign DC-voltages configurations are averaged to show the ion temperature vs. the EMM kinetic energy. Error-bars accounts for both fit confidence intervals (one sigma) and the statistics of averaging over the two opposing EMM points. The solid blue line is a linear fit for the data: $T_{Ion} = 0.575(19)E_{EMM}/k_B + 6.8(2.4)$ mK. Shaded area represents fit confidence bounds (one sigma). The black points are the results of a simulation ($T_{Ion} = 0.656E_{EMM}/k_B$) which takes into account only the effect of hard sphere collisions.

than 400 Langevin collisions occur on average. After interaction, we detected the time-resolved fluorescence signal with 50 μs binning and up to 50 ms. As the ion cools during detection, the fluorescence signal increases. We detected on average four photons in each bin. We repeated the experiment 350 times to improve our signal-to-noise ratio. We fitted the fluorescence curve to our DRC model using the power-law distribution (Eq. 5.1) with a single fit parameter, T. The power-law parameter, n, is fixed to the value extracted from a simulation which changes from n=3.9-4.2 between low and high EMM energies due to the atomic cloud finite size. The results are shown in Fig. 5.3. We observed a linear dependence of the ion's temperature with the EMM energy, $T_{Ion} = 0.575(19)E_{EMM}/k_B + 6.8(2.4)$ mK. The scaling predicted from a simulation of hard-sphere collisions only, is $T_{Ion} = 0.656E_{EMM}/k_B$ which has a slightly higher slope, probably due to inaccuracies in DRC modeling and atomic cloud size uncertainties. However, the main difference between the simulation and the experiment is the steady-state temperature when EMM is compensated. When EMM is compensated below 0.5 mk$\cdot k_B$, a simulation of hard-sphere collisions predicts a steady state temperature of similar magnitude (as shown in Fig. 5.3 by the crossing of the simulation data (black dots) in the origin), whereas our data indicates a steady-state temperature at least an order of magnitude higher. This is a second indication for dynamics beyond simple hard-sphere collisions. In the figure inset we show that even the Doppler re-cooling signal is sensitive, at-least qualitatively, to the deviation of the ion's energy distribution from thermal (best fit shown by dashed line) to power-law (similarly by solid line). Here however, DRC is not sensitive enough to extract the exact power-law from the experimental data.

5.6 Atom-ion dynamics

To study the approach to steady state in the presence of EMM we measured the ion's temperature using DRC after short interaction times. The ion's temperature, as it approaches steady-state, in the presence of EMM with 100 mK$\cdot k_B$ average kinetic energy is plotted in Fig. 5.4 (magenta diamonds). From an exponential fit, we extracted a time-scale (1/e) of 3.6(2.8) collisions to reach steady-state. We compared this collision time-scale with a simulation of hard-sphere collisions which yields a time-scale (1/e) of 7.7 collisions to reach steady-state regardless of the EMM energy (black dots). This time-scale is a signature of EMM dominated collisions where the ion quickly equilibrates with the EMM. In the absence of EMM, we observed a slow approach to steady state (64(14) collisions) which is extracted from the heating rate (100(13) μK/Coll.) measured using Rabi spectroscopy (Fig. 5.2g) and the steady-state (6.8(2.4) mK) measured using DRC (Fig. 5.3). This observation is the third indication for different dynamics in the absence of EMM.

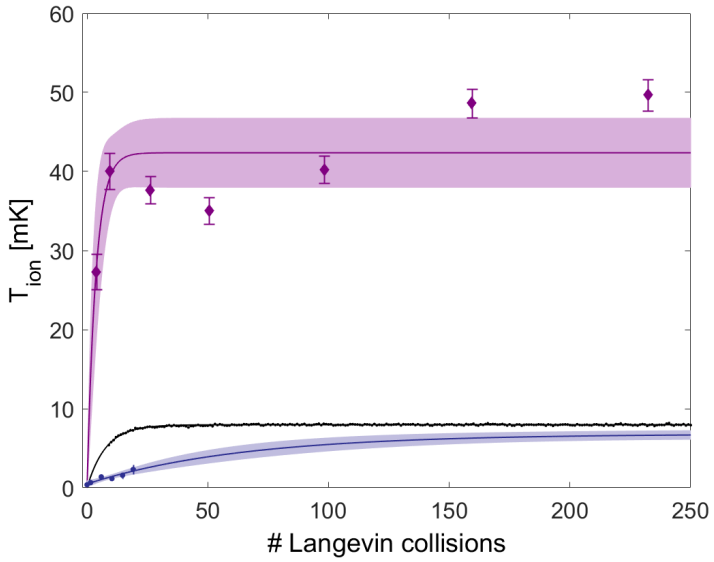

Figure 5.4: **Ion's heating dynamics.** Ion's temperature as it approaches steady-state for 100 mK·k_B EMM energy (purple diamonds) measured using DRC. From an exponential fit (purple solid line) we calculated 3.6(2.8) (1/e) collisions to reach steady-state which is with reasonable agreement with the number of collisions, 7.7, extracted from a simulation including only hard-sphere collisions. Error-bars are re-cooling fit confidence intervals (one sigma). Shaded area represents fit confidence bounds (one sigma). We compared this result to the heating rate measured using Rabi spectroscopy (Fig. 5.2g, blue circles in this figure) and the steady-state measured using DRC (Fig. 5.3, not shown in this figure) for EMM energy less than 0.5 mK·k_B. From an exponential fit (blue solid line) we calculated 64(14) collisions (1/e) to reach steady-state. For comparison, we show a hard-sphere collisions simulation results (black dots) with EMM energy (12 mK·k_B) which results in the same steady-state temperature. Here, the number of collisions (7.7) required to reach this temperature is much smaller.

5.7 Conclusion

To conclude, we used two complementary techniques to measure the ion's temperature and energy distribution after short (few collisions) and long (100s' of collisions) interaction times between a single trapped-ion, initialized in the trap ground-state and a cloud of ultra-cold atoms in the presence of negligible EMM. Our measurements allowed us to characterize the deviation of the ion's energy distribution from Maxwell-Boltzmann to a power-law distribution described by Tsallis function. This deviation from a thermal distribution was emphasized by the use of an ion-atom mixture of nearly equal-mass species. Our system can be further used to study non-equilibrium thermodynamics. We have seen that, in the regime of negligible EMM, ion heating is dominated by the pulling of the ion from the trap center by the atom. Although the steady-state temperature of our ion is far from the quantum regime, the heating rate is sufficiently slow to enable us to study ultra-cold interactions by preparing the ion in its electronic and motional ground-state and limiting the interaction to the first few collisions.

This work was supported by the Crown Photonics Center, ICore-Israeli excellence center circle of light, the Israeli Science Foundation, the US-Israel Binational Science Foundation, and the European Research Council.

5.8 Supplemental Material

Likelihood estimation

We performed a likelihood analysis to extract the Tsallis distribution parameters, n and T (Eq. 1 in the main text). The likelihood function is defined as: $L(n,T) = \prod_i L_i(x_i; N_i, p_i)$ where $L_i(x_i; N_i, p_i) = \binom{N_i}{x_i} p_i^{x_i} (1-p_i)^{N_i - x_i}$ is the likelihood to measure x_i dark ion events out of N_i measurements assuming that the ion's D-state population is exactly p_i. The index i represents the different pulse times, t_R, in the experiment. The D-state population, $p_i(n,T)$ is determined from evaluating Eq. 2 in the main text using Tsallis distribution with given parameters, n and T. From the likelihood function $L(n,T)$ we extracted the mean and standard-deviation of the distribution parameters and also the ion's temperature (Eq. 3 in the main text). The likelihood values for the different experimental data shown in Fig. 2 b-f in the main text and the ion's temperature for both the Tsallis and Maxwell-Boltzmann energy distribution are shown in Table 5.1.

Interaction time	$\log_{10}(L_{\mathrm{MBD}})$	$\mathrm{T}_{\mathrm{Ion}}^{\mathrm{MBD}}$ [mK]	$\log_{10}(L_{\mathrm{TD}})$	$\mathrm{T}_{\mathrm{Ion}}^{\mathrm{TD}}$ [mK]
0.5 ms	-13.98	0.62	-13.24	0.66
2 ms	-16.55	1.60	-15.69	1.38
3.5 ms	-19.31	2.62	-12.86	1.16
5 ms	-19.54	4.23	-10.44	1.58
6.5 ms	-19.51	4.96	-11.99	2.32

Table 5.1: **Likelihood estimation.** Likelihood values and ion's temperature for the data given in Fig. 2 b-f in the main text for both Tsaliis distribution (TD) and Maxell-Boltzmann distribtuion (MBD).

Doppler re-cooling

We used a semi-classical model for Doppler recooling as described in Ref. [123]. When the atom is Doppler cooled by a single laser cooling beam and a single re-pump beam, the time dependence of the ion's fluorescence rate can be used to measure its initial energy distribution.

The thermometry is based on a fact that the ion's fluorescence depends on the Doppler shifts induced by the ion's motion. The ion's emitted fluorescence increases as the ion cools down and the Doppler shifts decrease until the ion reaches the Doppler cooling limit.

We modeled the Doppler shifts assuming a velocity distribution of a 3D harmonic oscillator as described in Ref. [119]. We further extended the model to 3-level atom and we also included the effect of inherent micromotion.

Chapter 6
Outlook

This thesis outlines the building of an advanced apparatus for performing experiments with ground-state cooled and excess-micromotion compensated ions interacting with ultracold atoms. The main outcome of this thesis was the measurement of the energy distribution of the ion during elastic collisions with ultracold atoms which grows a power-law tail of high energies. The observed non-equilibrium dynamics emanates from the intrinsic nature of the ion's Paul trap. Unintentionally, we found out that our system is well suited for studying this kind of physics and we plan to continue this line of work.

Our system is also suited for studying ultracold physics, which was our initial goal, by limiting the interaction to a single collision. We plan to look on different methods to reduce the ion's steady-state temperature and power-law tail. We can change the trap parameters, e.g. trap and rf frequencies, and possibly find more energetically stable points [118]. We can also drastically reduce the atomic cloud size in one dimension by loading the atoms into a single lattice site. This should reduce the effect of multiple collisions. The best way to reduce the steady-state temperature, which is not experimentally feasible with our current system, is to use the lightest atom species and heaviest ions possible. This road is perused by the Amsterdam and Firenze groups.

There are other approaches for studying atom-ion physics. One prominent alternative, pursued by the Freiburg group in Germany [56], uses an optical dipole trap for ion trapping instead of a Paul trap. Here, the system is not coupled to the environment and sympathetic cooling of the ion to the atoms' temperature with Maxwell-Boltzmann distribution is expected. However, there are still many obstacles to overcome. Currently, the longest ion's life time in a dipole trap is only few ms. Trap frequencies are expected to lie outside the Lamb-Dicke regime such that coherent manipulation and control are much more difficult. An interesting approach might be to use an hybrid Paul-dipole trap. Ion preparation and readout is performed in the Paul trap while the interaction takes place in the optical trap. The ion is transferred between the traps adiabatically.

Additional approach is to use a multi-pole trap for ions [55] which is an higher order extension of the Paul trap. Here the trapping potential scale like r^{2n-2} where n is the pole order (Paul/quadrupole trap: n=2, octupole trap: n=4 etc.). For high pole number the trap becomes box-like and micromotion effects are suppressed.

Nonetheless, since the particle is almost free it is much harder to use motional sidebands for coherent control. Penning traps are also used for trapping ions and recently even for ground-state cooling [124]. However, the high frequency magnetron motion of the ions in Penning trapa will introduce similar difficulties to those of micromotion in Paul traps.

While the main focus of this thesis is on elastic collisions, we also performed preliminary experiments involving in-elastic processes. Here, the main motivation is to suppress (or enhance) in-elastic effects by controlling the initial state polarization. We achieved 85% spin alignment when the atoms are prepared either in the $|F=2,m_F=-2\rangle$ stretched state or in the $|F=1,m_F=-1\rangle$ state regardless of the ion's initial spin polarization (collisional pumping). In our system the spin exchange to spin relaxation rates ratio is an order of magnitude higher than in the Yb^+-Rb system [44]. This discrepancy between the systems can lead to better understanding of the spin relaxation process.

We see dependence of the charge-exchange rate on both the spin orientation and the collision energy. This might suggest that three-body collisions contribute to the charge-exchange rate [68]. Charge-exchange rates are highly suppressed with respect to the Langevin collision rate, even when the ion is initialized in the meta-stable $D_{5/2}$ state. In the Yb^+-Rb system, initializing the ion in exited states led to ion loss in every Langevin collision [33]. Again, this discrepancy between the systems can shed light on the relaxation process.

A hallmark of quantum interactions is the appearance of shape-resonances in the spectrum. The physics behind shape-resonances is very similar to Fabry-Pérot cavities. By tuning the collision energy with a quasi-bound state of the potential energy, long-lived molecular states will emerge thus changing significantly the collision cross section. Theory predicts the appearance of shape-resonances at relatively high temperatures of up to 10's mK [31]. However, they yet to be observed experimentally due to the broad ion's energy distribution at steady-state. We plan to observe shape-resonances by changing the relative energy between the atoms and the ion while keeping the temperature close to ground-state. This is done by sweeping repetitively the atoms through the ion at controlled velocity using the optical lattice. In each sweep less than a single atom-ion collision occurs such that the temperature remains in the ground-state but the energy of the collision is determined by the relative velocity.

To conclude, there are many avenues to explore with this system: from non-equilibrium dynamics through ultracold chemistry up to quantum information and many body simulations. I wish the best of luck for the coming students who will continue the work on this apparatus.

Bibliography

[1] Meir, Z. *et al.* Dynamics of a ground-state cooled ion colliding with ultra-cold atoms. *arXiv preprint arXiv:1603.01810v2* (2016).

[2] Meir, Z., Schwartz, O., Shahmoon, E., Oron, D. & Ozeri, R. Cooperative Lamb shift in a mesoscopic atomic array. *Phys. Rev. Lett.* **113**, 193002 (2014).

[3] Harty, T. P. *et al.* High-fidelity preparation, gates, memory, and readout of a trapped-ion quantum bit. *Phys. Rev. Lett.* **113**, 220501 (2014).

[4] Gaebler, J. *et al.* High-fidelity universal gate set for ^{9} Be^{+} ion qubits. *arXiv preprint arXiv:1604.00032* (2016).

[5] Kotler, S., Akerman, N., Glickman, Y., Keselman, A. & Ozeri, R. Single-ion quantum lock-in amplifier. *Nature* **473**, 61–65 (2011).

[6] Kotler, S., Akerman, N., Navon, N., Glickman, Y. & Ozeri, R. Measurement of the magnetic interaction between two bound electrons of two separate ions. *Nature* **510**, 376–380 (2014).

[7] Cornell, E. A. & Wieman, C. E. Nobel lecture: Bose-Einstein condensation in a dilute gas, the first 70 years and some recent experiments. *Reviews of Modern Physics* **74**, 875 (2002).

[8] DeMarco, B. & Jin, D. S. Onset of Fermi degeneracy in a trapped atomic gas. *Science* **285**, 1703–1706 (1999).

[9] Bloch, I., Dalibard, J. & Zwerger, W. Many-body physics with ultracold gases. *Reviews of Modern Physics* **80**, 885 (2008).

[10] Bloch, I., Dalibard, J. & Nascimbene, S. Quantum simulations with ultracold quantum gases. *Nature Physics* **8**, 267–276 (2012).

[11] Endres, M. *et al.* The 'Higgs' amplitude mode at the two-dimensional superfluid/Mott insulator transition. *Nature* **487**, 454–458 (2012).

[12] Härter, A. & Hecker Denschlag, J. Cold atom–ion experiments in hybrid traps. *Contemporary Physics* **55**, 33–45 (2014).

[13] Zipkes, C., Ratschbacher, L., Palzer, S., Sias, C. & Köhl, M. Hybrid quantum systems of atoms and ions. In *Journal of Physics: Conference Series*, vol. 264, 012019 (IOP Publishing, 2011).

[14] Willitsch, S. Ion-atom hybrid systems. *Ion Traps for Tomorrows Applications* 255–268 (2014).

[15] Zipkes, C., Palzer, S. & Köhl, M. A trapped single ion inside a Bose-Einstein condensate. *Nature* **464**, 388 (2010).

[16] Schmid, S., Härter, A. & Denschlag, J. H. Dynamics of a cold trapped ion in a Bose-Einstein condensate. *Phys. Rev. Lett.* **105**, 133202 (2010).

[17] Willitsch, S., Bell, M. T., Gingell, A. D., Procter, S. R. & Softley, T. P. Cold reactive collisions between laser-cooled ions and velocity-selected neutral molecules. *Phys. Rev. Lett.* **100**, 043203 (2008).

[18] Rellergert, W. G. *et al.* Measurement of a large chemical reaction rate between ultracold closed-shell ^{40}Ca atoms and open-shell $^{174}Yb^{+}$ ions held in a hybrid atom-ion trap. *Phys. Rev. Lett.* **107**, 243201 (2011).

[19] Ravi, K., Seunghyun, L., Arijit, S., Werth, G. & S.A., R. Cooling and stabilization by collisions in a mixed ion-atom system. *Nat. Commun* **3**, 1126 (2012).

[20] Sivarajah, I., Goodman, D. S., Wells, J. E., Narducci, F. A. & Smith, W. W. Evidence of sympathetic cooling of Na^{+} ions by a Na MOT in a hybrid trap. *Phys. Rev. A* **86**, 063419 (2012).

[21] Haze, S., Hata, S., Fujinaga, M. & Mukaiyama, T. Observation of elastic collisions between lithium atoms and calcium ions. *Phys. Rev. A* **87**, 052715 (2013).

[22] Makarov, O. P., Côté, R., Michels, H. & Smith, W. W. Radiative charge-transfer lifetime of the excited state of $(NaCa)^{+}$. *Phys. Rev. A* **67**, 042705 (2003).

[23] Smith, W. W., Makarov, O. P. & Lin, J. Cold ion-neutral collisions in a hybrid trap. *J. Mod. Phys.* **52**, 2253–2260 (2005).

[24] Grier, A. T., Cetina, M., Oručević, F. & Vuletić, V. Observation of cold collisions between trapped ions and trapped atoms. *Phys. Rev. Lett.* **102**, 223201 (2009).

[25] Bissbort, U. *et al.* Emulating solid-state physics with a hybrid system of ultracold ions and atoms. *Phys. Rev. Lett.* **111**, 080501 (2013).

[26] Gerritsma, R. *et al.* Bosonic Josephson junction controlled by a single trapped ion. *Phys. Rev. Lett.* **109**, 080402 (2012).

[27] Joger, J., Negretti, A. & Gerritsma, R. Quantum dynamics of an atomic double-well system interacting with a trapped ion. *Phys. Rev. A* **89**, 063621 (2014).

[28] Doerk, H., Idziaszek, Z. & Calarco, T. Atom-ion quantum gate. *Phys. Rev. A* **81**, 012708 (2010).

[29] Côté, R., Kharchenko, V. & Lukin, M. D. Mesoscopic molecular ions in Bose-Einstein condensates. *Phys. Rev. Lett.* **89**, 093001 (2002).

[30] Tomza, M., Koch, C. P. & Moszynski, R. Cold interactions between an yb^+ ion and a Li atom: Prospects for sympathetic cooling, radiative association, and Feshbach resonances. *Phys. Rev. A* **91**, 042706 (2015).

[31] da Silva Jr, H., Raoult, M., Aymar, M. & Dulieu, O. Formation of molecular ions by radiative association of cold trapped atoms and ions. *New Journal of Physics* **17**, 045015 (2015).

[32] Aymar, M., Guérout, R. & Dulieu, O. Structure of the alkali-metal-atom + strontium molecular ions: Towards photoassociation and formation of cold molecular ions. *The Journal of Chemical Physics* **135**, 064305 (2011).

[33] Ratschbacher, L., Zipkes, C., Sias, C., & Köhl, M. Controlling chemical reactions of a single particle. *Nat Phys* **8**, 649–652 (2012).

[34] Paul, W. & Steinwedel, H. Notizen: Ein neues massenspektrometer ohne magnetfeld. *Zeitschrift für Naturforschung A* **8**, 448–450 (1953).

[35] Major, F. G. & Dehmelt, H. G. Exchange-collision technique for the rf spectroscopy of stored ions. *Phys. Rev.* **170**, 91–107 (1968).

[36] DeVoe, R. G. Power-law distributions for a trapped ion interacting with a classical buffer gas. *Phys. Rev. Lett.* **102**, 063001 (2009).

[37] Tsallis, C. Possible generalization of Boltzmann-Gibbs statistics. *Journal of statistical physics* **52**, 479–487 (1988).

[38] Zipkes, C., Ratschbacher, L., Sias, C. & Köhl, M. Kinetics of a single trapped ion in an ultracold buffer gas. *New Journal of Physics* **13**, 053020 (2011).

[39] Chen, K., Sullivan, S. T. & Hudson, E. R. Neutral gas sympathetic cooling of an ion in a Paul trap. *Phys. Rev. Lett.* **112**, 143009 (2014).

[40] Bardou, F. *Lévy statistics and laser cooling: how rare events bring atoms to rest* (Cambridge University Press, 2002).

[41] Zaburdaev, V., Denisov, S. & Klafter, J. Lévy walks. *Rev. Mod. Phys.* **87**, 483–530 (2015).

[42] Berkeland, D. J., Miller, J. D., Bergquist, J. C., Itano, W. M. & Wineland, D. J. Minimization of ion micromotion in a paul trap. *Journal of Applied Physics* **83**, 5025–5033 (1998).

[43] Cetina, M., Grier, A. T. & Vuletic, V. Micromotion-induced limit to atom-ion sympathetic cooling in Paul traps. *Phys. Rev. Lett.* **109**, 253201 (2012).

[44] Ratschbacher, L. *et al.* Decoherence of a single-ion qubit immersed in a spin-polarized atomic bath. *Phys. Rev. Lett.* **110**, 160402 (2013).

[45] Hall, F. H. J., Aymar, M., Bouloufa-Maafa, N., Dulieu, O. & Willitsch, S. Light-assisted ion-neutral reactive processes in the cold regime: Radiative molecule formation versus charge exchange. *Phys. Rev. Lett.* **107**, 243202 (2011).

[46] Härter, A. *et al.* Population distribution of product states following three-body recombination in an ultracold atomic gas. *Nat Phys* **9**, 512–517 (2013).

[47] Steck, D. A. Rubidium 87 D line data (2001).

[48] Dalibard, J. Collisional dynamics of ultra-cold atomic gases. In *Proceedings of the International School of Physics-Enrico Fermi*, vol. 321 (1999).

[49] Langevin, M. Une formule fondamentale de théorie cinétique. In *Annales de chimie et de physique, Series*, vol. 5, 245–288 (1905).

[50] Söding, J., Guéry-Odelin, D., Desbiolles, P., Ferrari, G. & Dalibard, J. Giant spin relaxation of an ultracold cesium gas. *Phys. Rev. Lett.* **80**, 1869–1872 (1998).

[51] Krükow, A., Mohammadi, A., Härter, A., & Denschlag, J. H. Reactive two-body and three-body collisions of Ba^+ in an ultracold Rb gas. *arXiv:1602.01381* (2016).

[52] Moses, S. A. *et al.* Creation of a low-entropy quantum gas of polar molecules in an optical lattice. *Science* **350**, 659–662 (2015).

[53] Paul, W. Electromagnetic traps for charged and neutral particles. *Reviews of modern physics* **62**, 531 (1990).

[54] Dehmelt, H. Experiments with an isolated subatomic particle at rest. *Reviews of modern physics* **62**, 525 (1990).

[55] Wester, R. Radiofrequency multipole traps: tools for spectroscopy and dynamics of cold molecular ions. *Journal of Physics B: Atomic, Molecular and Optical Physics* **42**, 154001 (2009).

[56] Huber, T., Lambrecht, A., Schmidt, J., Karpa, L. & Schaetz, T. A far-off-resonance optical trap for a Ba^+ ion. *Nature communications* **5** (2014).

[57] Mathieu, E. Mémoire sur le mouvement vibratoire d'une membrane de forme elliptique. *Journal de mathématiques pures et appliquées* 137–203 (1868).

[58] D. J., W. *et al.* Experimental issues in coherent quantum-state manipulation of trapped atomic ions. *J. Res. Natl. Inst. Stand. Technol.* **103**, 259–328 (1998).

[59] King, B. E. *Quantum state engineering and information processing with trapped ions.* Ph.D. thesis, University of Colorado (1999).

[60] Leibfried, D., Blatt, R., Monroe, C. & Wineland, D. Quantum dynamics of single trapped ions. *Rev. Mod. Phys.* **75**, 281 (2003).

[61] James, D. Quantum dynamics of cold trapped ions with application to quantum computation. *Applied Physics B* **66**, 181–190.

[62] Schwarz, S. Simulations for ion traps buffer gas cooling. In *Trapped Charged Particles and Fundamental Interactions*, 1–21 (Springer, 2008).

[63] Höltkemeier, B., Weckesser, P., López-Carrera, H. & Weidemüller, M. Buffer-gas cooling of a single ion in a multipole radio frequency trap beyond the critical mass ratio. *Phys. Rev. Lett.* **116**, 233003 (2016).

[64] Lutz, E. Anomalous diffusion and Tsallis statistics in an optical lattice. *Phys. Rev. A* **67**, 051402 (2003).

[65] Lutz, E. & Renzoni, F. Beyond Boltzmann-Gibbs statistical mechanics in optical lattices. *Nature Physics* **9**, 615–619 (2013).

[66] Umarov, S., Tsallis, C. & Steinberg, S. On a q-central limit theorem consistent with nonextensive statistical mechanics. *Milan journal of mathematics* **76**, 307–328 (2008).

[67] Zipkes, C., Palzer, S., Ratschbacher, L., Sias, C. & Köhl, M. Cold heteronuclear atom-ion collisions. *Phys. Rev. Lett.* **105**, 133201 (2010).

[68] Krükow, A. *et al.* Energy scaling of cold atom-atom-ion three-body recombination. *arXiv:1510.04938v2* (2016).

[69] Dutta, S., Sawant, R. & Rangwala, S. Collisional cooling of light ions by co-trapped heavy atoms. *arXiv preprint arXiv:1512.04197* (2015).

[70] Lechner, R. *et al.* Electromagnetically-induced-transparency ground-state cooling of long ion strings. *Physical Review A* **93**, 053401 (2016).

[71] Ejtemaee, S. & Haljan, P. 3d sisyphus cooling of trapped ions. *arXiv preprint arXiv:1603.01248* (2016).

[72] J.D. Siverns, S. W., L.R. Simkins & Hensinger, W. On the application of radio frequency voltages to ion traps via helical resonators. *Applied Physics B* (2012).

[73] Harty, T. P. *High-fidelity microwave-driven quantum logic in intermediate-field* $^{43}Ca^{+}$. Ph.D. thesis, University of Oxford (2013).

[74] Johnson, K. *et al.* Active stabilization of ion trap radiofrequency potentials. *Review of Scientific Instruments* **87**, 053110 (2016).

[75] Likforman, J.-P., Tugayé, V., Guibal, S. & Guidoni, L. Precision measurement of the branching fractions of the $5p\,^2p_{1/2}$ state in $^{88}Sr^{+}$ with a single ion in a microfabricated surface trap. *Phys. Rev. A* **93**, 052507 (2016).

[76] Lamb, W. E. & Retherford, R. C. Fine structure of the hydrogen atom by a microwave method. *Physical Review* **72**, 241–243 (1947).

[77] Dicke, R. Coherence in spontaneous radiation processes. *Physical Review* **93**, 99 (1954).

[78] Fain, V. On the theory of the coherent spontaneous emission. *Sov. Phys. JETP* **9**, 562–565 (1959).

[79] Lehmberg, R. Radiation from an n-atom system. i. general formalism. *Physical Review A* **2**, 883 (1970).

[80] Arecchi, F. & Kim, D. Line shifts in cooperative spontaneous emission. *Optics Communications* **2**, 324–328 (1970).

[81] Friedberg, R., Hartmann, S. R. & Manassah, J. T. Frequency shifts in emission and absorption by resonant systems ot two-level atoms. *Physics Reports* **7**, 101–179 (1973).

[82] Keaveney, J. *et al.* Cooperative lamb shift in an atomic vapor layer of nanometer thickness. *Phys. Rev. Lett.* **108**, 173601 (2012).

[83] Röhlsberger, R., Schlage, K., Sahoo, B., Couet, S. & Rüffer, R. Collective lamb shift in single-photon superradiance. *Science* **328**, 1248–1251 (2010).

[84] Scully, M. O. & Svidzinsky, A. A. The lamb shift - yesterday, today, and tomorrow. *Science* **328**, 1239–1241 (2010).

[85] Anderson, W., Veale, J. & Gallagher, T. Resonant dipole-dipole energy transfer in a nearly frozen rydberg gas. *Physical review letters* **80**, 249–252 (1998).

[86] Afrousheh, K. *et al.* Spectroscopic observation of resonant electric dipole-dipole interactions between cold rydberg atoms. *Phys. Rev. Lett.* **93**, 233001 (2004).

[87] van Ditzhuijzen, C. S. E. *et al.* Spatially resolved observation of dipole-dipole interaction between rydberg atoms. *Phys. Rev. Lett.* **100**, 243201 (2008).

[88] Van Loo, A. F. *et al.* Photon-mediated interactions between distant artificial atoms. *Science* **342**, 1494–1496 (2013).

[89] Forster, T. Zwischenmolekulare energiewanderung und fluoreszenz). *Ann. Phys* **437**, 55 (1948).

[90] Hettich, C. *et al.* Nanometer resolution and coherent optical dipole coupling of two individual molecules. *Science* **298**, 385–389 (2002).

[91] Lukin, M. D. *et al.* Dipole blockade and quantum information processing in mesoscopic atomic ensembles. *Phys. Rev. Lett.* **87**, 037901 (2001).

[92] Urban, E. *et al.* Observation of rydberg blockade between two atoms. *Nature Physics* **5**, 110–114 (2009).

[93] Miroshnychenko, Y. *et al.* Observation of collective excitation of two individual atoms in the rydberg blockade regime. *Nature Physics* **5**, 115–118 (2009).

[94] DeVoe, R. & Brewer, R. Observation of superradiant and subradiant spontaneous emission of two trapped ions. *Physical review letters* **76**, 2049 (1996).

[95] Scully, M. O. Collective lamb shift in single photon dicke superradiance. *Physical review letters* **102**, 143601 (2009).

[96] Gross, M. & Haroche, S. Superradiance: An essay on the theory of collective spontaneous emission. *Physics Reports* **93**, 301–396 (1982).

[97] Scully, M. O., Fry, E. S., Ooi, C. R. & Wódkiewicz, K. Directed spontaneous emission from an extended ensemble of n atoms: Timing is everything. *Physical review letters* **96**, 010501 (2006).

[98] Richter, T. Cooperative spontaneous emission from an initially fully excited system of three identical two-level atoms. *Annalen der Physik* **495**, 234–261 (1983).

[99] Freedhoff, H. S. Spontaneous emission by a fully excited system of three identical atoms. *Journal of Physics B: Atomic and Molecular Physics* **19**, 3035 (1986).

[100] Grünwald, P. & Vogel, W. Entanglement in atomic resonance fluorescence. *Physical review letters* **104**, 233602 (2010).

[101] Clemens, J., Horvath, L., Sanders, B. & Carmichael, H. Collective spontaneous emission from a line of atoms. *Physical Review A* **68**, 023809 (2003).

[102] See Supplemental Material at http://link.aps.org/ supplemental/10.1103/PhysRevLett.113.193002 for more details regarding the system apparatus, measurements techniques and theoretical derivations.

[103] Kramida, A., Yu. Ralchenko, Reader, J. & and NIST ASD Team. NIST Atomic Spectra Database (ver. 5.1), [Online]. Available: `http://physics.nist.gov/asd` [2013, November 20]. National Institute of Standards and Technology, Gaithersburg, MD. (2013).

[104] James, D. Quantum dynamics of cold trapped ions with application to quantum computation. *Appl. Phys. B* **66**, 181–190 (1998).

[105] In the case of five [panel (c)] and seven ions [panel (e)], the data points at the tip of the peaks were excluded when calculating the mean.

[106] Eschner, J., Raab, C., Schmidt-Kaler, F. & Blatt, R. Light interference from single atoms and their mirror images. *Nature* **413**, 495–498 (2001).

[107] Wilson, M. *et al.* Vacuum-field level shifts in a single trapped ion mediated by a single distant mirror. *Physical review letters* **91**, 213602 (2003).

[108] Bushev, P. *et al.* Forces between a single atom and its distant mirror image. *Physical review letters* **92**, 223602 (2004).

[109] Hétet, G., Slodička, L., Hennrich, M. & Blatt, R. Single atom as a mirror of an optical cavity. *Phys. Rev. Lett.* **107**, 133002 (2011).

[110] Härter, A., Krükow, A., Brunner, A. & Denschlag, J. H. Long-term drifts of stray electric fields in a Paul trap. *Applied Physics B* **114**, 275–281 (2014).

[111] Turchette, Q. A. *et al.* Heating of trapped ions from the quantum ground state. *Phys. Rev. A* **61**, 063418 (2000).

[112] Sage, J. M., Kerman, A. J. & Chiaverini, J. Loading of a surface-electrode ion trap from a remote, precooled source. *Phys. Rev. A* **86**, 013417 (2012).

[113] Idziaszek, Z., Calarco, T., Julienne, P. S. & Simoni, A. Quantum theory of ultracold atom-ion collisions. *Phys. Rev. A* **79**, 010702 (2009).

[114] Härter, A. *et al.* Single ion as a three-body reaction center in an ultracold atomic gas. *Phys. Rev. Lett.* **109**, 123201 (2012).

[115] Schowalter, S. J. *et al.* Blue-sky bifurcation of ion energies and the limits of neutral-gas sympathetic cooling of trapped ions. *Nature Communications* **7** (2016).

[116] Rouse, I. & Willitsch, S. Superstatistical velocity distributions of cold trapped ions in molecular-dynamics simulations. *Phys. Rev. A* **92**, 053420 (2015).

[117] Goodman, D., Sivarajah, I., Wells, J., Narducci, F. & Smith, W. Ion–neutral-atom sympathetic cooling in a hybrid linear rf paul and magneto-optical trap. *Phys. Rev. A* **86**, 033408 (2012).

[118] Krych, M. & Idziaszek, Z. Description of ion motion in a Paul trap immersed in a cold atomic gas. *Phys. Rev. A* **91**, 023430 (2015).

[119] Wesenberg, J. H. *et al.* Fluorescence during Doppler cooling of a single trapped atom. *Phys. Rev. A* **76**, 053416 (2007).

[120] See Supplemental Material online for detailed description of the apparatus, likelihood estimation and simulations.

[121] Work in progress.

[122] In preperation.

[123] Wineland, D. J. & Itano, W. M. Laser cooling of atoms. *Physical Review A* **20**, 1521 (1979).

[124] Goodwin, J. F., Stutter, G., Thompson, R. C. & Segal, D. M. Resolved-sideband laser cooling in a penning trap. *Phys. Rev. Lett.* **116**, 143002 (2016).

Chapter 7

Appendix A - ion art

This chapter is dedicated to my wife which, during the years, cultivated in me a sense of appreciation for aesthetics. It needless to mention that none of the following images was treated with any graphic software such as Photoshop.

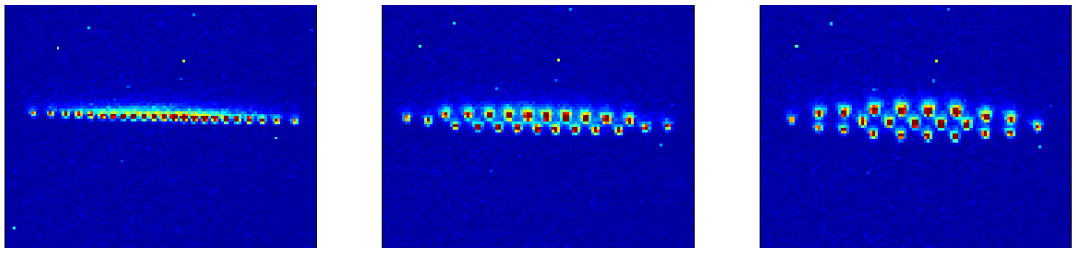

(a) Linear chain (b) Zig-Zag crystal (c) Zig-Zag-Zog

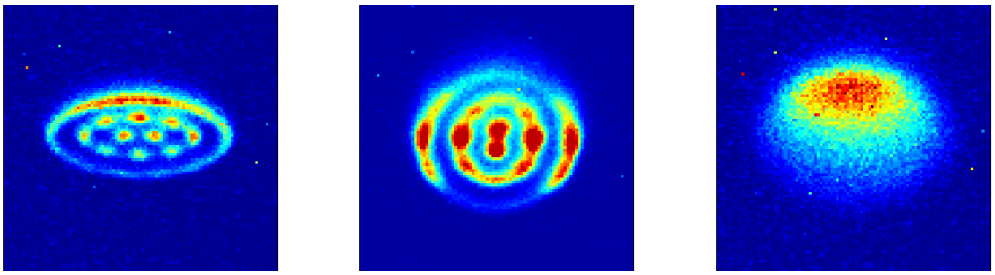

(d) Stadium (e) Darts (f) Ball

Figure 7.1: 23 ions crystal. By decreasing the ratio between radial and axial trap frequencies, the crystal transforms from a linear (a) chain to a 2D crystal (b-c). At some point the crystal partially melts and some of the ions follow well defined trajectories (d-e). Further decrease of the radial frequency results in a complete melting of the crystal (f).

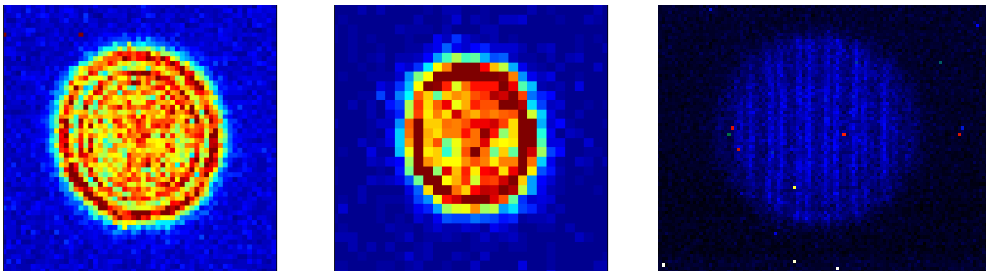

(a) Big pizza (b) Small pizza (c) Uranus

Figure 7.2: Defocused ion images. In (a) and (b) we image a single ion where the imaging system is defocused from the imaging plane. In (c) we image three ions which results in interference fringes patteren.

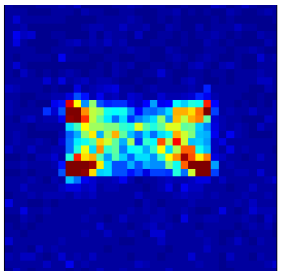

(a) Butterfly

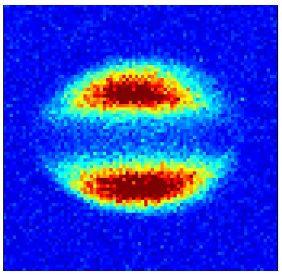

(b) Ion burger

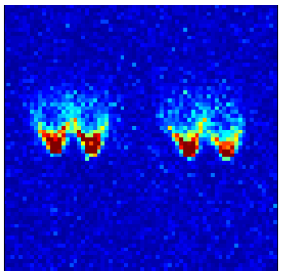

(c) Cat state

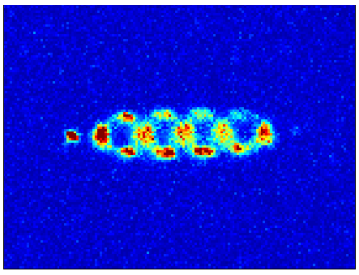

(d) Challah

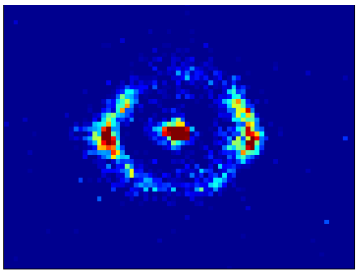

(e) Eye of Sauron

Figure 7.3: a) Single ion in a very bad mood. b) Mixed cloud of $^{88}Sr^{+}$ and $^{87}Rb^{+}$ ions. The Rb ions, which are dark, are drawn to center of the cloud due to their smaller mass. c) Four bright ions and two dark ions in a linear chain. The funny shape of the ions is due to imaging system abberations. d) Few ions following a spiralling trajectory. e) Two ions are orbiting around a single ion in the center of the trap[a].

[a] One Ion to rule them all, One Ion to find them, One Ion to bring them all and in the darkness bind them.

Chapter 8
Declaration

I declare that this thesis, *"Dynamics of a single, ground-state cooled and trapped ion colliding with ultracold atoms: A micromotion tale"*, is a record of the bona fide research work done by me under the supervision of Dr. Roee Ozeri in the Department of Complex Physics, The Weizmann Institute of Science, Israel. Section 3.5 of this thesis is a report of my mutual work with Dr. Osip Schwartz. While Osip was motivated by the theoretical aspects of this work I was more kin on the experimental aspects of precision spectroscopy with ions. Nonetheless, we shared the same responsibility for taking lab data, theory, manuscript writing and ideas.

Ziv Meir